Synthesis of Slender Spatial Compliant Mechanisms with application to passive exoskeletons

Amoozandeh, A.

DOI
10.4233/uuid:4be5a4e1-7c68-4a28-a1ba-4cff02a9f024

Publication date
2023

Document Version
Final published version

Citation (APA)
Amoozandeh, A. (2023). *Synthesis of Slender Spatial Compliant Mechanisms with application to passive exoskeletons*. [Dissertation (TU Delft), Delft University of Technology]. https://doi.org/10.4233/uuid:4be5a4e1-7c68-4a28-a1ba-4cff02a9f024

Synthesis of Slender Spatial Compliant Mechanisms

with application to passive exoskeletons

Synthesis of Slender Spatial Compliant Mechanisms

with application to passive exoskeletons

Dissertation

for the purpose of obtaining the degree of doctor
at Delft University of Technology,
by the authority of the Rector Magnificus Prof.dr.ir. T.H.J.J. van der Hagen,
chair of the Board for Doctorates,
to be defended publicly on,
Thursday 21 September 2023 at 15:00 o'clock.

by

Ali AMOOZANDEH NOBAVEH

Master of Science in Mechanical Engineering - Applied Design,
Sharif University of Technology, Iran,
born in Tehran, Iran.

This dissertation has been approved by the promotors.

Composition of the doctoral committee:

Rector Magnificus,	Chairperson
Prof. dr. ir. J.L. Herder,	Delft University of Technology, promotor
Dr. ir. R.A.J. van Ostayen,	Delft University of Technology, promotor
Independent members:	
Prof. dr. ir. L.J. Sluys,	Delft University of Technology
Prof. dr. ing. H. Vallery,	Delft University of Technology
Prof. dr. ir. H. van der Kooij,	University of Twente
Dr. ir. M. Schenk,	University of Bristol
Other members:	
Dr. ir. G. Radaelli,	Delft University of Technology

Keywords: Spatial Compliant Mechanisms, Spatially Curved Beams,
Anisotropic Variable Stiffness, Compliant Transmission,
Zero Torsional Stiffness, Passive Exoskeletons

Printed by: ProefschriftMaken

ISBN 978-94-6366-741-8

Strive for perfection in everything you do. Take the best that exists and make it better.
When it does not exist, DESIGN IT.

Henry Royce

Contents

Summary

Industrial passive exoskeletons have been developed for years as a tool to reduce the physical workload of their users. They accomplish this by compensating for the user's body weight and decreasing fatigue caused by repetitive loads. Despite their advantages, current exoskeletons have drawbacks that make them less convenient for users and thus less common as a supporting tool. Among the other issues, the most important are impeded and reduced movement, posture strain, and increased discomfort. This thesis proposes designs for spatial compliant mechanisms to address these issues in exoskeletons.

Compliant mechanisms gain their motion from the elastic deformation of their elements. Therefore, they can also store energy in their range of motion. This means that using them reduces the weight and cost of exoskeletons by combining energy storage and kinematic functions into a single element. Furthermore, these mechanisms can improve flexibility and resolve exoskeleton issues caused by kinematic constraints.

The objective of this thesis is to propose designs, develop understanding and demonstrate the applications of slender spatial compliant mechanisms in exoskeletons. The thesis is divided into three parts, wherein Part I, Chapter 2 and 3, investigates the effect of shape and boundary conditions to achieve specific kinetostatic behavior at the endpoint of spatially curved beams. Part II, Chapter 4 and 5, discusses the methods to achieve transmission, coupling, and zero stiffness in slender twisting beams. Part III, Chapter 6 and 7, presents two applications of the knowledge that was developed in Part I and II, in passive exoskeletons.

An optimization scheme for the shape and cross-sections of spatially curved beams is presented in Chapter 2 with the aim of achieving certain kinetostatic behavior. As a case study, the symmetry of the endpoint behavior of asymmetric cantilever beams is shown to be improved by 68%, based on the experiments. The torsional deformations along the beam are considered to have a major effect on the endpoint kinetostatic behavior. Based on this conclusion, in Chapter 3, a bellow is used as a torsional stiffener for spatially curved beams that have relatively low torsion and high bending stiffness. The combination of the beam and sliding bellow led to anisotropically adaptive stiffness at the endpoint of the beam, with 21.5 times higher stiffness changes in one direction compared to its perpendicular.

With the focus on the importance of torsional deformation on the kinetostatic behavior of spatial mechanisms and the modes of deformation that can transfer the torsion along the structure, in Chapter 4, a transmission mechanism for twist along the beam utilizing warping is presented. The effect of the warping constant on the proposed continuously variable transmission is discussed, and transmission ratios between 4:1 and 1:4 are tested to verify the concept. In an effort to make this transmission zero stiffness and neutrally stable, in Chapter 5, a method to control the torsional stiffness of beams using preload is presented. Two concepts are introduced: a variable, including zero, torsional stiffness twisting beam, and a beam with switchable torsional stiffness between positive and zero.

Finally, to show the applications of the developed designs in exoskeletons, in Chapter 6 the tools of Chapter 2 is utilized to present a slender beam that can balance the weight of the hand in a range of 83 degrees of the wrist's flexion and extension. Chapter 7 introduces neutrally stable differential mechanisms based on the knowledge developed in Chapter 5. The differential is employed in passive back support exoskeletons to address a fundamental problem by averaging leg angles to eliminate undesired forces during walking with the passive exoskeleton.

Samenvatting

Industriële passieve exoskeletten worden al jaren ontwikkeld als hulpmiddel om de fysieke belasting van hun gebruikers te verminderen. Zij doen dit door het lichaamsgewicht van de gebruiker te compenseren en daardoor vermoeidheid door repetitieve belasting te verminderen. De huidige exoskeletten hebben ook nadelen die ze minder geschikt maken voor gebruikers. De belangrijkste zijn belemmerde en verminderde beweging van de gebruiker, overbelasting door verkeerde houdingen en verhoogd ongemak. Dit proefschrift introduceert ontwerpen voor ruimtelijke compliante mechanismen om deze problemen in exoskeletten te verhelpen.

Compliante mechanismen ontlenen hun beweging aan de elastische vervorming van hun elementen, waarmee ze tegelijkertijd energie kunnen opslaan. Omdat energieopslag en kinematische functies in één enkel element worden gecombineerd, kunnen compliante mechanismen het gewicht en de kosten van exoskeletten verminderen. Daarnaast kunnen ze door hun flexibiliteit problemen als gevolg van de kinematische beperkingen van exoskeletten oplossen.

Het doel van dit proefschrift is het tonen van ontwerpen, het ontwikkelen van begrip en het demonstreren van toepassingen van slanke ruimtelijke compliante mechanismen in exoskeletten. Het proefschrift is opgedeeld in drie delen, waarbij in deel I, hoofdstuk 2 en 3, het effect van vorm en randvoorwaarden wordt onderzocht om specifiek kinetostatisch gedrag te realiseren aan het eindpunt van ruimtelijk gekromde balken. Deel II, hoofdstuk 4 en 5, bespreekt de methoden om transmissie, koppeling en nul stijfheid te realiseren in dunne torderende balken. Deel III, hoofdstuk 6 en 7, presenteert twee toepassingen van de kennis die ontwikkeld is in deel I en II, in passieve exoskeletten.

Hoofdstuk 2 presenteert een optimalisatieschema voor de vorm en doorsnede van ruimtelijk gekromde balken met als doel een bepaald kinetostatisch gedrag te realiseren. Experimenten tonen aan dat de symmetrie van het eindpuntsgedrag van asymmetrische enkelzijdig ingeklemde balken wordt verbeterd met 68%. De torsievervormingen langs de balk worden geacht een groot effect te hebben op het kinetostatisch gedrag van het eindpunt. Daarom wordt in hoofdstuk 3 een balg gebruikt als torsieverstijver voor ruimtelijk gekromde balken met een relatief lage torsiestijfheid en een hoge buigstijfheid. Deze combinatie leidt tot een anisotroop aanpasbare stijfheid aan het eindpunt van de balken, met 21,5 maal hogere stijfheidsveranderingen in één richting vergeleken met de richting loodrecht daarop.

Met de nadruk op het belang van torsievervorming op het kinetostatisch gedrag van ruimtelijke mechanismen en de vervormingsmodi die de torsie langs de constructie kunnen overbrengen, wordt in hoofdstuk 4 een transmissiemechanisme voor torsie langs de balk met behulp van welving gepresenteerd. Het effect van de welvingconstante op de voorgestelde continu variabele overbrenging wordt besproken, en overbrengingsverhoudingen tussen 4:1 en 1:4 worden getest om het concept te verifiëren. Met als doel deze overbrenging stijfheidsvrij en neutraal stabiel te maken, wordt in hoofdstuk 5 een methode gepresenteerd om de torsiestijfheid van balken te regelen met behulp van voorspanning. Dit heeft geresulteerd in twee concepten: een torderende balk met variabele stijfheid, inclusief nul stijfheid, en een balk met schakelbare torsiestijfheid tussen positief en nul.

De technieken van hoofdstuk 2 worden in hoofdstuk 6 gebruikt om de toepassing van de ontwerpen in exoskeletten te tonen. Een slanke balk wordt gepresenteerd die het gewicht van de hand in een polsondersteunend exoskelet kan balanceren, in een bereik van

83 graden flexie en extensie van de pols. Hoofdstuk 7 introduceert neutraal stabiele differentiële mechanismen gebaseerd op de kennis ontwikkeld in hoofdstuk 5. Het differentieel wordt gebruikt in exoskeletten met passieve rugondersteuning om een fundamenteel probleem aan te pakken door beenhoeken te middelen om ongewenste krachten tijdens het lopen met het passieve exoskelet te elimineren.

1

Introduction

This chapter presents an introduction to the research and its primary aim, which is to develop designs for slender spatial compliant mechanisms (CMs) intended for passive exoskeletons. It includes a background and an overview of the current status of these wearable devices and discusses the potential benefits of using CMs in this application. Moreover, the scientific gaps in the state-of-the-art CMs, as well as the objectives of the present work, are elucidated in this chapter. Finally, the thesis structure is outlined, showing how the different parts and chapters interrelate.

1.1 Background

Before the industrial revolution most of the work performed by humans came in the form of physical labor, often supported by animals. With the advent of machines, much of this physical labor was replaced by them. However, to this day, there are still many tasks that can only, or most efficiently, be performed by humans through physical labor. To support humans in these tasks, exoskeletons as a tool with the ultimate goal of supporting human movement are being developed. These wearable devices are beneficial not only for healthy users by reducing labor but also for those with disabilities or injuries by assisting them in moving and performing daily life tasks.

After the invention of the modern wearable devices that follow human motion while supporting the body, the term exoskeleton was applied to them. This word comes from Greek and is a combination of two words, *éxō* “outer” and *skeletós* “skeleton”. This term was originally used to indicate the outer shell that supports an animal’s body [1].

Exoskeletons can be categorized in several ways, based on their applications, e.g., medical, for people with spinal cord injuries [2] or with duchenne muscular dystrophy [3]; or industrial, for workers to reduce the physical workload. These devices can also be classified based on their working principle, e.g., passive, wherein no energy is added to the device other than the energy provided by the user’s movement, and active wherein a source of energy, e.g., battery, runs actuators to support the motion.

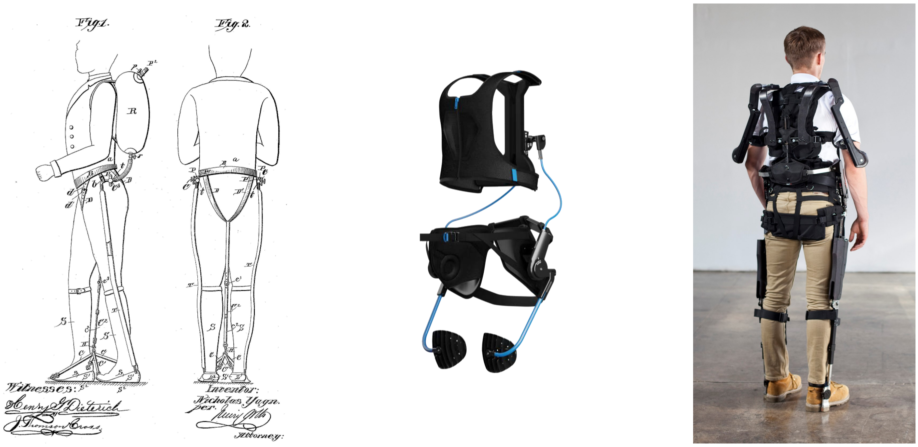

(a) (b) (c)

Figure 1.1: (a) The first known passive exoskeleton [4]. Examples of current commercial passive exoskeletons, (b) Flex from Laevo, (c) Suitx from US Bionics.

Passive exoskeletons are generally lighter and less expensive than their active counterparts, since they do not include batteries and actuators. In addition, they are economically more feasible and accessible to those who require a simpler support device. The earliest known passive exoskeleton was developed in 1890 by Nicholas Yagin [4]. This device was used as a movement-assist, as shown in Fig.1.1(a).

A passive exoskeleton in industrial contexts can increase endurance, reduce the muscular activity and the risk of musculoskeletal disorders [5]. This means healthier and more productive workers [6]. More recent examples of passive industrial exoskeletons are presented in Fig. 1.1(b, c). Research shows that these passive devices can reduce muscle activity by up to forty percent in dynamic lifting and reduce spinal loading by nearly thirty percent, besides reducing overall muscular fatigue [7].

1.2 Problem statement and possible solution

Despite years of development, current exoskeletons have some unanticipated ergonomical effects, e.g., kinematic constraints [8], which causes impeded and reduced range of motion [9, 10], posture strain [9], increased discomfort due to localized contact pressure [5], long-term fatigue due to the device's weight, and size adaptability issues. Most of these problems are due to the fact that current exoskeletons are mainly made from rigid elements which are connected to each-other in discrete locations to replicate the kinematic of the human body, beside having separate energy sources like actuators or springs to support the movements.

Several studies have been done to resolve these issues, and fields of research such as soft exosuits [11, 12], i.e., exoskeletons made from textiles and elastic segments instead of rigid bodies, are developed to directly answer the lack of flexibility and kinematic freedom in exoskeletons. However, even this type of exoskeleton is still having issues providing enough support as compared with conventional rigid element exoskeletons. In this regard, a possible solution between rigid and soft exoskeletons that can provide flexibility without impeding their functionality is the use of compliant mechanisms.

1.3 Compliant mechanisms

Compliant mechanisms (CMs) are a type of mechanisms that gain their motion from the deformation of their elements [13]. These mechanisms allow engineers to improve their design efficiency by (1) reducing the part count and decreasing the cost, (2) integrating functionality, (3) reducing the occupied space and weight, and (4) enhancing reliability and precision since they are not suffering from backlash or surface wear that affect conventional multi-bodied mechanisms [14].

Using these mechanisms in exoskeletons has the advantage of being flexible to match human movements and providing kinematic freedom, besides having a structure where the reaction forces can be applied to provide enough support for the user. CMs can combine the kinematics that were achieved in conventional exoskeletons by rigid systems and the energy storage that was achieved by springs or elastic bands, into one element. Therefore, utilizing them in exoskeletons reduces the weight of the device and improve the user's long-term convenience. It is important to note that having the mentioned features is not only making CMs beneficial in exoskeleton design, but also renders them advantageous for use in a variety of other wearable devices, such as orthoses and prostheses.

1.4 Scientific gap

The CMs utilized in the exoskeleton context should be able to support not only spatial motion but also spatial load cases since they are designed to interact with and support the human body. However, in the literature, CMs are mainly developed in a planar format.

There are only a small number of designs for spatial CMs in the literature [15, 16], and even the most complex spatial designs tend to be composed of planar modules [17, 18]. One example of this type of CMs is shown in Fig. 1.2. A prevailing issue of these CMs is the presence of rigid elements that connect separate compliant components. These elements are increasing the overall bulkiness and adding extra weight and space to the design and may lead to undesired dynamics.

Given the complexity of mechanical components in wearable devices, but also in other fields such as aerospace engineering and surgical robotics, where weight and design space are highly constrained, there exists a pressing need to effectively use the potential elasticity of all materials utilized in the CM design to achieve the necessary motion and support, while minimizing excess bulk and weight.

Recent research endeavors in the field of spatial CMs that effectively use all the compliancy of material have been influenced by the growth of computational power and the desire for enhanced functionality [19, 20]. Additionally, advancements in materials science and manufacturing techniques [21] have facilitated the development of more intricate CM shapes. However, among the present spatial designs, the topologies that can be made with simpler and more feasible techniques and yet employs all the capacity of the used material are barely investigated.

Figure 1.2: An example of a tip-tilt compliant mechanism, designed for space applications. This monolithic mechanism is made from several planar compliant modules, cross-axis flexural pivots, connected to each other with rigid elements [17].

1.5 Research objective

To address the need for slender spatial elements in the realm of CMs, with an eye towards their practical applications, we will propose novel designs that expand the toolbox available to compliant mechanism designers, thereby enabling more versatile design possibilities for spatial applications such as wearable devices. The presented designs will be lightweight, yet manufacturable and feasible for passive exoskeletons.

1.6 Approach

The approach of this thesis is to translate the functional requirements for different parts of exoskeletons to the kinetostatic behavior of compliant elements. Having the required behavior and with an eye on effects that only occur in spatial structures such as torsional deformation or warping, several concepts are proposed in the first and second part of the thesis which focus on the development of the concepts.

Once the final concepts and the required knowledge have been determined, in the third part of the thesis, the necessary understanding of the designs and how to simulate, test, and then use them in the main application of this project is developed and discussed.

1.7 Outline

Figure 1.3 schemes the outline of this thesis. In Part I, the effect of the shape and boundary conditions of the slender spatially curved beams on their endpoint kinetostatic behavior is investigated. Chapters 2 and 3 from this part show two designs of these curved beams.

In Part II, the effect of warping on the distribution of torsion along straight twisting beams, together with a technique to tune the torsional stiffness of these elements are investigated. Chapters 4 and 5 from this part present two concepts of these open thin-walled beams.

Finally, in Part III of the thesis, two applications of the proposed designs in Parts I and II on exoskeletons are presented. Chapter 6 is based on the design tool developed in Part I, and Chapter 7 is based on the methods developed in Part II.

Chapter 2 proposes a design approach based on numerical optimization that can achieve different kinetostatic behavior at the endpoint of a beam. The effect of sectional and shape parameters along the beam on improving a specific behavior that is selected as symmetric behavior from asymmetric beams is evaluated.

Chapter 3 introduces a technique to achieve anisotropic adaptive stiffness using contrasting elements. A bellow with high torsion and low bending stiffness is used as a tunable stiffener for a beam with low torsion and high bending stiffness to achieve the required behavior.

Chapter 4 presents a design for compliant transmission using warping as the working principle, where the change in transmission ratio is available by changing the location of the constraints along the twisting beams.

Chapter 5 proposes a method to control the torsional stiffness of these twisting beams by prestressing, and it elaborates on the effect of sectional warping rigidity on the behavior achieved from different twisting beams.

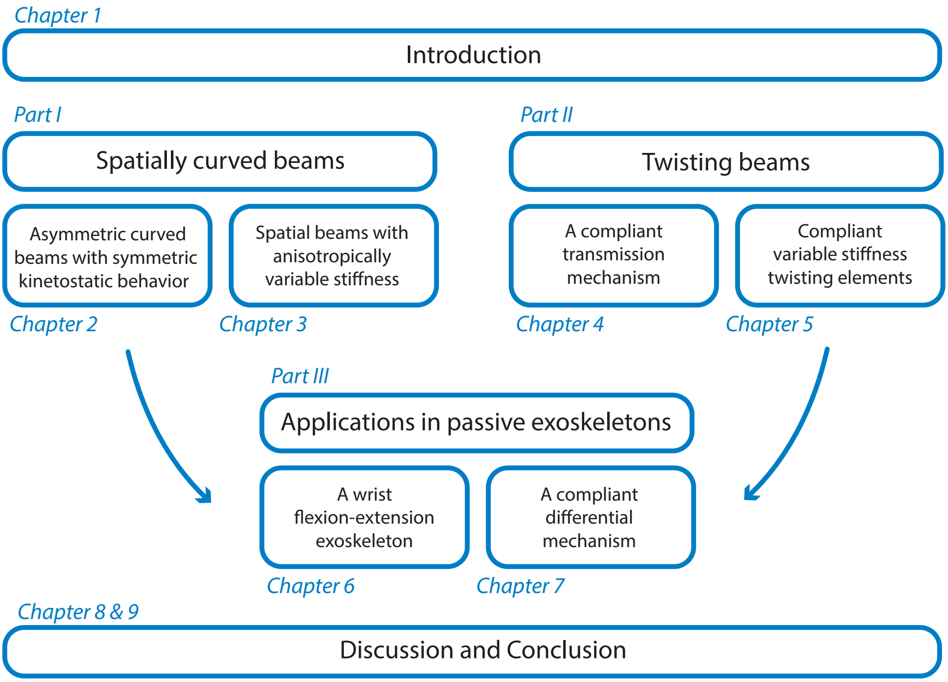

Figure 1.3: The outline of this thesis demonstrates how the knowledge gained in Parts I and II is applied in real-world applications in Part III. Chapter 6 is based on the design tool developed in Part I, and Chapter 7 is based on the methods developed in Part II.

Chapter 6 introduces a wrist support using the technique proposed in Part I to design a beam that can balance the weight of the user's hand in a large range of motion. This balancing result in a decrease of the energy required to move the hand in its range of motion.

Chapter 7 presents a curved differential mechanism, which is designed based on the principles discussed in Part II. This mechanism couples the reverse motion of legs with regard to the upper body when an exoskeleton user is walking and locks the motion between the upper and lower bodies when the user is bending, and by doing that, it resolves one of the main issues in passive back support exoskeletons.

Chapters 8 and 9 discuss and summarize the most important findings in this work as well as recommendations for possible future improvements of the proposed designs and considerations for this research direction to bring the final aim of the work one step closer to reality.

References

[1] H. Douglas, “Exoskeletons,” *Online etymology dictionary*, 2001. [Online; accessed 2023-03-20].

[2] C. Meijneke, G. Van Oort, V. Sluiter, E. Van Asseldonk, N. Tagliamonte, F. Tamburella, I. Pisotta, M. Masciullo, M. Arquilla, M. Molinari, *et al.*, “Symbitron exoskeleton: Design, control, and evaluation of a modular exoskeleton for incomplete and complete spinal cord injured individuals,” *IEEE transactions on neural systems and rehabilitation engineering*, vol. 29, pp. 330–339, 2021.

[3] P. N. Kooren, A. G. Dunning, M. M. Janssen, J. Lobo-Prat, B. F. Koopman, M. I. Paalman, I. J. de Groot, and J. L. Herder, “Design and pilot validation of a-gear: a novel wearable dynamic arm support,” *Journal of neuroengineering and rehabilitation*, vol. 12, no. 1, pp. 1–12, 2015.

[4] N. Yagin, “Apparatus for facilitating walking,” *US Patent 440684A*, filed February 11, 1890, issued November 18, 1890.

[5] T. Bosch, J. van Eck, K. Knitel, and M. de Looze, “The effects of a passive exoskeleton on muscle activity, discomfort and endurance time in forward bending work,” *Applied ergonomics*, vol. 54, pp. 212–217, 2016.

[6] B. McGowan, “Industrial exoskeletons: what you’re not hearing,” *Occupational Health and Safety Magazine*, vol. 1, 2018.

[7] M. P. De Looze, T. Bosch, F. Krause, K. S. Stadler, and L. W. O’sullivan, “Exoskeletons for industrial application and their potential effects on physical work load,” *Ergonomics*, vol. 59, no. 5, pp. 671–681, 2016.

[8] J. Theurel, K. Desbrosses, T. Roux, and A. Savescu, “Physiological consequences of using an upper limb exoskeleton during manual handling tasks,” *Applied ergonomics*, vol. 67, pp. 211–217, 2018.

[9] S. Kim, M. A. Nussbaum, M. I. M. Esfahani, M. M. Alemi, B. Jia, and E. Rashedi, “Assessing the influence of a passive, upper extremity exoskeletal vest for tasks requiring arm elevation: Part ii–“unexpected” effects on shoulder motion, balance, and spine loading,” *Applied ergonomics*, vol. 70, pp. 323–330, 2018.

[10] E. Rashedi, S. Kim, M. A. Nussbaum, and M. J. Agnew, “Ergonomic evaluation of a wearable assistive device for overhead work,” *Ergonomics*, vol. 57, no. 12, pp. 1864–1874, 2014.

[11] A. T. Asbeck, K. Schmidt, and C. J. Walsh, “Soft exosuit for hip assistance,” *Robotics and Autonomous Systems*, vol. 73, pp. 102–110, 2015.

[12] M. Wehner, B. Quinlivan, P. M. Aubin, E. Martinez-Villalpando, M. Baumann, L. Stirling, K. Holt, R. Wood, and C. Walsh, “A lightweight soft exosuit for gait assistance,” in *2013 IEEE international conference on robotics and automation*, pp. 3362–3369, IEEE, 2013.

[13] A. Midha, T. W. Norton, and L. L. Howell, "On the nomenclature, classification, and abstractions of compliant mechanisms," 1994.

[14] L. L. Howell, *Compliant Mechanisms.* John Wiley & Sons, 2001.

[15] M. Ling, D. Song, X. Zhang, X. He, H. Li, M. Wu, L. Cao, and S. Lu, "Analysis and design of spatial compliant mechanisms using a 3-d dynamic stiffness model," *Mechanism and Machine Theory*, vol. 168, p. 104581, 2022.

[16] F. P. Rad, R. Vertechy, G. Berselli, and V. Parenti-Castelli, "Analytical compliance analysis and finite element verification of spherical flexure hinges for spatial compliant mechanisms," *Mechanism and Machine Theory*, vol. 101, pp. 168–180, 2016.

[17] E. G. Merriam, *Fully Compliant Mechanisms for Bearing Subtraction in Robotics and Space Applications.* Brigham Young University, 2013.

[18] D. F. Machekposhti, N. Tolou, and J. Herder, "A fully compliant homokinetic coupling," *Journal of Mechanical Design*, vol. 140, no. 1, p. 012301, 2018.

[19] B. Zhu, X. Zhang, H. Zhang, J. Liang, H. Zang, H. Li, and R. Wang, "Design of compliant mechanisms using continuum topology optimization: A review," *Mechanism and Machine Theory*, vol. 143, p. 103622, 2020.

[20] X. Zhang and B. Zhu, *Topology optimization of compliant mechanisms.* Springer, 2018.

[21] Y. Luo, O. Sigmund, Q. Li, and S. Liu, "Additive manufacturing oriented topology optimization of structures with self-supported enclosed voids," *Computer Methods in Applied Mechanics and Engineering*, vol. 372, p. 113385, 2020.

I

Spatially curved beams

2

Asymmetric curved beams with symmetric behavior

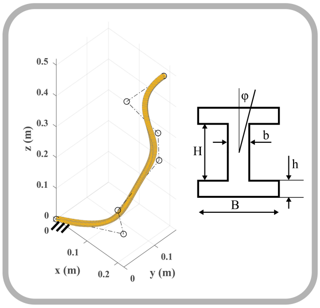

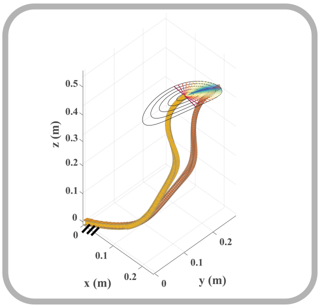

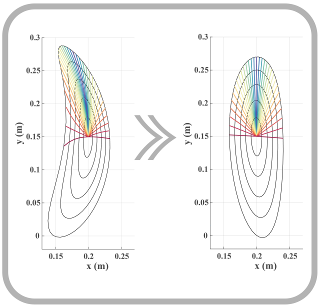

In Part I of the thesis, the kinetostatic behavior of the endpoints of spatially curved beams will be investigated, and the effect of shape and boundary conditions on their behavior will be discussed. This chapter is an effort to understand the effect of the shape of the beam on the endpoint's kinetostatic behavior. A numerical optimization scheme that enhances the desired behavior of clamped-free beams using shape parameters is introduced. The optimizer uses the coordinates of a certain number of control points to make a B-spline for the curved shape as well as the parameters of an I-section as inputs. The optimizer's goal function is set based on the endpoint's motion and reaction forces over a wide range of deformations. In this work, the objective is to achieve symmetric behavior from asymmetric curved beams. A constrained design space was also applied to the shape to show the ability of the developed scheme to come up with solutions in a limited design space.

This chapter was published as:
Amoozandeh Nobaveh, A., Radaelli, G., and Herder, J., 2022. Symmetric Kinetostatic Behavior from Asymmetric Spatially Curved Beams. *Journal of Mechanisms and Robotics*, 15(4), p.041010.

Symmetric Kinetostatic Behavior from Asymmetric Spatially Curved Beams

Abstract *A cantilevered rod's endpoint has a symmetric stiffness profile throughout its range of motion. Generally, this is not the case for spatially curved compliant beams, particularly if they are asymmetric, i.e., their fixation is not in the symmetry plane of their endpoint operating field. This chapter discusses a technique for obtaining symmetric kinetostatic behavior from this type of asymmetric compliant beam over a relatively large range of motion. To accomplish this, a parametrization scheme was used to base the geometry of the beam on a limited number of control parameters. These parameters were then used as inputs for optimization in order to create beams with symmetric endpoint behavior. This process was further investigated using different sets of parameters. To validate the method's performance, experiments on prototypes were conducted. The results demonstrated a high degree of congruence with simulations of the anticipated behavior. Comparing to the non-optimized benchmark beam, the experimental performance of the resulting shapes demonstrated up to a 68% improvement in the desired symmetric behavior.*

2.1 Introduction

Numerous studies have been conducted on the design of complex monolithic spatial elements with the ultimate goal of increasing a structure's rigidity by reducing elastic deformations [1]. On the other hand, there are various applications where large-deformable elements with specific force-deflection behavior are desirable. Thus, introducing compliancy along the part becomes essential. These monolithic compliant elements are classified as a type of Compliant Mechanism (CM) as they can provide a specific motion while they are elastically deforming [2–4].

Several engineering applications could benefit from monolithic CMs with a spatial range of motion as a more efficient replacement of complex conventional (rigid body chain) mechanisms, applications where slenderness and being lightweight are essential, e.g. gravity balancers for wearable devices like exoskeletons and prostheses, where a certain compensating force within a spatial motion is expected in a very limited design space around the user's body [5–8].

In recent years, spatial CMs have become a topic of interest in the CM design community as planar CMs have been extensively investigated. Yet more complex design requirements were defined, which could only be addressed by three-dimensional motions. Efforts have been made in both the characterization as well as in the design and optimization of spatial CMs. For instance, in flexure mechanisms, there are plenty of examples and principles [9]. However, most of the developed spatial mechanisms are for precision devices, where they usually consist of several parts that make them bulky compared to their output range of motion.

Designing monolithic spatial CMs with an extensive range of motion were emerging in recent years [10–13]. The main advantage of having a fully compliant monolithic part to obtain a desired kinetostatic behavior is that the whole shape effectively takes part in the CM's characterization.

There are several widely used CM design methods, e.g. FACT, Building Block Approach, PRBM, etc [14–16]. However, using these methods for designing large deformable spatial monolithic parts is not feasible, because capturing the distributed contribution to the endpoint stiffness, in addition to a desired kinetostatic behavior from a spatially curved shape is more complex than what these methods can propose. Another approach is to take advantage of automated design methods like optimization. Concerning the complexity of the defined requirements, the latter approach was assumed to be a better choice to find these compliant shapes.

In this regard, there are a handful of studies on the topology optimization of monolithic CMs [17–20]. The output of these works were usually rather complex monolithic shapes which make them only fabricable with additive manufacturing techniques.

To achieve complex kinetostatic behavior and yet keep the CM manufacturable with common techniques, choosing a simple topology and optimizing its shape parameters can be considered a better solution [21]. There is extensive research in this regard, mainly in planar mechanisms [22, 23]. However, making use of spatial mechanisms can enable other possibilities, e.g., torsion of elements.

In this regard, spatial geometries varying from rods to shells were scarcely investigated [24–28]. There is no doubt that reaching exceptional kinetostatic behavior might be possible with different forms of compliant elements. However, from a utilization perspective as well as a fabrication perspective, it appears convenient to consider the simplest topology of a cantilevered spatial beam as the monolithic compliant element.

A useful yet undiscovered kinetostatic behavior from this type of CMs is sought in this work, where the end point of a spatially curved beam has symmetric stiffness behavior in its plane of motion, even if the beam is asymmetric in the sense that it is not grounded in the symmetry plane of its stiffness field. This situation emerges in several applications of manipulator-type devices where the endpoint symmetry plane is occupied and no room is available for the grounding point on that plane, these devices can be widely seen in surgical robots and aerospace structures. Also, in wearable devices where the desired symmetry plane of the limbs' motion is occupied by the body itself, or when a symmetrical support force is required but a symmetrical structure is not possible. For instance, consider a unilateral upper-body bending support for wheelchair users, it is not safe to lock the user's upper-body in a wheelchair with a bilateral, symmetrical structure, and a normal unilateral, asymmetrical structure cannot provide the symmetrical support on the chest and will turn open upon forward bending. In this instance, an asymmetric beam with symmetric kinetostatic behavior, such as the one proposed in this chapter, can supply the required bending support force while not restricting the user's freedom. The majority of the parameters used in this study are derived from the latter application. In our previous work [29], we showed that there exist non-uniform distributions of cross-sectional properties along an asymmetric beam for which the natural rotating behavior was corrected toward more symmetric endpoint behavior.

This chapter aimed to realize the effect of tuning the shape and sectional properties of a spatially curved asymmetric beam to enhance the symmetry of the endpoint's stiffness in a specific range of motion. By utilizing B-spline, a parametrization scheme was developed to generate beam shapes in the prescribed design space from a small set of parameters. An objective function was defined to evaluate the symmetric kinetostatic behavior of the endpoint in the range of motion. Additionally, an optimizer was used to improve the objective function iteratively by tuning shape parameters. Finally, experiments were conducted to validate the kinetostatic performance of the shapes generated by this process.

The chapter is structured as follows. In section 2.2, the definition of the requirements is specified together with the description of the optimization process for different combinations of parameters. Also, the formulation of the objective function and the optimization settings and the Finite Element solver are described. Furthermore, the verification procedure using experiments is discussed. In section 2.3, the resulting beams from all cases and their performance are shown and compared with the benchmark beam. A discussion on the validity of the results and possible improvements is given in section 2.4, and the conclusion is given in section 2.5.

2.2 Methods

The process of making and evaluating beams has different aspects. These aspects are discussed in the following subsections. The overall procedure can be summarized as follows: (1) A scheme for parametrizing the shape of beams using B-splines was developed to form the beams' shape using a limited number of control parameters. (2) The beams were generated by optimization of different sets of shape parameters. (3) The objective function of the optimization was defined to assess the symmetric kinetostatic behavior in the desired region. (4) The displacements of the beams under the objective function's loadings were numerically computed using a self-developed finite element model. (5) An experimental setup was designed to verify the beams' performance.

2.2.1 Beam geometry

As discussed in section 2.1 the topology of the simplest form of a monolithic CM is that of a cantilever beam. This includes a fixed clamp in the base and an asymmetric spatially curved beam which ends at an end-effector point at the tip.

The position of the grounding point was assumed to be at the origin of the Cartesian coordinate system, and the beam endpoint was chosen arbitrarily to be at $X_e = 0.20\,\text{m}$, $Y_e = 0.15\,\text{m}$, and $Z_e = 0.50\,\text{m}$ as shown in Fig. 2.1. The symmetry plane was selected as the plane that coincides with the endpoint, parallel to the YZ plane. The beam shape was formed based on the set of parameters described in further subsections.

2.2.2 Objective function

The defined objective function f_{total} for the optimization procedure, includes two parts f_1 and f_2. The first part, f_1, was defined to maximize the endpoint symmetric kinetostatic behavior. It is the average difference of the components of displacements in the X and Y

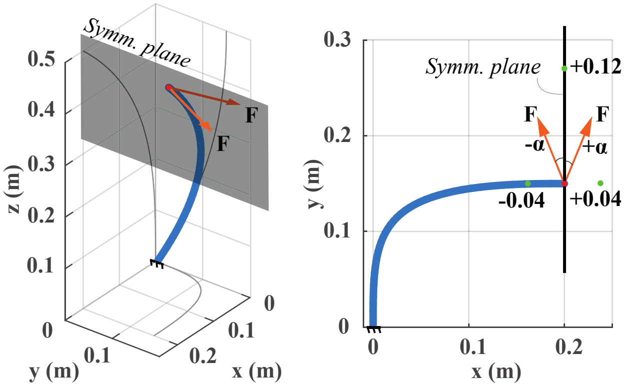

Figure 2.1: Isometric and top views of the asymmetric beam with its fixed grounding and loaded endpoint, where a pair of mirrored loadings about the desired symmetry plane are shown as demonstration. In the top view, desired displacements upon sides and front loadings with $F = 100\,\text{N}$ are shown with green points.

directions as a result of three mirrored tip loadings with a force magnitude of $F = 100\,\text{N}$ and mirrored angles of $\pm\alpha$, where $\alpha = 30°, 60°, 90°$, plus a straight loading for finding the drift from the symmetry plane in X direction when $\alpha = 0°$. The reasoning behind selecting only three mirrored loadings for the objective function of this application is explained in the previous work [29]. f_1 which is the summation of these differences was named *Symmetry Error*, as reducing it will cause more symmetrical behavior for the endpoint of the beam. Hence, it improves the symmetry response within the desired deformation region. However, this region might be unsatisfactory in terms of in-plane and out-of-plane displacement magnitudes, i.e., the resulting symmetry could be achieved in a narrow band of offset from the symmetry plane, which was not the desired working range. For this reason, a second part of the objective, f_2, named *Range Error*, was defined. This section takes into account the error of the endpoint displacement with respect to the desired working range, which was set in this case to $+12\,\text{cm}$ in the y direction and $\pm 4\,\text{cm}$ in the x direction (see Fig. 2.1). The denominator for each part of the total objective function is selected based on the number of vector differences in each part to make an unweighted summation of the two parts, f_1 consists of 7 displacement differences, so this part was divided by 7, and f_2 consists of 3 displacement differences, with similar logic, it was divided by 3. The formula for f_{total} was defined as

$$\begin{aligned}
&f_{\text{total}} = f_1 + f_2 = f_{\text{symmetry}} + f_{\text{range}} = \\
&\frac{1}{7}\left(|dx_{\alpha=0}| + \sum_{\alpha=30,60,90}\left(|dx_{+\alpha} - dx_{-\alpha}| + \left|dy_{+\alpha} - dy_{-\alpha}\right|\right)\right) + \\
&\frac{1}{3}\left(\left|0.12 - dy_{\alpha=0}\right| + |0.04 - dx_{\alpha=90}| + |0.04 + dx_{\alpha=-90}|\right),
\end{aligned} \tag{2.1}$$

where α denotes the effective angle of F, and dx, dy, dz are displacements in the three coordinate directions. The optimization procedure was assigned to minimize the mentioned objective function by optimizing different sets of shape-related parameters along the beam.

2.2.3 Parameter optimization

In this work, the parameter optimization to form the beam in each of the iterations, was divided into two branches, the first branch contains parameters related to the beam's shape and the second set contains sectional parameters and orientations along the beam. The shape optimization was implemented in three steps: 1) a fixed-shape beam, 2) an optimized free-form shape beam, and 3) an optimized shape under a curved planar constraint.

The second set concerns the cross-section and has two possible conditions, 1) a beam with a circular section, which means that only the circular beam's radius was optimized, and 2) beam with an I-section where all sectional parameters and sectional orientations of control points were optimized, as shown in Fig. 2.2. The combination of these two sets made 3x2 beams (see Fig. 2.5). These six beams are described in the following subsections.

It is important to note that, since we used a beam model in the implemented FEM, the sectional dimensions were ultimately reduced to four main parameters, i.e., the area, the second moments of inertia about the two main axes, and the torsional constant. Thus, it might asked why we did not optimize parameters instead of sectional dimensions. However, these parameters are not independent, and thus, optimizing them directly as separate variables could lead to unfeasible results. For this reason, it was chosen to optimize the dimensional parameters of a prevalent section. Between those, the I-section was selected since changing its dimensions enables a large variety of combinations of these four principal beam parameters. However, as the optimization is essentially about determining a collection of four principal beam parameters ($A, I_{\mathrm{yy}}, I_{\mathrm{zz}}, J$), another non-bisymmeric section with a relatively low torsional constant can do the same task as the I-section.

Beam 1 - Circular section with fixed shape

This beam is the simplest beam with only one optimized parameter, and it was used as a benchmark for evaluating the effect of parameter optimization on the other beams. The shape of this beam (see Fig. 2.1) was chosen arbitrarily and parametrized as

$$(x, y, z) = (C_1 t^3,\ a - b(C_2 t - c)^2,\ C_3 t), \tag{2.2}$$

where t is the independent parameter ranging from 0 to 40, the constants a, b and c were chosen as $a = 1.5, b = 0.75, c = \sqrt{2}$, and the constants C_1, C_2 and C_3 were determined such that the end of the beam reaches the arbitrarily chosen coordinates described in subsection 2.2.1.

$$C_1 = \frac{X_e}{t^3}, \quad C_2 = \frac{\sqrt{\frac{a-Y_e}{b}} + c}{t}, \quad C_3 = \frac{Z_e}{t}. \tag{2.3}$$

The cross-section of this beam is a filled circular section. The radius was optimized to enhance the performance of the beam's working range and make it a comparable benchmark for the beams that will be discussed next.

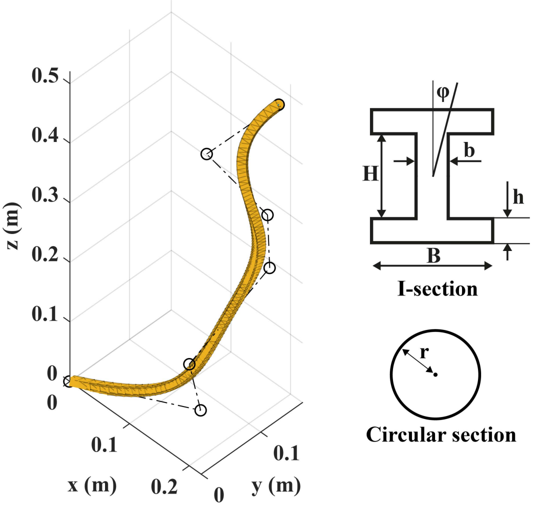

Figure 2.2: Each beam shape formed up based on a B-spline curve through control points and its sectional parameters.

Beam 2 - I-section with fixed shape

In the second beam, the dimensions and orientations of an I-section along the beam were subjected to the optimization, and the beam shape remained the same as it was described for Beam 1. The I-section was defined by their web height H, flange width B, flange thickness h, web thickness b, and the section orientation φ (see Fig. 2.2). The first four parameters were subjected to optimization once for the whole beam. The orientations were optimized at five control points, and all the other sectional orientations along the beam were interpolated based on the values of those five points.

Beam 3 - Circular section with optimized shape

The beam shape's optimization process was based on finding the best positions of intermediate control points to form the beam shape. The shape was made based on a B-spline between the grounding point and the endpoint described in subsection 2.2.1, concerning the optimized intermediate control points. The positions of all other nodes along the beam were interpolated from this B-spline, and together they made the shape of the beam. Theoretically, it was possible to choose any number of control points to make this spatially curved line. Here, we used five control points in the design space.

Bounds on the search space were applied to avoid the shape crossing itself or going out of the design space. The section of Beam 3 is again a filled circle, with one optimized radius. It is important to note that in all beams, the optimization process for section and shape parameters was performed simultaneously. Here, in Beam 3 a set of sixteen parameters, including three coordinates for five control points and one radius, were optimized.

Table 2.1: Sectional parameters and control points coordinates resulting from the optimization procedure which forms beams as shown in Fig. 2.2.

		Beam 1			Beam 2			Beam 3			Beam 4			Beam 5			Beam 6		
			Cir. Section Fix Shape			I-section Fix Shape			Cir. Section Opt. Shape			I-section Opt. Shape			Cir. Section Cons. Shape			I-section Cons. Shape	
Sec. Dimensions	Radius (mm)		5.40			-			5.50			-			5.52			-	
	Web Height (mm)		-			5.75			-			8.00			-			7.98	
	Flange Width (mm)		-			6.77			-			11.70			-			8.00	
	Flange Thick. (mm)		-			2.67			-			1.89			-			2.97	
	Web Thick. (mm)		-			5.38			-			4.39			-			4.00	
		x	y	z	x	y	z	x	y	z	x	y	z	x	y	z	x	y	z
C.P. Coordinates	Control Point 1 (mm)		-			-		80	120	79	196	23	74	135	31	79	4	28	88
	Control Point 2 (mm)		-			-		118	137	158	187	13	152	136	60	157	177	149	176
	Control Point 3 (mm)		-			-		123	138	240	191	14	224	121	116	238	177	149	264
	Control Point 4 (mm)		-			-		122	138	329	189	14	313	109	127	326	177	149	297
	Control Point 5 (mm)		-			-		93	127	421	144	86	423	96	118	416	62	108	462
Sec. Orientations	Orientation 1 (deg)		-			85.9			-			60.1			-			83.0	
	Orientation 2 (deg)		-			86.0			-			128.3			-			62.9	
	Orientation 3 (deg)		-			86.0			-			148.6			-			14.4	
	Orientation 4 (deg)		-			86.0			-			35.6			-			150.8	
	Orientation 5 (deg)		-			86.0			-			23.0			-			29.2	

Beam 4 - I-section with optimized shape

This beam was made up of a combination of both the mentioned procedures for shape optimization and sectional parameter optimization, which made it the most advanced beam among all six. These two sets of parameters were optimized together and enable control of all possible shape parameters of this scheme. A matrix consisting of three coordinates for each of five control points and a set of four variables for sectional dimensions and five parameters for orientations of sections were optimized together. These twenty four parameters together formed the beam's shape.

Beam 5 - Circular section with optimized shape on planar constraint

In several applications, using the whole volume between grounding and endpoint is not viable due to design restrictions. This is the case in, e.g., assistive devices where the human body is obstructed, or in applications like robots and machines, where there might be some objects in between the grounding locations and the endpoint. In those cases, constraining the available space for the optimizer is part of the procedure. In this work, an extruded ellipse was chosen as the curved planar constraint, and the shape was formed on it. The formula for the ellipse constraint was defined as

$$\frac{(x-0.2)^2}{0.2^2}+\frac{y^2}{0.15^2}=1, \tag{2.4}$$

using this equation reduces the set of three Cartesian coordinates for each control point to two since either x or y can be derived from it. Hence, the number of optimized parameters that was sixteen for Beam 3 will be reduced to eleven for this beam.

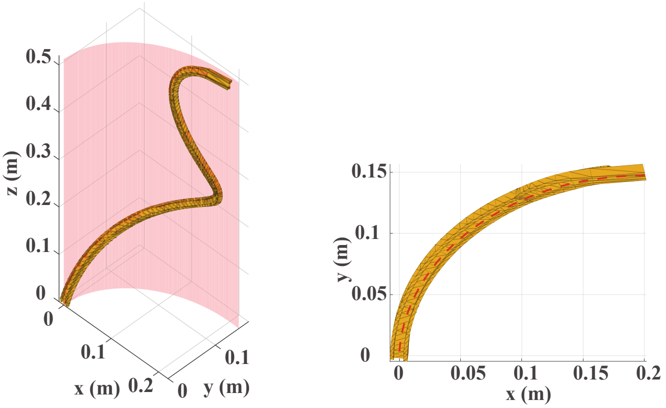

(a) **(b)**

Figure 2.3: The isometric and top view of a beam of which the shape is constrained to be on an curved plane as described in equation 2.4.

Beam 6 - I-section with optimized shape on planar constraint

The procedure for this beam was like Beam 4, only with two instead of three coordinates for control points to meet the constraint defined in equation 2.4. It is important to note that in this beam, not only the control points, but also all other interpolated points along the beam were defined to obey this equation to keep the beam shape always on this extruded ellipse constraint, as can be seen in Fig. 2.3.

2.2.4 Optimization process and finite element model

A degree-four B-spline was used to interpolate the shape and the sectional properties based on the optimized control points. The B-spline was chosen to have an open uniform knot vector to ensure that the first and last optimized control points coincide with the first and last parameters of the beam itself, which were the grounding and the endpoint. The internal knots were determined based on the de Boor algorithm [30] to equalize the weight of all control points. Using b-spline interpolation ensured a smooth transition between optimized parameters of the beam and avoided any discontinuities that could have happened due to sudden dimensional changes in the finite element model.

All the displacements under different loading conditions were derived from a self-developed finite element solver. The developed solver uses geometrically non-linear co-rotational beam elements. The mentioned beam elements were introduced by Battini [31], based on the Euler-Bernoulli formulation. This solver was selected as it can handle non-linearities due to large elastic deformations. Furthermore, having access to the source code of the solver made it an easier choice to tailor it for the aim of this work.

For the optimization process of the parameters, the *Multi Start* option from the Matlab® *optimization toolbox* was used. Five random starting points for the *fmincon* function with *Interior-Point* algorithm were set. With an objective function tolerance of $1e-5$, the maximum number of iterations is set at 100. Upper and lower bounds were used to keep the sectional parameters in a way to preserve the I-shape of the resulting sections and keep the beam shape inside the design space. The material constants for all beams were Young's modulus of $E = 200$ GPa and shear modulus of $G = 76.9$ GPa.

2.2.5 Experiments

For verification of the method's efficacy, the resulting beams' kinetostatic behavior has been checked with experiments. To make the results from this verification comparable with the results from the developed code, the same loading conditions from the objective function were implemented on the beams, and the errors were derived from the same objective function of equation 2.1.

All six resulting beams have been 3D-printed with the multi-jet fusion method and Polyamide 12 (PA12) as the print material. The beams have been scaled by 0.7 due to limitations in the printing size. To generate end point loads from different directions, the beam grounding was set to rotate about a horizontal axis. The load was exerted by known weights at the endpoint, which were always pointing vertically downward. The experimental setup is shown in Fig. 2.4(a). The resulting displacements have been extracted using vision-based measurement between the loaded and unloaded tip positions.

(a) **(b)**

Figure 2.4: (a) The experimental setup with a rotational clamp at the grounding point and a load at the endpoint. (b) A printed version of Beam 4 in seven loading angles where the beam base rotates instead of the endpoint load angle. The transparent beam shows the deformed state, and the solid beam shows the undeformed state.

2.3 Results

To evaluate the performance of the described method, the resulting objective functions of all beams with different optimized parameters are shown in Table 2.2.

To make the improvements in the kinetostatic behavior of different beams comparable, additional criterion based on the objective function is derived, denoted by Relative Improvement (RI) which is the improvement in each component of the objective function (symmetry and range) normalized by the average magnitude of the displacement vectors. This criterion is defined in order to exclude the effect of each beam's range of motion. The formulation of RI is defined as

$$\mathrm{RI} = f / \left(1/7 \left[\sum_{\alpha=0,\ \pm 30,\ \pm 60,\ \pm 90} \left\| \vec{d}_{\alpha} \right\| \right] \right). \tag{2.5}$$

The above numbers were compared with the RI values for Beam 1 as the benchmark, and the improvement of each beam is displayed in percentage in Table 2.2.

The first set of errors are directly resulted from the optimization procedure and self-developed finite element model. The second set was based on displacements obtained from the experiments.

Table 2.2: f_{symmetry}, f_{range}, and f_{total} (objective function) from beams 1 to 6, from the developed finite element model, and from experiments are shown. The relative improvement percentage for each part of the objective compared to the benchmark beam (Beam 1) are also shown.

		Beam 1	Beam 2	Beam 3	Beam 4	Beam 5	Beam 6
		Cir. Section Fix shape	I-section Fix shape	Cir. Section Opt. shape	I-section Opt. shape	Cir. Section Cons. shape	I-section Cons. shape
Dev. Beam Model	f_{symmetry} (mm)	6.2	5.3	5.2	1.5	5.3	3.7
	f_{range} (mm)	27.6	7.2	26.6	0.4	26.6	3.1
	f_{total} (mm)	**33.7**	**12.4**	**31.9**	**1.9**	**31.9**	**6.8**
	Rel. Symm. Improv.	0%	53%	22%	88%	20%	69%
	Rel. Range Improv.	0%	86%	10%	99%	11%	94%
Experiments	f_{symmetry} (mm)	5.1	16.7	5.1	3.4	6.2	4.6
	f_{range} (mm)	36.3	4.1	31.4	11.9	29.9	13.1
	f_{total} (mm)	**41.4**	**20.8**	**36.5**	**15.3**	**36.1**	**17.7**
	Rel. Symm. Improv.	0%	-24%	12%	68%	-3%	53%
	Rel. Range Improv.	0%	96%	25%	85%	31%	81%

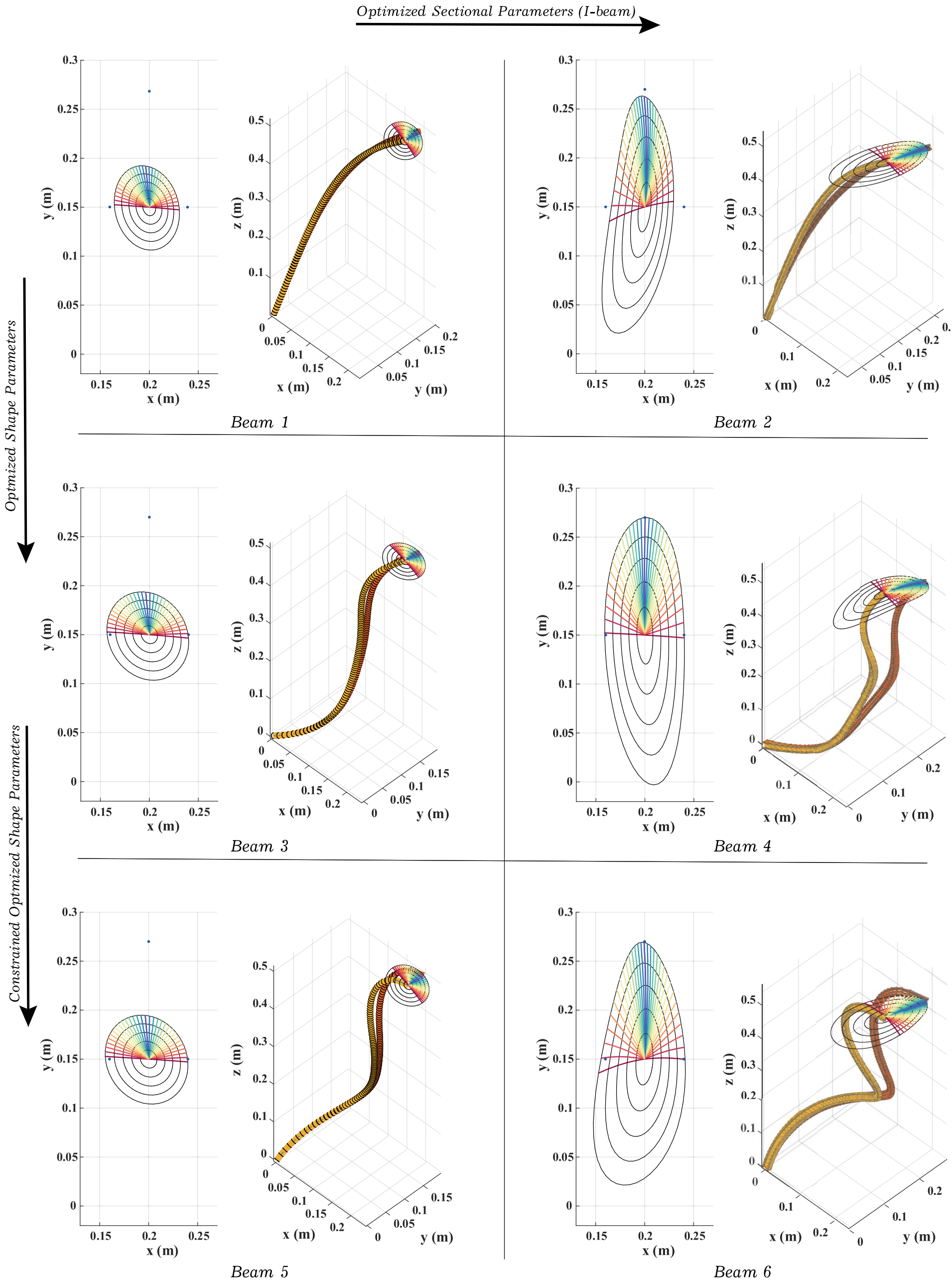

Figure 2.5: The Isoforce and Mirrored-force mapping of the resulting beams in the desired range, and the Isometric view of undeformed (yellow) and deformed (orange) shape of the beam under 100 N force in Y direction. All beams are defined based on the optimized parameters described in Table 2.1.

The isometric and top views of the resulting beams are shown in Fig. 2.5. To represent the kinetostatic behavior, in the field of action, an isoforce mapping at the endpoint of the beam is presented with black lines, which represents the displacement of the endpoint under the constant magnitudes of the force $F = 20, 40, 60, 80, 100\,\mathrm{N}$ and a full cycle of the angle α. The mirrored colored lines represent the endpoint path under increasing force from zero to 100 N with mirrored angles $\pm\alpha$ shown in the same color. The isoforce mapping together with the colored mirrored loading mapping can indicate the symmetry in the working range of the beams. The blue dots show the desired endpoint position for $\alpha = \pm 90^\circ$, 0° under 100 N loading. In the isometric view, the undeformed (yellow) and deformed (red) configurations are shown for $\alpha = 0^\circ$ and $F = 100\,\mathrm{N}$. The final optimized parameters of all beams are given in the Table 2.1.

2.4 Discussion

Analysis of the objective functions in Table 2.2 and comparing the errors with Beam 1 as the benchmark, shows the effect of tuning different sets of shape-related parameters on achieving desired symmetric behavior in an extended range of motion. Better results were achieved when more parameters were subjected to the optimization process. Furthermore, in Fig. 2.5 it can be recognized that in comparison with Beam 1, almost all beams exhibited a straighter path of the endpoint subject to a force in the y-direction ($\alpha = 0^\circ$).

It is fair to note that the anisotropic stiffness in X and Y directions, defined as the range error, has not been achieved with circular cross-sections. Hence, using non-circular cross-sections, or sections with different second moments of inertia about the two main axes, tends to make up for the anisotropy and contributes to favorably agreeable results.

Comparing the results from six optimized beams shows that having more freedom to tune the shape has a lower effect on achieving exceptional results on its own. On the other hand, having more freedom to tune the cross-section, effectively enhances the desired behavior. After all, combining these two led to a performance leap to achieve symmetric kinetostatic behavior. It is obvious that a solid conclusion on the exact effect of each optimized parameter needs more investigation of a possibly larger variety of beam parameters.

The logic behind the defined objective function can be used for other applications where anisotropic stiffness plus another feature like symmetry is needed. Here, the effect of the two parts of the objective function was chosen to be equal. However, it might be possible to achieve better results for specific requirements with a different weight ratio for f_1 and f_2. Furthermore, each part of the objective function might be improved. For instance, for the symmetry part f_1, it is possible to use more than three paired loadings, which might lead to better symmetry. However, it also has the negative effect of increasing computational time.

Our previous work [29] demonstrated that increasing the number of optimized cross-sections does not always lead to better values for objective, while making the problem computationally more expensive. However, the optimal number of control points for the best result may vary in different settings and cases, and this was not the focus of this study. Analysis can be performed to determine this optimal number for each set of requirements.

There are limitations in the self-developed beam model due to its assumptions. Relieving these limitations, which suppress all sectional deformations, e.g., warping and in-plane deformations, and using the same parameter optimization approach can lead to more complex deformed shapes and possibly more accurate results. However, advancing the mechanical model has not been the topic of investigation here, and the experiments shows that the current model is still valid for the desired loading conditions of this work.

There are several sources of error that might affect the experimental results. Beam fabrication is one of the sources where up to 0.08 mm deviation from the CAD model of the beam is observed in printed prototypes. Another source of error is the load angle of the beam, where up to 0.5 degrees of error was possible in the fixation of the base rotary stage, which affected the loading angle. The position of the endpoint load was assumed to be fixed at the tip hole of the beam. However, deviation from this location was observed in the different angles of the loading. Correction was applied to the experimental pictures due to camera lens distortion. Still, the image processing and correction might have caused some errors in the measurements. The rotary stage is connected to the base with rigid bars, and processing images in unloaded and loaded states shows no measurable deformation of the base. Thus, the beam grounding point can be assumed to be rigid.

Despite the fact that it was anticipated that these two sets of results would differ due to the discussed inaccuracies in the finite element model and potential experimental errors, it is not possible to determine the relative contribution of each to the final deviation of the measurements from the simulation. However, the patterns are identical generally. Consequently, it might be argued that the chapter's message remains legitimate.

It is clear that the resulting beams are not the best possible solution to this problem due to the limited number of available parameters. However, we can state that the presented beam parameter optimization scheme undoubtedly enhanced the desired symmetrical behavior. A similar approach can be applied to an arbitrarily defined kinetostatic behavior for other types of structures with different sets of available parameters.

The combination of parametrization and optimization significantly reduces the input parameters for the whole design process, while using interpolation between those key parameters ensures a smooth transition to avoid discontinuities in the overall structure. Therefore, the proposed method can be assumed as an effective way for enhancement of other compliant structures' kinetostatic behavior.

2.5 Conclusion

This chapter investigates the tuning of different combinations of shape and sectional parameters of asymmetric beams toward enhanced symmetric kinetostatic behavior. An optimization scheme for parametrized beams with an objective function that enhances symmetry in an extensive range of motion was defined. Different sets of parameters representing divergent design conditions were subjected to the optimization. Rather complex shapes were found by this method, and 68% enhancement of the desired behavior was achieved based on experimental results.

The effectiveness of different parts of the method has been validated by comparing the experimental performance of resultant beams from this approach. It is stated that tuning shape and sectional parameters along a slender spatial beam can significantly enhance the desired kinetostatic behavior at the endpoint. The results also suggest solid connections between the availability of shape and sectional parameters for optimization and enhancement of the desired kinetostatic behavior.

The presented method effectively shows its capability to achieve symmetric kinetostatic behavior in the three-dimensional range of motion of the beam's endpoint. Such design requirements are not easily achievable with existing compliant mechanism design methods. Therefore, this method is an enrichment as a synthesizing method for compliant mechanisms, and it can facilitate the implementation of monolithic spatial compliant elements for other applications.

References

[1] M. Liao, G. Xu, and Y. Yang, "Geometrically nonlinear quadrature element analysis of spatial curved beams," *Engineering Structures*, vol. 209, p. 110004, 2020.

[2] V. Parlaktaş, "Spatial compliant constant-force mechanism," *Mechanism and Machine Theory*, vol. 67, pp. 152–165, sep 2013.

[3] G. Radaelli and J. L. Herder, "Study on the large-displacement behaviour of a spiral spring with variations of cross-section, orthotropy and prestress," *Mechanical Sciences*, vol. 9, pp. 337–348, oct 2018.

[4] S. Kok, G. Radaelli, A. A. Nobaveh, and J. Herder, "Neutrally stable transition of a curved-crease planar shell structure," *Extreme Mechanics Letters*, vol. 49, p. 101469, 2021.

[5] H. Kooistra, C. J. Kim, W. W. van de Sande, and J. L. Herder, "Shape optimization framework for the path of the primary compliance vector in compliant mechanisms," *Journal of Mechanisms and Robotics*, vol. 12, no. 6, 2020.

[6] A. A. Nobaveh, G. Radaelli, and J. L. Herder, "A design tool for passive wrist support," in *International Symposium on Wearable Robotics*, pp. 13–17, Springer, 2020.

[7] A. Dunning, J. Stroo, G. Radaelli, and J. Herder, "Feasibility study of an upper arm support based on bending beams," in *2015 IEEE International Conference on Rehabilitation Robotics (ICORR)*, pp. 520–525, IEEE, 2015.

[8] M. T. Pham, S. H. Yeo, T. J. Teo, P. Wang, and M. L. S. Nai, "Design and optimization of a three degrees-of-freedom spatial motion compliant parallel mechanism with fully decoupled motion characteristics," *Journal of Mechanisms and Robotics*, vol. 11, no. 5, p. 051010, 2019.

[9] L. L. Howell, S. P. Magleby, and B. M. Olsen, *Handbook of Compliant Mechanisms.* Somerset: Wiley, 1 ed., 2013.

[10] O. A. Turkkan, V. K. Venkiteswaran, and H.-J. Su, "Rapid conceptual design and analysis of spatial flexure mechanisms," *Mechanism and Machine Theory*, vol. 121, pp. 650–668, mar 2018.

[11] J. P. A. Nijssen, G. Radaelli, J. L. Herder, J. B. Ring, and C. J. Kim, “Spatial Concept Synthesis of Compliant Mechanisms Utilizing Non-Linear Eigentwist Characterization,” in *Volume 5A: 42nd Mechanisms and Robotics Conference*, American Society of Mechanical Engineers, aug 2018.

[12] P. Bilancia, G. Berselli, L. Bruzzone, and P. Fanghella, “A CAD/CAE integration framework for analyzing and designing spatial compliant mechanisms via pseudo-rigid-body methods,” *Robotics and Computer-Integrated Manufacturing*, vol. 56, pp. 287–302, apr 2019.

[13] A. Yellowhorse, J. Rommers, A. Amoozandeh, and J. L. Herder, “Methods for shape fitting in morphing compliant mechanisms,” in *International Design Engineering Technical Conferences and Computers and Information in Engineering Conference*, vol. 85444, p. V08AT08A021, American Society of Mechanical Engineers, 2021.

[14] J. B. Hopkins and M. L. Culpepper, “Synthesis of multi-degree of freedom, parallel flexure system concepts via freedom and constraint topology (fact)–part i: Principles,” *Precision Engineering*, vol. 34, no. 2, pp. 259–270, 2010.

[15] C. J. Kim, Y.-M. Moon, and S. Kota, “A building block approach to the conceptual synthesis of compliant mechanisms utilizing compliance and stiffness ellipsoids,” *Journal of Mechanical Design*, vol. 130, no. 2, 2008.

[16] L. L. Howell, A. Midha, and T. W. Norton, “Evaluation of equivalent spring stiffness for use in a pseudo-rigid-body model of large-deflection compliant mechanisms,” 1996.

[17] S. R. Deepak, M. Dinesh, D. K. Sahu, and G. Ananthasuresh, “A comparative study of the formulations and benchmark problems for the topology optimization of compliant mechanisms,” 2009.

[18] O. Sigmund, “On the Design of Compliant Mechanisms Using Topology Optimization,” *Mechanics of Structures and Machines*, vol. 25, pp. 493–524, jan 1997.

[19] B. Zhu, X. Zhang, H. Zhang, J. Liang, H. Zang, H. Li, and R. Wang, “Design of compliant mechanisms using continuum topology optimization: A review,” *Mechanism and Machine Theory*, vol. 143, p. 103622, 2020.

[20] J. Liu and Y. Ma, “Sustainable design-oriented level set topology optimization,” *Journal of mechanical design*, vol. 139, no. 1, p. 011403, 2017.

[21] P. Hu, L. Yang, and B. Li, “Skeleton-section template parameterization for shape optimization,” *Journal of Mechanical Design*, vol. 140, no. 12, p. 121404, 2018.

[22] S. Cho and S.-H. Ha, “Isogeometric shape design optimization: exact geometry and enhanced sensitivity,” *Structural and Multidisciplinary Optimization*, vol. 38, no. 1, p. 53, 2009.

[23] C. V. Jutte, *Generalized Synthesis Methodology of Nonlinear Springs for Prescribed Load-Displacement Functions.* PhD thesis, 2008.

[24] O. Weeger, B. Narayanan, and M. L. Dunn, “Isogeometric shape optimization of nonlinear, curved 3d beams and beam structures,” *Computer Methods in Applied Mechanics and Engineering*, vol. 345, pp. 26–51, 2019.

[25] K. Zhao and J. P. Schmiedeler, “Using rigid-body mechanism topologies to design path generating compliant mechanisms,” *Journal of Mechanisms and Robotics*, vol. 8, no. 1, p. 014506, 2016.

[26] G. Radaelli and J. Herder, “Gravity balanced compliant shell mechanisms,” *International Journal of Solids and Structures*, vol. 118, pp. 78–88, 2017.

[27] M. Tschiersky, E. E. Hekman, D. M. Brouwer, and J. L. Herder, “Gravity balancing flexure springs for an assistive elbow orthosis,” *IEEE Transactions on Medical Robotics and Bionics*, vol. 1, no. 3, pp. 177–188, 2019.

[28] J. Nijssen, G. Radaelli, C. J. Kim, and J. L. Herder, “Overview and kinetostatic characterization of compliant shell mechanism building blocks,” *Journal of Mechanisms and Robotics*, vol. 12, no. 6, 2020.

[29] A. A. Nobaveh, G. Radaelli, and J. L. Herder, “Asymmetric spatial beams with symmetric kinetostatic behaviour,” in *Symposium on Robot Design, Dynamics and Control*, pp. 247–254, Springer, 2020.

[30] J. Hoschek and D. Lasser, *Fundamentals of computer-aided geometric design.* A.K. Peters, 1993.

[31] J.-M. Battini, *Co-rotational beam elements.* PhD thesis, Royal Institute of Technology, Stockholm, Sweden, 2002.

3

Spatial beams with anisotropically variable stiffness

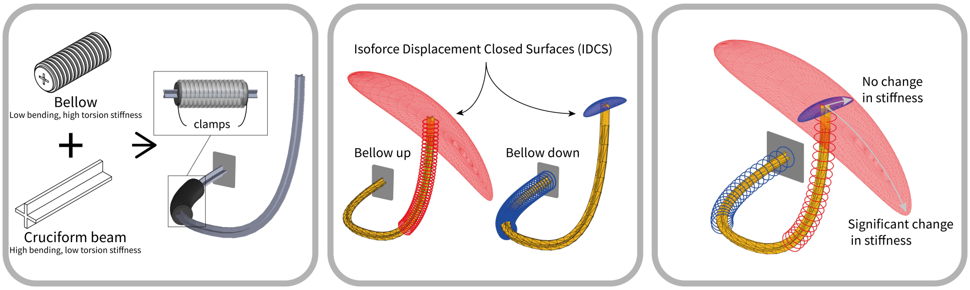

This chapter presents a concept to obtain variable kinetostatic behavior from the same type of beams, whose shapes were investigated in chapter 2, using variable boundary conditions. The results of the parameter optimization in the previous chapter showed that in spatial beams, the endpoint's kinetostatic behavior is heavily dependent on the torsional deformation of sections along the structure. Therefore, to change the endpoint's kinetostatic behavior, a possible solution would be local constraining of the torsion on the beam. To realize this, a short bellow is used as the stiffener of the covered part of the curved beam. It is shown that by changing the position of the bellow on the beam, the endpoint kinetostatic behavior changes. However, as the share of torsional and bending deformation of sections along the beam on the endpoint behavior is not the same in all directions, these changes of stiffness are shown to be anisotropic.

This chapter was published as:
Amoozandeh Nobaveh, A., Radaelli, G., van de Sande, W.W.P.J, van Ostayen, R.A.J., and Herder, J., 2022. Characterization of spatially curved beams with anisotropically adaptive stiffness using sliding torsional stiffeners. *International Journal of Mechanical Sciences*, 234, p.107687.

Characterization of spatially curved beams with anisotropically adaptive stiffness using sliding torsional stiffeners

Abstract *Compliant mechanisms (CM) with adaptive stiffness have been widely used in robotics and machine design applications. This chapter proposes a method for adapting the endpoint stiffness of a spatially curved compliant beam using a movable torsional stiffener and a new graphical characterization method for the resulting anisotropic stiffness of the endpoint for large deflections. A slender clamped-free cruciform beam with a predetermined spatial shape was utilized as the main compliant part, and a shorter sliding bellow was served as the torsional stiffener. The beam's endpoint displacements are mainly determined by its bending and torsional deformations. Therefore, the relocation of a bellow stiffener with high torsion and low bending stiffness along the described beam with relatively low torsion and high bending stiffness led to notable changes in the kinetostatic behavior at the endpoint. The share of bending and torsional stiffness of elements along the beam to endpoint stiffness varies depending on the direction. Experiments with arbitrarily chosen parameters of the current design reveal an anisotropically adaptive stiffness with 21.5 times more stiffness variations in one direction compared to the other. Effective characteristics for this behavior, such as the length and position of the bellow, were explored in an effort to improve it. To capture the effect of these parameters, the Isoforce Displacement Closed Surface (IDCS) was introduced as a new characterization method to visualize the nonlinear kinetostatic behavior of a CM throughout its three-dimensional range of motion. The IDCS was further used to elucidate how individual components of the current mechanism contribute to the system's overall kinetostatic behavior. Experiments were done on prototypes to confirm the changes in endpoint stiffness that were predicted by simulations.*

3.1 Introduction

Variable stiffness is a topic of interest in a wide variety of research fields. There are numerous examples in aerospace engineering, soft robotics, medical devices, smart materials, and wearable robotics. Despite the fact that these applications are different, the shared desired characteristic is that the designed devices must be able to alter their stiffness in a specified direction on demand.

In aerospace engineering, variable stiffness structures can be found in shape morphing applications [1–4]. Through shape morphing, wings can change their shape to become more efficient across various flight conditions. Kuder et al. [5] reviewed concepts for variable stiffness with a focus on shape morphing for aerospace applications, and Sun et al. [6] reviewed the same concept based on smart materials and structures.

Variable stiffness solutions were also explored in the field of soft robotics. Manti et al. [7] reviewed concepts for variable stiffness for application in this field. In soft robotics, the focus is mainly on using variable stiffness parts for the different phases of the interaction of soft robots with natural environments [8–10]. There are a handful of examples in soft robotics grippers which change the stiffness during different phases of grasping and handling the material using different techniques such as granular jamming, which can be defined as transition of granular media from fluid like to solid like state [11–13]. or layer jamming [14–16] and hybrid jamming which includes a combination of both techniques [17]

In medical applications, variable stiffness is a topic of interest mainly in surgical equipment where the stiff mode is used for cutting, grasping, or supporting other equipment while the soft mode is needed for traveling inside the body [18–20]. Blanc et al. [21] reviewed variable stiffness mechanisms for the application of medical devices.

In smart materials, taking advantage of variable stiffness can be the functionality basis of several proposed designs, where the effect of temperature or input voltage causes different stiffness characteristics of the structure [22, 23].

Adjusting stiffness can also be used in wearable robotics, where changing the stiffness of slender and lightweight structures is demanded to support different phases of human motion, e.g., different states of the upper body or limbs in their range of motion [24–26].

Numerous techniques for altering the stiffness of a system and characterizing these variations have been developed for a variety of applications. [27–30]. However, the majority of these techniques are designed in a complex and obtrusive manner. Still, in some applications, e.g., aerospace or wearable robotics, slenderness and being lightweight are key requirements. For instance, morphing aircraft wings using traditional mechanical actuators and mechanisms is often not viable due to the additional weight of these mechanisms [31, 32]. Similarly, the weight of wearable robots should be kept as low as possible to minimize the load that the user must bear [33–35]. On the other hand, these applications mostly need to perform relatively complex motion or support in three-dimensional space, which would commonly result in a complex assembly of several parts [36, 37]. However, adding complexities can wipe out the core functionality of the mechanism for these specific applications.

A spatial Compliant Mechanism (CM) could be used to address these types of intricate requirements for a relatively simple and slender system [38–41]. These mechanisms gain their motion as well as support the force from the elastic deformation of spatially curved parts [42, 43]. This type of CMs is still underexplored. A notable example of this type of topology is a clamped-free slender beam, in which the elements of the curved beam affect endpoint behavior [44], similar to an open chain robotic arm, in which the entire system contributes to end-effector behavior. Here, mainly the bending and torsional stiffness of elements along the beam contribute to the endpoint kinetostatic behavior. Hence, it is possible to use these parameters to adapt the endpoint stiffness. There are several examples in the literature, mainly focusing on changing the local bending stiffness of elements to adapt the overall stiffness of the system. Methods like layer coupling have been widely used [45–47], in these examples, a mechanism locally decouples layers to reduce the bending stiffness of the endpoint.

The majority of research cited thus far has focused exclusively on adapting a system's bending stiffness in order to design a planar mechanism. In spatial mechanisms, the endpoint behavior is not only dependent on the bending stiffness of elements along the shape but also strongly influenced by the torsional stiffness of these elements [48]. There is no doubt that by utilizing torsion as a primary stiffness tailoring tool in spatial mechanisms, higher and more sophisticated stiffness change ratios are achievable. However, implementing torsional stiffness changes has received little attention [49, 50].

In this chapter, adapting the endpoint stiffness of a spatially curved compliant clamped-free beam using a sliding torsional stiffener is investigated, and a new graphical characterization is proposed for the characterization of the resulting anisotropic stiffness of the endpoint for large deflections. It is shown that the endpoint secant stiffness under large deflections can notably change when the stiffener length and position on the beam alter. Two key compliant parts with contrasting mechanical behavior were used: a bellow as a torsional stiffener and a spatially curved prismatic beam with a cruciform cross-section as the base part. It is shown that the changes in the beam's endpoint stiffness are highly anisotropic. These changes in endpoint kinetostatic behavior were determined by different bellow configurations and then captured by the definition of a graphical characterization method, Isoforce Displacement Closed Surface (IDCS), and a metric, Displacement Change (DC). The IDCS was defined to visualize the nonlinear spatial kinetostatic behavior of the CM for large deflections. The definition of IDCS is not only beneficial for this work, but also it enables spatial CMs to be characterized, and the major effective design parameters of a spatial system to be identified. It can also be used to quantify the comparison of alternate solutions. The metric (DC) was defined as a quantitative measure for the change of stiffnesses in different configurations of an adaptive CM. Finally, experiments on prototypes were conducted to validate the simulation-based behavior.

The chapter is structured as follows. In Section 3.2, the concept for visualization of endpoint kinetostatic behavior is introduced. The definition of the problem and effective parameters together with the finite element solver are elaborated in section 3.3. Additionally, the context of experimental verification procedures is discussed. In Section 3.4 the resulting behavior from different conditions is shown. A discussion on the validity of the results and possible other applications and future improvements are given in Section 3.5, and the conclusion is given in Section 3.6.

3.2 Preliminaries

In this section, we present a concept for the visualization of the nonlinear kinetostatic behavior of a CM for large deflections by introducing *Isoforce Displacement Closed Line* (IDCL), and *Isoforce Displacement Closed Surface* (IDCS). An IDCL is obtained by loading a point of interest, typically the endpoint, of a CM by a force circle (see figure 3.1), meaning that a force ($\vec{F}$) of a constant magnitude is applied in a 360° sweep, and interconnecting all of the endpoint's displaced positions makes the IDCL. We have introduced this closed curve shape previously in [51].

With the same logic, an IDCS is the interconnection of all of the point of interest's

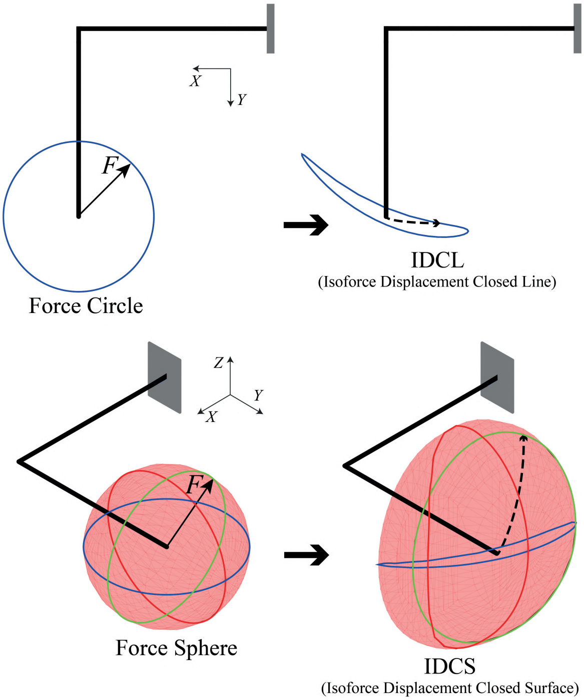

Figure 3.1: The top figures show the forming process of an L-shaped cantilever beam's *Isoforce Displacement Closed Line* (IDCL) from a tip force circle in the XY plane. The bottom figures show the forming process of the same beam's *Isoforce Displacement Closed Surface* (IDCS) from a tip force sphere in 3D. Three IDCLs are shown as closed curves on the IDCS. These IDCLs result from the force circles of the same color in the XY, XZ, and YZ planes. A force vector $\vec{F}$ is shown in solid black and its curved representative displacement path as a result of gradually increasing force $\vec{F}$ is also shown with dashed black.

deflected positions when it is loaded by a force sphere. It is worth noting that, an IDCL is a closed curve on the IDCS surface. Figure 3.1 shows the IDCS and three IDCLs of an 'L' shaped beam with a circular cross section. The IDCLs are the results of force circles on the XY, XZ, and YZ planes.

As is suggested in figure 3.1, the nonlinear displacement as a result of a force vector in a specific direction is not by definition in the direction of the force itself. Therefore, it is not valid to assume each point of IDCL and IDCS as a direct representation of the endpoint compliance in that direction. However, these graphical characterizations can clearly show the nonlinear kinetostatic behavior of a point of interest on a CM.

A similar concept for the characterization of the kinetostatic behavior of compliant building blocks was previously introduced by Kim et al. [52] as "compliance ellipsoids". The presented method in that work is analytical and easier to derive for simpler typologies, however, it only illustrates three main compliance vectors of a point of interest of a mechanism in each instance. Additionally, it only indicates the linear tangent stiffness. Thus, it is mainly effective for small deflections and it is not dependent on the magnitude of the force. In contrast, by employing IDCS, nonlinearities can be demonstrated; as a consequence, a change in force magnitude may result in a different IDCS.

In this study, the proposed graphical characterization method is used to demonstrate the spatial kinetostatic behavior of the beams' endpoints, as well as to elucidate variations in this behavior caused by different bellow configurations. This method of visualization can clarify the influence of torsional stiffening in the suggested combined design of the existing compliant mechanism. Noting that, as stated, we are proposing a method for changing stiffness and are not interested in a particular application for this method, it is essential to demonstrate changes in overall behavior that are not dependent on a particular application or direction; therefore, proposing this visualization is more important.

3.3 Methods

A slender cruciform clamped-free beam with a predetermined shape was used as the main compliant part, and a shorter bellow was employed as the torsional stiffener, as shown in figure 3.2(a). The bellow was sixty times stiffer in torsion than the beam, and its bending stiffness was approximately one-tenth of the beam bending stiffness. The bellow is only connected to the main beam with its side clamps. We hypothesized that altering the configuration of the bellows would result in significant changes in endpoint stiffness. To aid in the investigation of this mechanical behavior, various steps are detailed in this section.

The mechanism's topology and detailed parameters of the cruciform beam and bellow are discussed in the first step. The defined graphical characterization method for facilitating comprehension of changes in the beam's endpoint behavior in various bellow configurations is then elaborated. The details of implementing a geometrically nonlinear finite element beam model are discussed. Finally, the details of experimental beam prototyping and the test setup for verifying simulated results are elaborated.

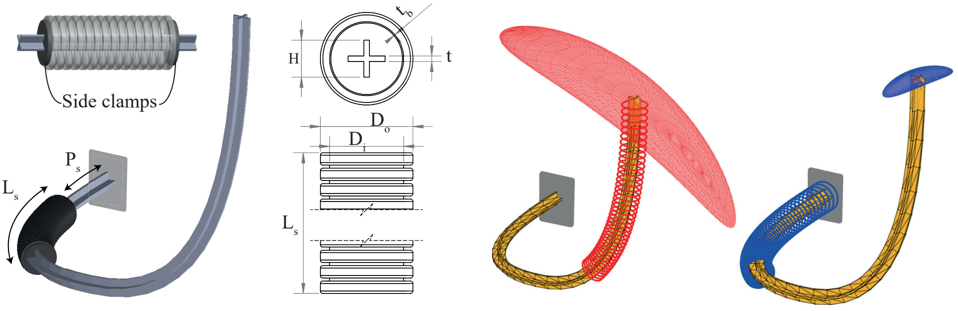

(a) (b)

Figure 3.2: (a) The cantilever cruciform beam and its movable torsional stiffener. The length of the sliding bellow is defined as L_s and its starting position on the beam named as P_s. The bellow is only connected to the beam with two thin clamps on the sides. (b) The Isoforce Displacement Closed Surface (IDCS) of the mechanism endpoint in two configurations of the bellow stiffener (red and blue).

3.3.1 Definition of topology

The cruciform beam was designed to be in a 1 m cube design space and have a spatial form. To make the shape of the beam extreme, the beam is set to move along all three principal axes. Therefore, the beam shape was formed in a way to travel the internal diagonal of a 1 m cube via its edges. However, following the cube corners could lead to sharp changes in the beam shape, which might lead to discontinuities in the finite element model, also stopping prismatic movement of the bellow along the beam. Therefore, to have a smooth shape for the beam, it was chosen to be formed based on a degree-two B-spline in which four corners of a 1 m cube were used as control points. The B-spline was chosen to have an open uniform knot vector of $[0, 0, 0, 0.5, 1, 1, 1]$. The position of the grounding point was assumed to be at the origin of the Cartesian coordinate system, and the beam endpoint was located at $[1, 1, 1]$. There were six different possibilities for the beam shape. The resultant shapes are shown in figure 3.3. A guide curve was determined to define the orientation of the cross-section in each point. Each beam section was set to be normal to the B-spline and the upper flange of the cruciform was designed to always point to the guide curve, which is shown in figure 3.3 with a red line. By defining this shape, we ensure that the beam is smooth enough for the bellow movement, and that it has parts oriented in the main Cartesian directions.

In the end, we selected only one beam out of all six possibilities, because the aim here was to capture the endpoint spatial behavior in different configurations of stiffener. After preliminary simulations, we discovered that the endpoint behavior of all six beam shapes follows the same pattern, meaning that all six beams show the same IDCS shape in a rotated or mirrored situation. Hence, we continued with only one beam out of six. The selected beam is shown in solid yellow in figure 3.3.

The bellow and cruciform cross-sectional dimensions, where the bellow length L_s was defined as a fraction of the main beam length L_b, are shown in figure 3.2(a). This figure also shows how the bellow was assembled on the beam by partially covering it. The bellow and beam connections, i.e., the side clamps in figure 3.2(a) were only on the sides of the bellow, where two circular parts with 2 mm thickness and a cruciform section cut were connected to the bellow sides. The bellow starting position from the beam base was labeled as P_s and it can slide on the beam. The value of P_s was expressed as a fraction of the main beam length and cannot be greater than $1 - L_s$ in order to accommodate the bellow on the beam. figure 3.2(b) depicts two different positions of a bellow (red and blue) and the resulting IDCSs.

3.3.2 Cruciform beam and bellow stiffener dimensions

As shown in figure 3.2(a), the dimensions of the cruciform section were $H = W = 0.06\,\text{m}$ in height and width and $t = 0.009\,\text{m}$ in thickness.

For the bellow there were two diameters $D_{\text{out}} = 0.15\,\text{m}$, $D_{\text{in}} = 0.12\,\text{m}$ and a uniform thickness $t_b = 0.0018\,\text{m}$.

3.3.3 Isoforce Displacement Closed Surface (IDCS)

It is essential to have an understanding of the endpoint spatial kinetostatic behavior to realize changes determined by different bellow configurations. For this reason, we used

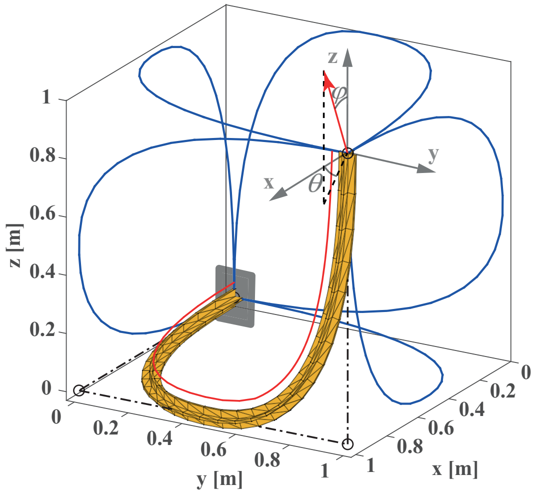

Figure 3.3: All possible shapes for the spatial cantilever beam traveling from $[0,0,0]$ to $[1,1,1]$ according to the defined B-spline and control points on the edges of a virtual 1*1*1 cube are shown with blue lines. The selected beam's shape from six possible shapes and its control points are demonstrated. The guide curve specifying cross-sectional orientation is shown with the red line. Also, a local spherical coordinate system is set up at the end of the beam to make it easier to show the direction of the tip force.

IDCS for different bellow positions and lengths. To implement the tip force sphere, a spherical coordinate system was defined on the endpoint, as shown in figure 3.3. The in-plane angle θ of $\vec{F}$ was changed in 10° steps from 0° to 350° to form IDCLs. This procedure was repeated in planes with 36 different φ from 0°to 175°to make an IDCS from 36*36 displaced states for each bellow configuration. The resulted IDCS of these points are shown in figure 3.7. The magnitude of force was chosen to be three Newton ($\|\vec{F}\| = 3\,\mathrm{N}$), this led to the maximum equivalent (von Mises) stress of 32.8 MPa, which is below 68% of the yield stress (48 MPa) of the prototype material (PA-12). This force magnitude can be different for other materials and possibly lead to a bigger or smaller volume of IDCS.

3.3.4 Displacement Change (DC)

To have a clear quantified estimation of changes in the endpoint's stiffness, a metric was defined as *Displacement Change* (DC). This value was defined as the absolute magnitude of the displacement difference between two bellow configurations as a result of the same force vector ($\vec{F}$). To make this number dimensionless, we divided it by the base beam length (L_b). The formulation for so-called DC is:

$$DC = \frac{\left\| \vec{d}_i(\theta,\varphi) - \vec{d}_e(\theta,\varphi) \right\|}{L_b}, \tag{3.1}$$

where d_i and d_e are displacement vectors as a result of the initial and the end configurations of the bellow, and φ, θ are respectively polar and azimuthal angle of the exerted tip force.

Finding the directions of the maximum and the minimum DC could be an intriguing aspect of the kinetostatic change. For this reason, a search function was used to find the force direction (θ, φ) among all 36*36 deformed states, which led to the Highest Displacement Change, HDC, and the Lowest Displacement Change, LDC, (see Fig. 3.4).

To find DC, we always compared two different positions of the same bellow. As the bellows had the lowest effect when they were placed at the top end of the beam, we always calculated HDC and LDC between the highest possible position of the bellows (P_{s_e}) as the benchmark and other positions (P_{s_i}). It is important to mention that the bellow was designed to always remain on the beam, hence, P_{s_i} could only range from 0 to $1 - L_s$ while P_{s_e} (benchmark configuration) was always equal to $1 - L_s$.

The HDC direction can be interpreted as the direction where the endpoint behavior is affected most by changes in bellow position, and with the same logic, the LDC direction is the direction where changes in bellow have the least kinetostatic effect.

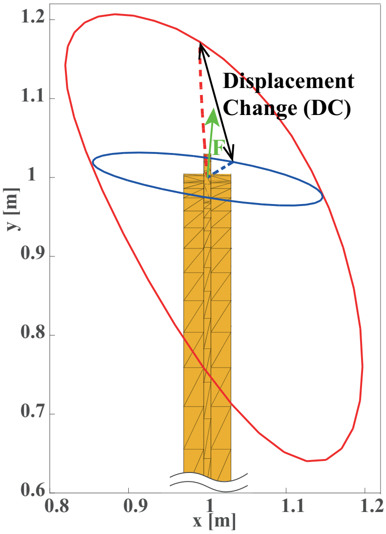

Figure 3.4: The figure shows two Isoforce Displacement Closed Lines (IDCLs) for two bellow configurations (red and blue lines), and the displacement paths as a result of gradually increasing force $\vec{F}$ for each bellow configuration with dashed red and blue. Displacement Change (DC) is the magnitude of the difference between these two displacement vectors.

3.3.5 Finite element modeling

To simplify the model in finite element analysis, the parts of the beam covered by the torsional stiffener have been replaced by elements with the combined stiffness of the beam and stiffener. To obtain the IDCS, we needed to find the combined beam's endpoint displacements under 36*36 different loading vectors, and do this for each bellow configura-

tion. Also, most of these loadings lead to large deformations. Hence, a relatively fast self-developed beam model was implemented. The solver uses geometrically nonlinear co-rotational beam elements, which were introduced by Battini [53], this model has been further explained in detail in [51].
A mesh converged solution with 30 elements for the beam length was used. As it mentioned the bellow stiffening effect were modeled by multiplying the I_{yy}, I_{zz} of bellow covered elements by 1.13 and their J by 60.8 regarding the data in table 3.1. For different lengths of the bellows the number of covered elements was changed. 15, 10 and 5 elements respectively for long, medium, and short bellows, and for different heights of the bellow on the beam, the starting stiffened element was changed.

It is important to note that, we are employing the described finite element model as a tool in our work, as it is a well-established gold standard model and performs sufficiently for this application. It is clear that alternative more advanced models can also be used with the same visualization and layout as those described in this study.

Both the bellow and the cruciform beam were modeled as 3D Euler-Bernoulli beam. Therefore, all dimensions were ultimately reduced into four main beam parameters: area, second moment of inertia in the two main directions, and torsional constant. Based on the dimensions and the preliminary experiments, the parameters for modeling these two components are mentioned in table 3.1.

Table 3.1: The parameters for the bellow and the beam.

	Beam	Bellow
Area (m^2)	9.99e-4	4.48e-4
I_{yy} (m^4)	1.65e-7	2.23e-8
I_{zz} (m^4)	1.65e-7	2.23e-8
J (m^4)	2.64e-8	1.56e-6

For finding the Young's modulus (E), we conducted preliminary experiments on the bellow and beam prototypes. These tests resulted in $E = 1.17\,\mathrm{GPa}$. By using the Poisson's ratio of PA-12 [54], the shear modulus was calculated as $G = 0.41\,\mathrm{GPa}$ for both the beam and the bellow.

3.3.6 Experiments

To validate modeling results, an experimental setup was developed. The prototypes for the experiments were 3D-printed using the multi-jet fusion method with PA-12 as the material. The beams were down-scaled six times to fit within the printing volume.

The experiments included loading the endpoint in LDC and HDC directions obtained from simulations (see table 3.2), with $\overline{F} = 3\,\mathrm{N}/\mathrm{scale} = 0.5\,\mathrm{N}$, and capturing the undeformed and deformed states to find the experimental HDC and LDC (see figure 3.6).

Here, we used suspended weight as the load. This load was always pointing vertically downward. Therefore, to implement the load's different directions, the whole mechanism was clamped onto a universal rotational stage where the rotation of the beam's global coordinates in θ and φ represented the changes in endpoint load direction. The experimental setup is shown in figure 3.5.

The three-dimensional displacement in the loaded and unloaded states were obtained by tracking the displacement of the endpoint marker in images that were taken from two perpendicularly located cameras.

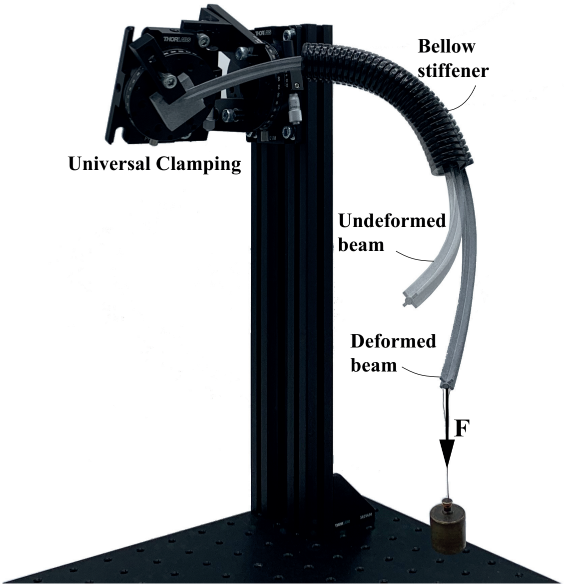

Figure 3.5: The experimental setup with a suspended-weight represents the constant magnitude of the tip force and a universal joint at clamping to represent the changes in load direction. The spatial displacement of the endpoint was measured using image processing of unloaded and loaded states from two perpendicular angles.

3.4 Results

To understand the effect of torsional stiffener length, three different bellows were chosen with their length (L_s) indicated as a fraction of the main beam length (L_b). The bellow lengths were selected to be 1/2 (long), 1/3 (medium), and 1/6 (short) of L_b. Besides the length of the bellow, the effect of its starting position (P_s) was also investigated.

The resultant HDC and LDC of these different positions are shown in figure 3.6 with thick dashed lines for HDC and thick solid lines for LDC. The directions of the forces for LDC and HDC in different configurations are shown in table 3.2. It is clear that with a longer bellow, the range of motion for the bellow becomes shorter. Hence, in figure 3.6 the horizontal axis (P_s) for longer bellow is shorter.

In addition, for each of the three bellow lengths in figure 3.7 (a, c, e), we have also shown the IDCS of the two most extreme positions ($P_s = 1 - L_s, 0$). In the same figure, the displacement path of the beam in two configurations with HDC (dashed lines) and LDC (solid lines) are also shown (b, d, f). The blue and red lines and surfaces are for the blue and red configurations of the bellows.

Table 3.2: The directions of the force to obtain the Lowest Displacement Change (LDC) and the Highest Displacement Change (HDC) in different positions of the bellow ($P_s = 0 - 0.7$). θ and φ are resulted from modeling and used for the experiments. The resulted HDC, LDC, and HDC/LDC from experiments are also shown for all bellow lengths (long, medium and, short).

$P_{s(\text{position})}$	Long							Medium							Short						
	LDC			HDC			HDC/LDC	LDC			HDC			HDC/LDC	LDC			HDC			HDC/LDC
	direction		LDCe-2	direction		HDCe-2		direction		LDCe-2	direction		HDCe-2		direction		LDCe-2	direction		HDCe-2	
	θ	φ		θ	φ			θ	φ		θ	φ			θ	φ		θ	φ		
0	40	50	5.8	110	150	**30.9**	5.3	50	45	1.2	120	160	**25.4**	21.5	50	40	2.3	90	160	**11.1**	4.7
0.1	70	30	7.5	130	155	**21.6**	2.9	70	30	3.7	150	160	**19.5**	5.2	50	40	1.8	130	165	**7.4**	4.1
0.2	70	30	6.0	150	160	**6.9**	1.2	90	20	2.0	160	145	**7.8**	3.9	70	30	0.3	150	160	**2.0**	7.5
0.3	90	20	2.0	160	145	**3.7**	1.8	90	20	3.3	170	130	**8.4**	2.5	90	20	0.7	180	140	**6.0**	8.3
0.4	80	30	1.3	170	130	**1.5**	1.2	90	20	0.9	180	115	**5.3**	6.1	90	10	1.7	180	120	**3.1**	1.8
0.5								280	30	1.4	180	110	**1.4**	1	90	20	0.7	180	110	**1.9**	2.6
0.6															280	30	0.2	180	115	**0.7**	4.7
0.7															280	30	0.2	180	120	**1.7**	8.5

3.4.1 Experimental results

Experiments were used to determine the displacements of the mechanism with various bellow configurations. The mechanism displacements were found in discrete positions and normalized based on the length of the prototype beam to be comparable with modeling results. The resultant DCs from experiments are shown with an asterisk (*) in figure 3.6. To make the experimental results trend comparable with the simulation results, the data points are connected with the thin dashed (HDC) and thin solid (LDC) lines.

A Normalized Root Mean Square Error (NRMSE) is used for each set of experimental results to show the difference with finite element results. For normalization of the RMSE, each set of results is divided by its “max value - min value”. Table 3.3 shows the NRMSE for different sets.

Table 3.3: The Normalized Root Mean Square Error (NRMSE) for different sets of experimental results compared to finite element results. The errors for long, medium, and short bellows, in the Lowest Displacement Change (LDC) and the Highest Displacement Change (HDC) are shown.

	Long		Medium		Short	
	LDC	HDC	LDC	HDC	LDC	HDC
NRMSE	16.2%	8.2%	8.6%	7.7%	5.5%	27.9%

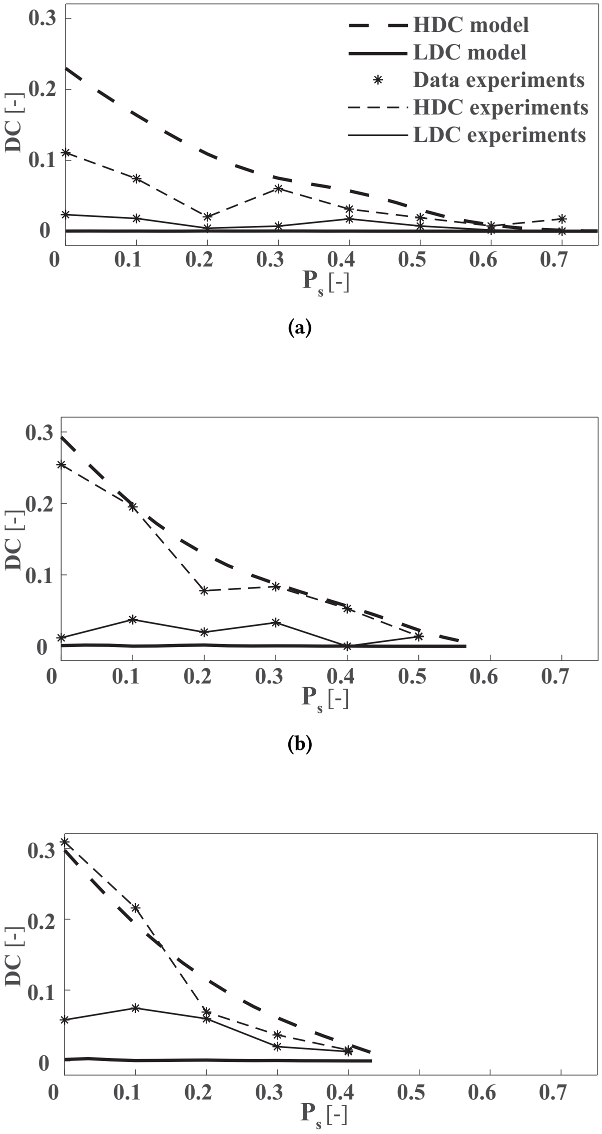

(a)

(b)

(c)

Figure 3.6: Displacement Change (DC) as a result of the same magnitude of force in the Lowest DC (LDC, solid lines) and the Highest DC (HDC, dashed lines) directions upon different bellow positions (P_s). Figures (a),(b),(c) are respectively for short, medium, and long bellows.

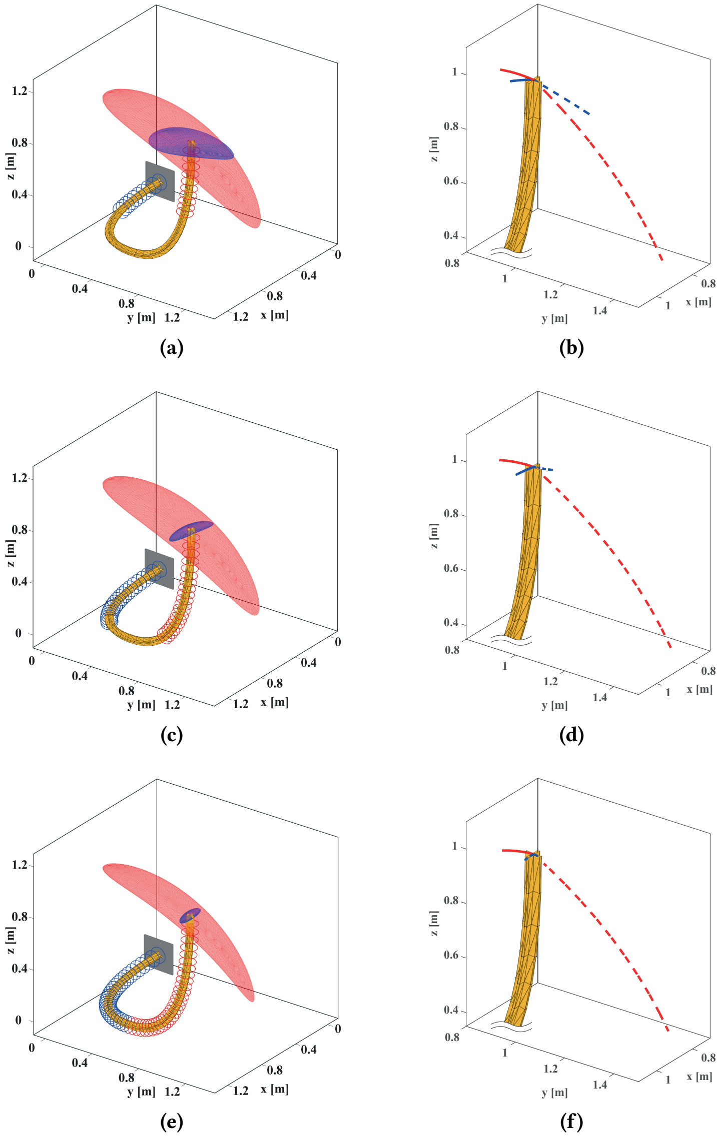

Figure 3.7: The left figures show the resulting Isoforce Displacement Closed Surfaces (IDCSs) for two positions of the bellow, on top and bottom of the beam. Blue IDCS is for the bottom blue position, and red IDCS is for the top red position of the bellow. The right figures show the displacement path of the endpoint for the same two positions of the bellow on the top and bottom, where the blue lines are for the bottom position and the red lines are for the top position of the bellow. The displacement paths are shown for two different directions of the load in each of the two bellow position, HDC load direction (dashed lines) and LDC load direction (solid lines). The displacement paths are the result of gradually increasing loads in that direction. Figures (a, b), (c, d), (e, f) are respectively for short, medium, and long bellows.

3.5 Discussion

The results highlighted the effect of torsional stiffening on the endpoint behavior of the CM and the anisotropically adaptive stiffness that was achieved with this technique. It was shown that meaningful trends in the nonlinear kinetostatic behavior of the mechanism can be achieved by changing configurations of the bellow. These changes are further analyzed by the graphical characterization method and the metric, IDCSs and HDC, which were specifically defined to understand the behavior of spatial CM.

In figure 3.7, the difference between the IDCSs of the two configurations of the bellow, blue and red, becomes more significant as the length of the bellow increases. Also, from figure 3.6 it can be revealed that with longer bellows, we can achieve higher HDC. However, a shorter bellow has a greater travel range than a longer bellow, and it is more appropriate for having a fine control on the endpoint behavior. Hence, there is a trade off between having a higher stiffness change (longer bellow) or a wider range of adjustment (shorter bellow) when choosing the bellow length.

Figure 3.6 also shows that the effect of the change in bellow position is higher near the grounding of the beam. This nonlinear decrease in HDC is due to the fact that with the current topology of the clamped-free beam, the base elements are subjected to higher deformation due to larger moment arms, and their deformations have a larger effect on the endpoint displacement.

As anticipated, both figure 3.6 and 3.7 confirm that the changes in endpoint behavior are not isotropic. The reason behind this behavior can be explained by an example. If we imagine a tip force in the Y direction in figure 3.3 on the beam, it will cause bending of the Z and Y-oriented parts of the beam and torsion of the X-oriented part. Regarding the fact that the deformation of the endpoint is heavily dependent on the beam base and that the moments are higher in the base part. Therefore, the torsion in the X-oriented part of the beam plays the major role. Hence, by torsionally stiffening this part, we can expect higher overall stiffness of the endpoint in the Y direction.

If we imagine the same situation for a tip force in the X direction, it will cause bending in the Z-oriented and X-oriented parts of the beam and torsion in the Y-oriented part. However, we mentioned that the effect of the beam base (the X-oriented part) is much more important. Therefore, torsional stiffening of the beam base will not cause a significant change in stiffness for the endpoint in the X direction.

Regarding this explanation, we can state that, by torsional stiffening of the beam, the endpoint stiffness behavior changes significantly in the directions wherein the torsion of the base elements is dominant, namely the Y direction in figure 3.3 which causes the HDC direction, and it almost remains the same in directions where the bending of the base part is dominating, namely the X direction, which causes the LDC direction.

In figure 3.6, the solid LDC lines are representative of bending-dominated directions, where the overall stiffness of the structure remains almost the same, and therefore, the DC remains almost zero regardless of the length and position of the bellow. With the same logic, the dashed HDC lines are representative of torsion-dominated directions where the endpoint stiffness is affected significantly by the torsional stiffening caused by the bellow.

The experimental results arguably match the anticipated results from finite element modeling, and the highest achievable HDCs in two cases are comparable. The reason behind some mismatches can be found in different assumptions:

Firstly, in the finite element modeling, we assumed that the stiffened beam parts, i.e., beam parts that are covered by the bellow, can be replaced by beam elements with the combined stiffness of the beam and bellow, whereas in reality, the bellow is only connected to the beam on two side clamps. The modeling of this stiffening could be captured better by taking the bellow and beam as parallel elements between clamping points and constraining them only on the side clamps of the bellow.

Secondly, here we have used Bernoulli's beam model, which is a gold standard for this type of structure, but it cannot capture some forms of deformation, e.g., section deformation. Using a more advanced finite element model can lead to a lower mismatch between experiments and modeling. Furthermore, in the current model, increasing the number of simulations per each configuration of the bellow can improve the resolution of θ and φ for HDC and LDC directions.

Thirdly, there were sources of error in the measurement setup, e.g., the torsion of the beam curve and the bellow were not matched in all configurations. Moreover, with the current bellow-beam connection, there is still room for under-bending of the bellow and over-torsion of the covered part of the beam, which makes the model less valid and shows its effect mainly on the most extreme cases, i.e., LDC of the long bellow and HDC of the short bellow (Fig. 3.6(a) dashed line and Fig. 3.6(c) solid line).
Another source of error can be considered in the bending stiffness of the bellow, which was assumed to be linear. However, initial investigations have shown that in large deformations, the bellow exhibits bending stiffening and it shows nonlinear behavior.

Eliminating these major causes of errors can result in a better match between modeling and experiments. However, the current data already demonstrate the desired behavior, and the conclusion regarding the change of kinetostatic behavior remains sound.

Attention must be paid to the definition of what we are achieving in terms of changes in endpoint kinetostatic behavior as the displacement vectors are not in the same direction as the forces due to the coupled parameters in the endpoint stiffness matrix (see figure 3.1). Also, in most cases, as it is shown in figure 3.7(b,d,f), we observed a curved path and nonlinear deformation of the endpoint due to the large magnitude of the force. Hence, the arbitrarily selected magnitude of the endpoint force has an effect on the maximum achievable HDC/LDC, but the overall anisotropic adaptive stiffness behavior due to torsional stiffening of the spatial mechanism is present regardless of the force amplitude.

Here, torsional stiffening was selected as the primary way to achieve anisotropically variable behavior. It is possible to achieve this behavior for other types of spatial structures as well, e.g., thin-walled shells. Also, changing the torsional stiffness is possible with other methods.

The resulting anisotropic change in the displacement domain is an interesting effect that can be used in many ways, e.g., in exoskeletons or morphing wings, where the stiffness needs to be reduced in one direction but stay more or less the same in other directions.

The optimization of several arbitrarily selected parameters like the shape and cross section of the beam and its torsion to bending stiffness ratio can notably change the behavior of the mechanism and further enhance the DC and anisotropy of the system. Hence, it is possible to use this simple, effective technique to design and modify the endpoint characterization of other spatial compliant systems, specifically for applications where weight and slenderness are key requirements.

3.6 Conclusion

We have presented a method which allows for anisotropic changes of end point stiffness of a spatial CM. This is done by a novel combination of two contrasting parts: a clamped-free curved cruciform beam with relatively high bending and low torsional stiffness as the base structure, and a short bellow with low bending and high torsional stiffness as a prismatic torsional stiffener of the main beam.

A graphical characterization method has been introduced to investigate the three dimensional nonlinear changes of the mechanism's endpoint's behavior due to the variation of the length and position of the bellow. This visualization can further be used to characterize the kinetostatic behavior of other types of spatial CM.

21.5 times higher stiffness changes in one direction compared to the other was achieved in the experiments using this method. The simulated behavior was also verified by observing similar trend of changes with experiments with an averaged normalized RMS error of 12.5%.

This type of anisotropic adaptive stiffness can have several applications where changes only in one direction's stiffness are required while the other direction's stiffness should remain almost the same. A similar combination of contrasting elements can be used for other types of structures like thin-walled shells. It is also possible to implement optimization on effective parameters of the current design to further enhance the presented feature.

References

[1] S. Barbarino, O. Bilgen, R. M. Ajaj, M. I. Friswell, and D. J. Inman, "A review of morphing aircraft," *Journal of intelligent material systems and structures*, vol. 22, no. 9, pp. 823–877, 2011.

[2] G. A. Thuwis, M. M. Abdalla, and Z. Gürdal, "Optimization of a variable-stiffness skin for morphing high-lift devices," *Smart materials and structures*, vol. 19, no. 12, p. 124010, 2010.

[3] Z. Chen, X. Wu, Z. Wang, and J. Shao, "Concepts for morphing airfoil using novel auxetic lattices," in *International Conference on Aerospace System Science and Engineering*, pp. 265–274, Springer, 2019.

[4] F. Nicassio, G. Scarselli, F. Pinto, F. Ciampa, O. Iervolino, and M. Meo, "Low energy actuation technique of bistable composites for aircraft morphing," *Aerospace Science and Technology*, vol. 75, pp. 35–46, 2018.

[5] I. K. Kuder, A. F. Arrieta, W. E. Raither, and P. Ermanni, "Variable stiffness material and structural concepts for morphing applications," *Progress in Aerospace Sciences*, vol. 63, pp. 33–55, 2013.

[6] J. Sun, Q. Guan, Y. Liu, and J. Leng, "Morphing aircraft based on smart materials and structures: A state-of-the-art review," *Journal of Intelligent material systems and structures*, vol. 27, no. 17, pp. 2289–2312, 2016.

[7] M. Manti, V. Cacucciolo, and M. Cianchetti, “Stiffening in soft robotics: A review of the state of the art,” *IEEE Robotics & Automation Magazine*, vol. 23, no. 3, pp. 93–106, 2016.

[8] B. Fang, F. Sun, L. Wu, F. Liu, X. Wang, H. Huang, W. Huang, H. Liu, and L. Wen, “Multimode grasping soft gripper achieved by layer jamming structure and tendon-driven mechanism,” *Soft Robotics*, vol. 9, no. 2, pp. 233–249, 2022.

[9] G. B. Crowley, X. Zeng, and H.-J. Su, “A 3d printed soft robotic gripper with a variable stiffness enabled by a novel positive pressure layer jamming technology,” *IEEE Robotics and Automation Letters*, vol. 7, no. 2, pp. 5477–5482, 2022.

[10] D. D. Arachchige, Y. Chen, I. D. Walker, and I. S. Godage, “A novel variable stiffness soft robotic gripper,” in *2021 IEEE 17th International Conference on Automation Science and Engineering (CASE)*, pp. 2222–2227, IEEE, 2021.

[11] V. Wall, R. Deimel, and O. Brock, “Selective stiffening of soft actuators based on jamming,” in *2015 IEEE International Conference on Robotics and Automation (ICRA)*, pp. 252–257, IEEE, 2015.

[12] L. Al Abeach, S. Nefti-Meziani, T. Theodoridis, S. Davis, *et al.*, “A variable stiffness soft gripper using granular jamming and biologically inspired pneumatic muscles,” *Journal of Bionic Engineering*, vol. 15, no. 2, pp. 236–246, 2018.

[13] S. Hauser, M. Robertson, A. Ijspeert, and J. Paik, “Jammjoint: A variable stiffness device based on granular jamming for wearable joint support,” *IEEE Robotics and Automation Letters*, vol. 2, no. 2, pp. 849–855, 2017.

[14] Y. Gao, X. Huang, I. S. Mann, and H.-J. Su, “A novel variable stiffness compliant robotic gripper based on layer jamming,” *Journal of Mechanisms and Robotics*, vol. 12, no. 5, p. 051013, 2020.

[15] M. Zhu, Y. Mori, T. Wakayama, A. Wada, and S. Kawamura, “A fully multi-material three-dimensional printed soft gripper with variable stiffness for robust grasping,” *Soft robotics*, vol. 6, no. 4, pp. 507–519, 2019.

[16] L. Gerez, G. Gao, and M. Liarokapis, “Laminar jamming flexure joints for the development of variable stiffness robot grippers and hands,” in *2020 IEEE/RSJ International Conference on Intelligent Robots and Systems (IROS)*, pp. 8709–8715, IEEE, 2020.

[17] Y. Yang, Y. Zhang, Z. Kan, J. Zeng, and M. Y. Wang, “Hybrid jamming for bioinspired soft robotic fingers,” *Soft robotics*, vol. 7, no. 3, pp. 292–308, 2020.

[18] Y.-J. Kim, S. Cheng, S. Kim, and K. Iagnemma, “A stiffness-adjustable hyperredundant manipulator using a variable neutral-line mechanism for minimally invasive surgery,” *IEEE transactions on robotics*, vol. 30, no. 2, pp. 382–395, 2013.

[19] I. De Falco, M. Cianchetti, and A. Menciassi, “A soft multi-module manipulator with variable stiffness for minimally invasive surgery,” *Bioinspiration & biomimetics*, vol. 12, no. 5, p. 056008, 2017.

[20] A. Jiang, G. Xynogalas, P. Dasgupta, K. Althoefer, and T. Nanayakkara, "Design of a variable stiffness flexible manipulator with composite granular jamming and membrane coupling," in *2012 IEEE/RSJ International Conference on Intelligent Robots and Systems*, pp. 2922–2927, IEEE, 2012.

[21] L. Blanc, A. Delchambre, and P. Lambert, "Flexible medical devices: Review of controllable stiffness solutions," in *Actuators*, vol. 6, p. 23, Multidisciplinary Digital Publishing Institute, 2017.

[22] M. Baniasadi, A. Foyouzat, and M. Baghani, "Multiple shape memory effect for smart helical springs with variable stiffness over time and temperature," *International Journal of Mechanical Sciences*, vol. 182, p. 105742, 2020.

[23] A. Adeodato, B. T. Duarte, L. L. S. Monteiro, P. M. C. Pacheco, and M. A. Savi, "Synergistic use of piezoelectric and shape memory alloy elements for vibration-based energy harvesting," *International Journal of Mechanical Sciences*, vol. 194, p. 106206, 2021.

[24] G. Radaelli, E. J. Rosenberg, M. E. Aguirre, A. C. Verkuyl, and B. M. Wisse, "Wearable support structure and method of supporting a torso," Feb. 18 2020. US Patent 10,561,518.

[25] A. Dunning, J. Stroo, G. Radaelli, and J. Herder, "Feasibility study of an upper arm support based on bending beams," in *2015 IEEE International Conference on Rehabilitation Robotics (ICORR)*, pp. 520–525, IEEE, 2015.

[26] M. del Carmen Sanchez-Villamañan, J. Gonzalez-Vargas, D. Torricelli, J. C. Moreno, and J. L. Pons, "Compliant lower limb exoskeletons: a comprehensive review on mechanical design principles," *Journal of neuroengineering and rehabilitation*, vol. 16, no. 1, p. 55, 2019.

[27] S. Yuan, Y. Sun, M. Wang, J. Ding, J. Zhao, Y. Huang, Y. Peng, S. Xie, J. Luo, H. Pu, *et al.*, "Tunable negative stiffness spring using maxwell normal stress," *International Journal of Mechanical Sciences*, vol. 193, p. 106127, 2021.

[28] M. Doumit and J. Leclair, "Development and testing of stiffness model for pneumatic artificial muscle," *International Journal of Mechanical Sciences*, vol. 120, pp. 30–41, 2017.

[29] H. Akhavan, P. Ribeiro, and M. De Moura, "Large deflection and stresses in variable stiffness composite laminates with curvilinear fibres," *International Journal of Mechanical Sciences*, vol. 73, pp. 14–26, 2013.

[30] T. Jin, Z. Liu, S. Sun, Z. Ren, L. Deng, D. Ning, H. Du, and W. Li, "Theoretical and experimental investigation of a stiffness-controllable suspension for railway vehicles to avoid resonance," *International Journal of Mechanical Sciences*, vol. 187, p. 105901, 2020.

[31] X. Lachenal, S. Daynes, and P. M. Weaver, "A zero torsional stiffness twist morphing blade as a wind turbine load alleviation device," *Smart materials and structures*, vol. 22, no. 6, p. 065016, 2013.

[32] X. Lachenal, S. Daynes, and P. M. Weaver, "Review of morphing concepts and materials for wind turbine blade applications," *Wind energy*, vol. 16, no. 2, pp. 283–307, 2013.

[33] M. del Carmen Sanchez-Villamañan, J. Gonzalez-Vargas, D. Torricelli, J. C. Moreno, and J. L. Pons, "Compliant lower limb exoskeletons: a comprehensive review on mechanical design principles," *Journal of neuroengineering and rehabilitation*, vol. 16, no. 1, pp. 1–16, 2019.

[34] A. A. Nobaveh, G. Radaelli, and J. L. Herder, "A design tool for passive wrist support," in *International Symposium on Wearable Robotics*, pp. 13–17, Springer, 2020.

[35] L. Lin, F. Zhang, L. Yang, and Y. Fu, "Design and modeling of a hybrid soft-rigid hand exoskeleton for poststroke rehabilitation," *International Journal of Mechanical Sciences*, vol. 212, p. 106831, 2021.

[36] J. Hull, R. Turner, and A. T. Asbeck, "Design and preliminary evaluation of two tool support arm exoskeletons with gravity compensation," *Mechanism and Machine Theory*, vol. 172, p. 104802, 2022.

[37] S. Buccelli, F. Tessari, F. Fanin, L. De Guglielmo, G. Capitta, C. Piezzo, A. Bruschi, F. Van Son, S. Scarpetta, A. Succi, *et al.*, "A gravity-compensated upper-limb exoskeleton for functional rehabilitation of the shoulder complex," *Applied Sciences*, vol. 12, no. 7, p. 3364, 2022.

[38] G. Radaelli, *Synthesis of mechanisms with prescribed elastic load-displacement characteristics.* PhD thesis, Delft University of Technology, Delft, The Netherlands, 2017.

[39] G. Radaelli and J. Herder, "Gravity balanced compliant shell mechanisms," *International Journal of Solids and Structures*, vol. 118, pp. 78–88, 2017.

[40] M. Tschiersky, E. E. Hekman, J. L. Herder, and D. M. Brouwer, "Gravity balancing flexure spring mechanisms for shoulder support in assistive orthoses," *IEEE Transactions on Medical Robotics and Bionics*, vol. 4, no. 2, pp. 448–459, 2022.

[41] S. Kok, G. Radaelli, A. A. Nobaveh, and J. Herder, "Neutrally stable transition of a curved-crease planar shell structure," *Extreme Mechanics Letters*, vol. 49, p. 101469, 2021.

[42] P. Bilancia, G. Berselli, L. Bruzzone, and P. Fanghella, "A CAD/CAE integration framework for analyzing and designing spatial compliant mechanisms via pseudo-rigid-body methods," *Robotics and Computer-Integrated Manufacturing*, vol. 56, pp. 287–302, apr 2019.

[43] J. Nijssen, G. Radaelli, C. J. Kim, and J. L. Herder, "Overview and kinetostatic characterization of compliant shell mechanism building blocks," *Journal of Mechanisms and Robotics*, vol. 12, no. 6, 2020.

[44] O. Weeger, B. Narayanan, and M. L. Dunn, "Isogeometric shape optimization of nonlinear, curved 3d beams and beam structures," *Computer Methods in Applied Mechanics and Engineering*, vol. 345, pp. 26–51, 2019.

[45] C. Tridech, H. A. Maples, P. Robinson, and A. Bismarck, "High performance composites with active stiffness control," *ACS applied materials & interfaces*, vol. 5, no. 18, pp. 9111–9119, 2013.

[46] J. Ou, L. Yao, D. Tauber, J. Steimle, R. Niiyama, and H. Ishii, "jamsheets: thin interfaces with tunable stiffness enabled by layer jamming," in *Proceedings of the 8th International Conference on Tangible, Embedded and Embodied Interaction*, pp. 65–72, 2014.

[47] T. Wang, J. Zhang, Y. Li, J. Hong, and M. Y. Wang, "Electrostatic layer jamming variable stiffness for soft robotics," *IEEE/ASME Transactions on Mechatronics*, vol. 24, no. 2, pp. 424–433, 2019.

[48] F. P. Rad, G. Berselli, R. Vertechy, and V. P. Castelli, "Compliance based characterization of spherical flexure hinges for spatial compliant mechanisms," in *Advances on Theory and Practice of Robots and Manipulators*, pp. 401–409, Springer, 2014.

[49] W. Raither, A. Bergamini, and P. Ermanni, "Profile beams with adaptive bending–twist coupling by adjustable shear centre location," *Journal of intelligent material systems and structures*, vol. 24, no. 3, pp. 334–346, 2013.

[50] R. Ajaj, M. Friswell, W. Dettmer, A. Isikveren, and G. Allegri, "Conceptual modeling of an adaptive torsion wing structure," in *52nd AIAA/ASME/ASCE/AHS/ASC Structures, Structural Dynamics and Materials Conference 19th AIAA/ASME/AHS Adaptive Structures Conference 13t*, p. 1883, 2011.

[51] A. A. Nobaveh, G. Radaelli, and J. L. Herder, "Asymmetric spatial beams with symmetric kinetostatic behaviour," in *Symposium on Robot Design, Dynamics and Control*, pp. 247–254, Springer, 2020.

[52] C. J. Kim, Y.-M. Moon, and S. Kota, "A building block approach to the conceptual synthesis of compliant mechanisms utilizing compliance and stiffness ellipsoids," 2008.

[53] J.-M. Battini, *Co-rotational beam elements*. PhD thesis, Royal Institute of Technology, Stockholm, Sweden, 2002.

[54] M. Faes, Y. Wang, P. Lava, and D. Moens, "Variability in the mechanical properties of laser sintered pa-12 components," in *Proceedings of the 26th annual international solid freeform fabrication symposium. Solid freeform fabrication symposium*, pp. 847–56, 2015.

II

Twisting beams

4

A compliant transmission mechanism

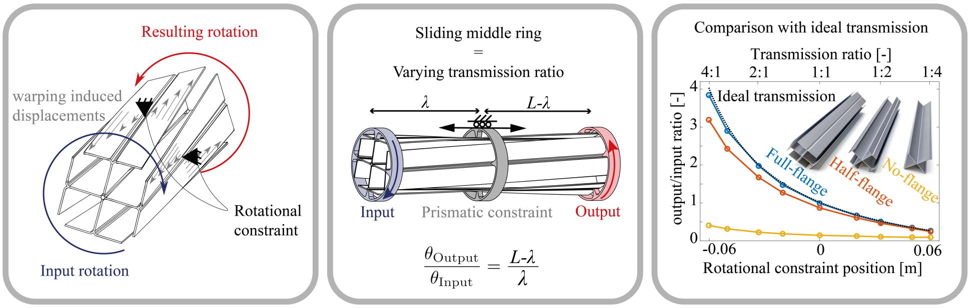

In part I, the kinetostatic behavior of spatially curved beams was investigated, and the torsional deformation was found to have a key effect on the endpoint's behavior of spatial compliant beams. In part II, other mechanical effects that can play a role in the propagation of torsion and the control of it in open thin-walled straight beams will be investigated. In this chapter, warping, a well-known effect in thin-walled structures, is utilized to transmit the torsion. It is shown that beams with a relatively high warping constant can work like a transmission mechanism and pass the sectional rotation over a rotational constraint to make the reverse rotation on the other side. The concept has been shown to have the possibility of also changing the transmission ratio between rotations of the sides of the beam, which makes it a compliant continuously variable transmission mechanism.

This chapter was published as:
Amoozandeh Nobaveh, A., Herder, J.L. and Radaelli, G., 2023. A compliant Continuously Variable Transmission (CVT). *Mechanism and Machine Theory*, 184, p.105281.

A compliant Continuously Variable Transmission (CVT)

Abstract *Continuously Variable Transmissions (CVT) can serve as subsystems for a variety of machineries and robotic systems. A compliant CVT mechanism based on the warping of twisting beams is presented here. The design works based on the demonstrated fact that the twist on one side of a beam can be transferred via sectional warping and propagate across a rotational constraint in the middle of the beam to create a reverse twist on the opposite side. In the proposed compliant CVT the transmission ratio is dependent on the position of the middle rotational constraint which can vary in a continuous range. We have demonstrated this concept and its relation to the twisting beam's warping constant, as well as its functionality for different transmission ratios of 1:4 to 4:1. An analytical model as well as a Finite Element Analysis (FEA) and experiments are employed to characterize and verify the concept and its relation to the warping constant.*

4.1 Introduction

A transmission mechanism is generally a complex, multi-element system. When a continuously variable transmission (CVT) ratio is required, an additional level of complexity might be anticipated. There are several designs for CVT systems, including half and full toroidal CVTs [1], magnetic CVTs [2], and belt- or chain- type CVTs. Designs of the latter type, which is the largest group of known CVTs, utilize two pulleys with variable diameters coupled to one another with a belt or chain [3].

Considering applications requiring light-weight mechanisms like aerospace engineering and wearable robots, using these conventional systems is not viable as they are rather bulky and complex. Also, for small-scale applications, such as sensors or micro robots, these conventional systems are inadequate because of fabrication and assembly problems. Apart from the fact that these mechanisms operate on the basis of contacts between numerous connected elements, which introduces inherent problems such as backlash and other contact-related errors that can reduce the applicability of these conventional variable transmission solutions for applications such as MEMS and micro manufacturing, clean (room) applications i.e., optics and extreme precision [4].

A compliant transmission mechanism is capable of resolving several of the concerns listed above. Due to the fact that these mechanisms operate via elastic deformation of elements rather than contact, issues such as backlash are not present. Additionally, these systems are predominantly monolithic, light-weight and easily fabricable. As a result, a compliant CVT can be used to construct devices such as tiny aerial robots [5], watch oscillators [6], and precision systems such as sensors, or any other application that does not require a full cycle rotation like walking mechanisms for humanoid robots [7, 8] or motion transferring for wearable robots [9].

Numerous examples exist of compliant transmission mechanisms [10–12]. However, these compliant transmission systems are mainly planar and were designed by substituting rigid body mechanism joints by compliant parts. As a result, the most of these mechanisms require a very large design area to accommodate the links, and in the majority of situations, linkages can only imply a fix transmission ratio. There are fewer instances of systems that allow for variable transmission ratios, but still in those designs, a reconfiguration of the whole mechanism is required in order to change the transmission ratio, which makes them even less space efficient [13, 14]. There are another type of these compliant transmissions in literature which can only switch between specified ratios; in other words, they are incapable of continuously covering a range of transmission ratios [15]. Apart from that, the aforementioned planar techniques were primarily created for translation to translation transmission.

To achieve rotation to rotation compliant transmission mechanisms, spatial compliant elements such as twisting beams can be used. Earlier, such an element was employed to morph shapes [16], and also for some compliant revolute joints [17, 18], where the bending to torsion stiffness ratio of the beam is crucial for representing joint-like behavior. Strategies such as balancing and prestressing are proposed to further increase this ratio for the joint functionality purposes. However, in non of these compliant twisting elements, designers looked at the possibility of using them as transmissions.

In this work, we use warping as an intrinsic property of a beam with an open thin-walled section, to obtain rotation–rotation transmission. Warping is usually regarded as an undesirable behavior, and designers try to minimize or avoid it. There are only a few applications, e.g., adjusting the effective angles of airplane wings [19], that take advantage of this principle. Warping, or in another words out of plane deformation of cross-sections, can be very effective as it causes axial displacements in a warpable beam. These axial displacements can propagate across an intermediate rotational constraint and cause exceptional effects like twist coupling along the beam, which can be considered a method to transmit the rotation between sides of a warpable beam. The transmission of warping in thin-walled structures is a well-established topic in structural engineering and there are several papers on characterization and possibly avoiding its propagation in the whole structure [20–22]. However, using this warping behavior to achieve a mechanism has only been proposed by the authors as a compliant differential mechanism with a one to one ratio [9, 23].

The purpose of this chapter is to present a concept for a compliant CVT mechanism that operates by twisting warpable beams. It is demonstrated that the rotation of one beam side can be transmitted by warping along the beam and passing across a rotational constraint in the middle of the beam to cause the opposite side to rotate in reverse. The ratio of the rotation angles at the input and output sides is dependent on the location of the intermediate rotational constraint. As a result, it is demonstrated that by repositioning the middle constraint a continuously variable transmission can be created. We have established and validated this concept using an analytical solution, finite element analysis (FEA) and experiments on the beam prototypes with different warping constants in order to demonstrate the effect of warping on this transmission behavior.

The chapter is structured as follows. In Section 4.2, the concept, and the reasoning behind the captured behavior are introduced. The effective design parameters together with the details of the analytical solution, the FEA and the experimental setup are elaborated in Section 4.3. In Section 4.4 the results for all beams and from different methods are shown. A discussion on the validity of the concept and the results, beside possible applications and improvements are given in Section 4.5. Finally, a brief overview of the achievements and possible applications are stated in Section 4.6.

4.2 Concept Overview

When a beam with a high warping constant is loaded in torsion, the cross-sections deform in the axial direction of the beam. In other words plane cross-sections are not planar anymore (Fig. 4.1) [24]. These warping induced axial deformations can propagate along the beam length. Therefore, the rotational constraint perpendicular to the beam's length (fork support) cannot block them. This means that by rotating one side of the beam, they form and transfer the sectional torsion across the rotational constraint and bring it to the other side. This behavior results in a reverse rotation of the output of the beam compared to the input. Here, this principle is used as a transmission and inversion between input and output. The schematic of the mechanism and the warping-induced displacements are shown in Fig. 4.1.

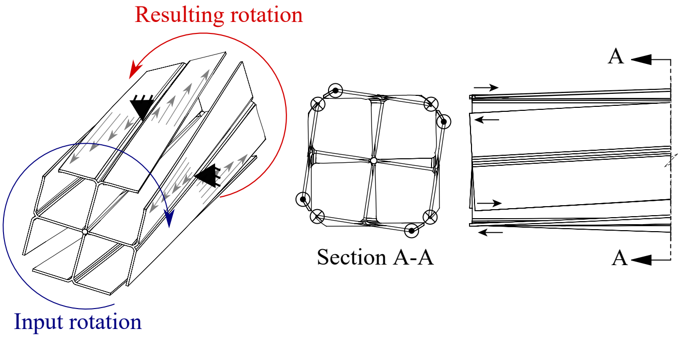

Figure 4.1: The working principle of the compliant CVT based on the warping of twisting beams. The axial displacements of the beam flanges, which are caused by the beam warping are also shown with vectors.

In an ideal case for a twisting beam with high warping constant, if there are no restrains for the warping, a uniform torsion along the beam will form upon a rotation at the input [24], as shown in Fig. 4.2. This uniform torsion results in a constant twist angle along the whole beam. At the same time, the presence of the prismatic mid-beam rotational constraint (the gray ring) leads to a zero twist angle for this middle cross-section. Therefore, assuming a constant twist angle along the beam, the ratio between output twist angle θ_{Out} (red ring) to input twist angle θ_{In} (blue ring) in an ideal case is equal to the ratio of the distance between mid constraint to input ring λ, over the distance of the mid constraint to the output ring $L-\lambda$ (Fig. 4.2):

$$\frac{\theta_{\text{Out}}}{\theta_{\text{In}}} = \frac{L-\lambda}{\lambda}. \tag{4.1}$$

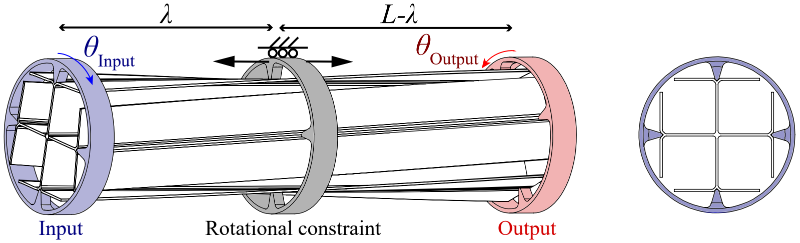

Figure 4.2: The input ring (blue), sliding rotational constraint ring (gray), and output ring (red) where rotations and constraints are exerted on the beams by prismatic grooves along the four web tips. The distance between the middle constraints and the beam's sides, which specifies the transmission ratio, are also shown.

It is explained that varying the mid constraint location directly affects the transmission ratio, exactly like the changes of mechanical advantage when the location of the middle joint of a lever changes. This analogy is illustrated schematically in Fig. 4.3. In this concept, the warping induced axial displacement of the cross-sections plays the role of the rigid bar in the lever mechanism. It is clear that if we reduce the rigidity of the bar in the lever mechanism, the output/input ratio will not be as ideally expected. A similar logic can explain by the effect of the warping constant on transferring the rotation.

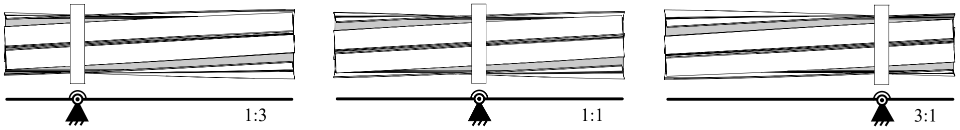

Figure 4.3: The comparison between the presented concept, when there is no load at output, and a lever mechanism

4.3 Methods

To realize this concept and to understand the effect of warping on the transmission behavior of the proposed mechanism, three open thin-walled cruciform beams are chosen, as shown in Fig. 4.4. These three beams have the same length (200 mm) and the same web dimensions. However, the flange widths of these three beams are selected to have three sizes as shown in Fig. 4.4(a). The beams are designed in a way to have torsional constants in the same order of magnitude and warping constants in three different orders of magnitude as shown in Table 4.1. The warping constant of a cross-section is a measure for the effort needed to reduce warping [24]. In other words, the effort needed to keep the cross-sections in plane although a torsion is applied. Similarly, the torsional constant of a section is a measure of the effort needed to make an angle of twist in the beam sections.

The warping induced transmission behavior of these beams are analyzed with an analytical solution, FEA with beam and shell elements, and with experiments. The details of each of these methods are described in the following sections.

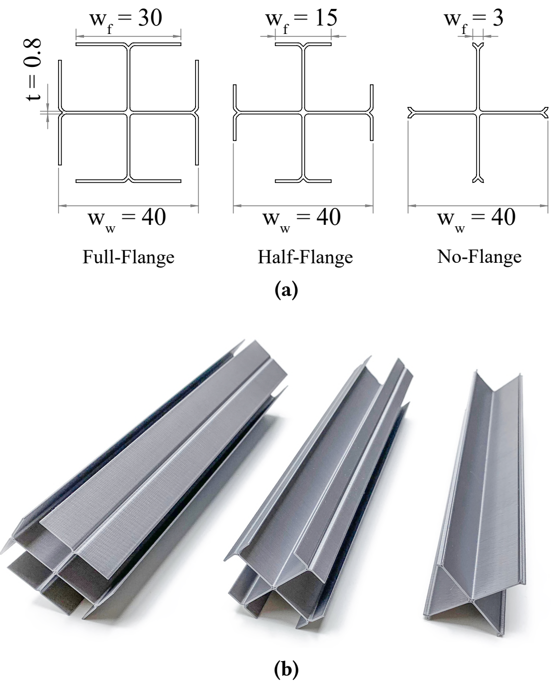

Figure 4.4: Three cruciform beams with the same length, same web dimensions, and different flange sizes are chosen to show the effect of warping. (a) shows the dimensions of these beams. (b) shows additive manufactured beams for the experiments.

Table 4.1: The St. Venant torsional constant J and warping constant I_w for three beams with full-flange (w_f = 30 mm), half-flange (w_f = 15 mm), and no-flange (w_f = 3 mm).

	Full-flange	Half-flange	No-flange
J [m^4]	3.48e-11	2.42e-11	1.59e-11
$I_\mathbf{w}$ [m^6]	2.76e-12	3.45e-13	3.14e-15

4.3.1 Analytical solution

Using Vlasov's torsion theory for beam elements with restrained warping [25], the rotation of a beam cross-section can be derived from this differential equation:

$$m = EI_\mathrm{w}\frac{\mathrm{d}^4\varphi}{\mathrm{d}x^4} - GJ\frac{\mathrm{d}^2\varphi}{\mathrm{d}x^2}, \tag{4.2}$$

where GJ is the torsional rigidity, EI_w is the warping rigidity and m is a distributed torsion moment along the beam. The torsion stiffness and warping stiffness are cross-section properties that are obtained using Ansys and shown in Table 4.1.

The torsion moment can be specified as:

$$M_t = \frac{\mathrm{d}B}{\mathrm{d}x} + GJ\frac{\mathrm{d}\varphi}{\mathrm{d}x}, \tag{4.3}$$

where the bimoment (B) shows the distributions of axial warping induced stress at a cross-section and follows this equation:

$$B = -EI_\mathrm{w}\frac{\mathrm{d}^2\varphi}{\mathrm{d}x^2}. \tag{4.4}$$

The boundary condition for the beam can be an applied rotation $\varphi = \varphi_0$, or an applied torsion moment $M = M_0$. In this case we imposed an input moment and solved Eq. 4.2 for each side of the beam. The differential equations were solved using a general form with four boundary conditions for each sides of the beam (eight in total for $x = 0 - C^-$, $x = C^+ - L$) as shown in Fig. 4.5. The input and output moments and angles can be tweaked separately in this formulation to see the behavior of the beam in different cases. The Matlab code based on this formulation that can solve Eq. 4.2 with different boundary conditions can be found in the supplementary material.

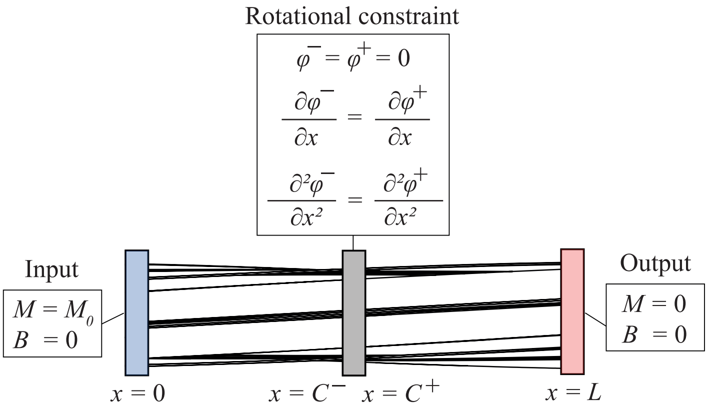

Figure 4.5: The boundary conditions of the beam which are used to solve Eq. 4.2

4.3.2 Finite Element Modeling (FEM)

The Ansys Parametric Design Language (APDL) has been used to analyze the output to input ratio of the beams. In order to have a fair comparison with the presented analytical formulation and the experiments, two different elements types are used: the beam element as a benchmark for analytical formulation and the more advanced shell element as a benchmark for the experiments.

The material properties of Polylactic Acid (PLA) [26] are used for both the models to match the material of the additive manufactured prototypes. The moments of $0.2\,\mathrm{N\,m}$ and $0.4\,\mathrm{N\,m}$ are exerted on the beam's input side via the ring. The position of the prismatic rotational constraint ring varies in nine steps from $-0.06\,\mathrm{m}$ to $0.06\,\mathrm{m}$ from the middle of the beam $x = 0\,\mathrm{m}$, to form 1:4 to 4:1 transmission ratios between output and input rotations.

Beam modeling

To have an estimation of the sectional rotations along the beam to compare with the results from analytical model, the beam element (beam 188) is used. This beam model is based on Timoshenko [27] with warping adapted from Schulz and Filippou [28].

Twenty elements were used to construct the beam. Based on the convergence check, this number of elements is slightly more than what is needed. Also, having 20 elements can give key points on the locations that are important for limiting the rotation for different transmission ratios, which is shown in this work. The beam's input constrained in three translational directions. For the middle ring, two translations, in y and z directions, and one rotation in x direction are implemented as shown in Fig. 4.6.

Shell modeling

The eight-node shell element (shell 281) is selected as the constructing element. The beam constrained at two positions, one at the input section similar to the beam, and four at the location of the prismatic rotational constraint at the tips of the webs, where points are tangentially constrained as shown in Fig. 4.6. It is important to note that the shear center of a bi-symmetric cruciform beam is in its center, and ideally the four webs will not warp, considering their small thickness. Therefore, the best location to constrain the rotation is the webs endpoint where there will be in principle no out of plane deformation of the cross-section due to the warping.

The input moment is applied via another set of four points on the input side, where tangential forces are applied. The input and output rotations upon exerted moments are obtained by tracking the rotation of the shear center of the input and output sections.

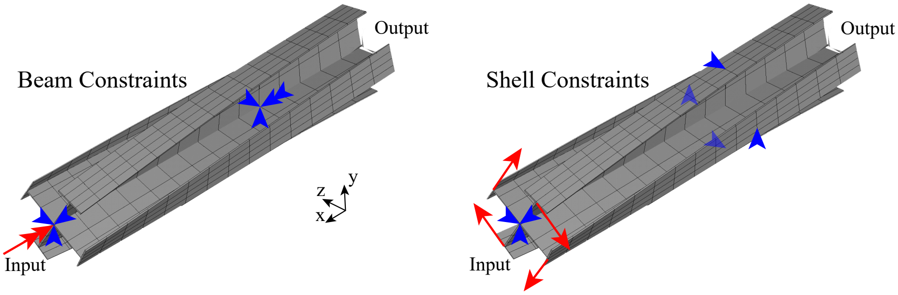

Figure 4.6: The model used for the finite element analysis and the rotational constraints imposed on it for both shell and beam elements. Blue arrows are showing constraints, and red arrows are showing input loads and moments.

4.3.3 Experimental setup

The compliant beams are used as rotation–rotation transmission. Therefore, to have control over the rotations of the sections and to replicate the same constraints described in the FEM, four longitudinal notches are made on the edge of the beam webs, and prismatic rigid rings with four V-shaped keys are designed to fit into these grooves as shown in Fig. 4.2 and realized in Fig. 4.7. Putting moments on these rings or constraining them has the same constraining effect described in the FEM for sets of four section-mate points (see Fig. 4.6).

The input ring is constrained in x, y and z directions and a force couple is exerted on it by two ropes connected to suspended weights via pulleys. The applied moment is kept constant as the ropes are wrapped around a central pulley. The moments are $0.2\,\mathrm{N\,m}$ and $0.4\,\mathrm{N\,m}$. The output ring is free in all directions. The middle constraint ring is connected to an yz compliant stage in order to have all freedom except rotation around the x axis. This compliant yz stage is connected to a slider parallel to the beam's longitudinal direction x, so that the middle ring can be moved along the beam. The prismatic motion of this ring can continuously vary the output/input ratio.

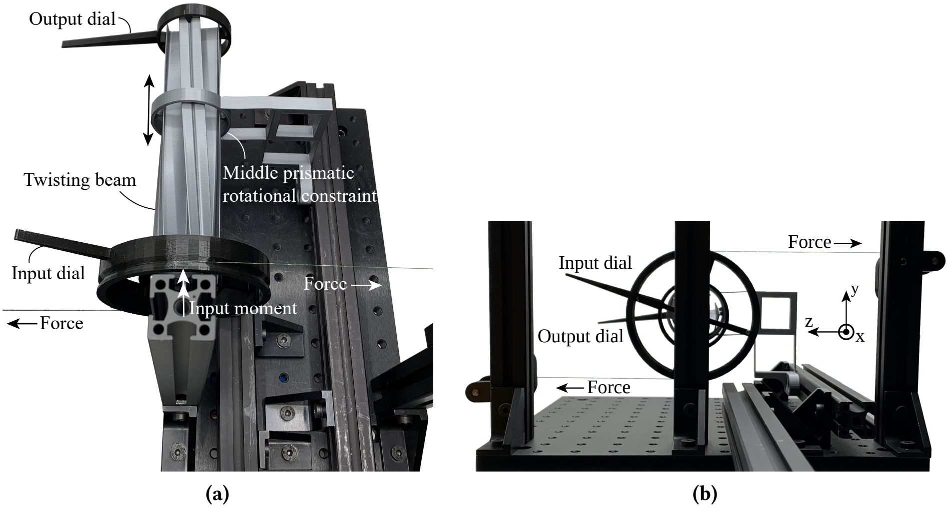

Figure 4.7: (a) shows the experimental setup. The beam is constrained in the middle where the compliant yz stage allows for translations while constraining the x rotation. The input ring is hinged to the ground and a force couple is exerted on it to make an input moment. Input and output rings have dials for image processing of their angles. (b) shows an example of the view which is used in image processing to measure the input and output rotations.

The behavior of the beams is examined by experiments on additive manufactured prototypes made out of PLA and shown in Fig. 4.4(b). The position of the middle constraint ring changes in the same nine steps as described in Section 4.3.2. The output and input rotation angles are measured by image processing of the output and input dials, which are connected to the rings. An example of an image from which angles are extracted from is shown in Fig. 4.7(b).

4.4 Results

To understand how warping induced displacements can transfer the rotation, the nodal rotations (φ) and the nodal warping ($\mathrm{d}\varphi/\mathrm{d}x$) along all three beams from the analytical solution and from FEM with a beam model are shown in Fig. 4.8. In this figure an input rotation of 0.5 rad is applied on one side of the beam and the rotational constraint located at the middle of the beam (x= 0.1 m) which is indicated by a vertical line.

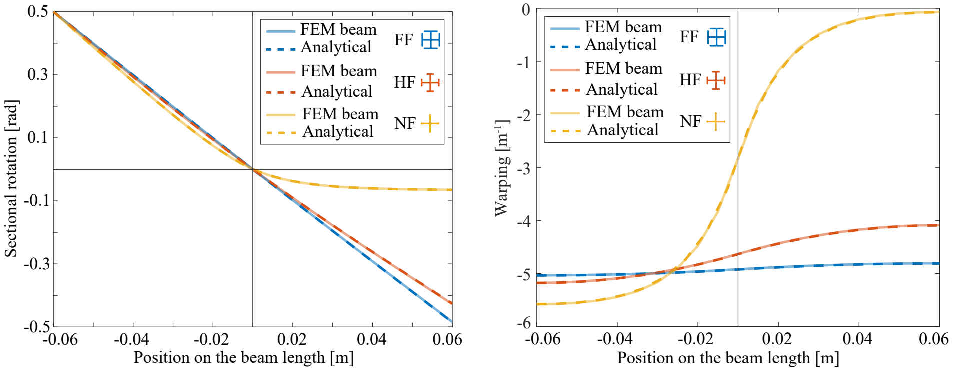

(a) **(b)**

Figure 4.8: (a) shows the sectional rotation (φ), and (b) shows the sectional warping ($\mathrm{d}\varphi/\mathrm{d}x$). Both parameters are illustrated for nodes along the three beams when an input rotation of 0.5 rad is applied at the input for a 1:1 ratio. The dashed lines are from the analytical solution and the solid lines are from the FEM with beam elements.

Beside the nodal solutions, the output/input rotation and moment are measured to evaluate how close these beam can perform to the ideal ratio from (Eq. 4.1). This ideal ratio is shown with a dotted line in Fig. 4.9 and the ratios which were achieved from beams are shown with colors. The data points are shown with circles and connected to each other with straight lines to show the trend. The resulting ratios are for the output/input rotation, in other words the geometrical advantage in Fig. 4.9. These results are obtained using the analytical model using an input moment of 0.2 N m.

The match rate to the ideal ratio is a good indicator of how good each of these beams can transfer the motion in different ratios of transmission. Therefore, this match rates with ideal ratio are shown in Fig. 4.10 for all modeling methods.

Another effective parameter that can have effect on the match rate with ideal ratio is the input rotation caused by the input moment. To evaluate this effect all beams undergo input moments ranging from 0.1 N m to 3 N m and the match rates in 1:1 ratio from FEM with shell elements are shown in Fig. 4.11.

It is mentioned that the experiments and FEM both are performed with 0.2 N m and 0.4 N m as input moments. To have a second insight on the effect of the input moment on the match rate besides the Fig. 4.11, the average match rates from all methods and for these two input moments are indicated in Table 4.2.

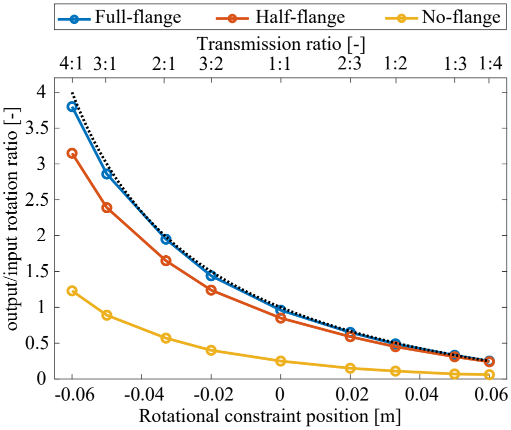

Figure 4.9: Resulting output/input angle ratios from analytical solution for the beams with nine different positions of the rotational constraint along the beam are compared with the ideal ratio of Eq. 4.1.

Table 4.2: The average match rate to ideal ratio for different cross-sections from analytical solution, FEM with beam and shell elements and experiments are shown for beams with the input moments of 0.2 N m and 0.4 N m.

	Full-flange		Half-flange		No-flange	
Input M [N.m]	0.2	0.4	0.2	0.4	0.2	0.4
Analytical [%]	97	97	86	86	16	14
FEM beam [%]	96	97	86	86	16	16
FEM shell [%]	93	91	79	75	17	16
Experiments [%]	68	67	56	55	10	9

Table 4.3: The resulting M_{out}/M_{in} ratios from analytical formulation when the output resistant moment increases from 0.5 to 5 N.m for the ideal geometrical ratios of 4/1, 1/1 and 1/4 of the full-flange beam.

	Output resistant moment M_{out} [N.m]									
	0.5	1	1.5	2	2.5	3	3.5	4	4.5	5
Ideal ratio	Resulting ratio M_{out}/M_{in} [-]									
4/1	1.77	2.47	2.84	3.07	3.22	3.34	3.42	3.49	3.55	3.59
1/1	0.57	0.73	0.81	0.85	0.88	0.90	0.92	0.93	0.94	0.95
1/4	0.11	0.16	0.18	0.20	0.21	0.22	0.22	0.23	0.23	0.23

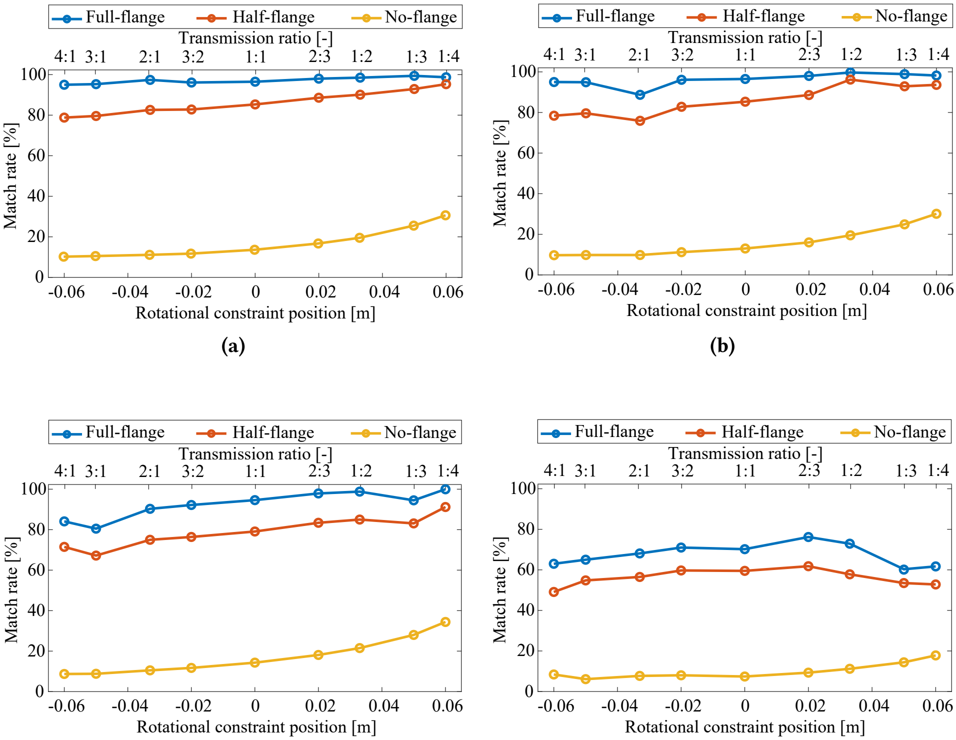

(a) (b) (c) (d)

Figure 4.10: The geometrical match rates with ideal ratio from Eq. 4.1 are shown for nine different transmission ratios. The results are obtained from (a) Analytical solution, (b) FEM with beam elements, (c) FEM with shell elements, and (d) Experiments.

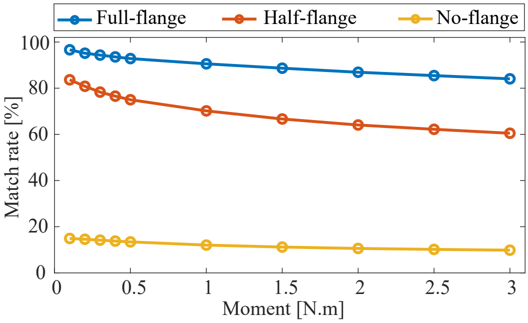

Figure 4.11: The effect of input moment on the geometrical match rate for three beams. The results are obtained from the FEM with shell elements with 1:1 ratio.

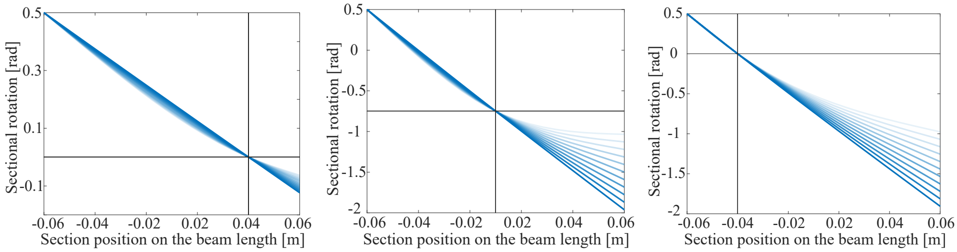

(a) **(b)** **(c)**

Figure 4.12: Effect of output resistant moment on the deviation of sectional twist angles along the beam from the expected uniform twist angle (straight line) when the resistant moment increases from 0 N.m (dark blue) to 5 N.m (light blue) for the full-flange beam for (a) 4/1 ratio, (b) 1/1 ratio, and (c) 1/4 ratio.

Lastly, in Table 4.3 an important feature of the transmission is shown, which is the ability to transfer moments while there is a resistant moment on the output. This table shows the resulting ratios between the output and input moments of the full-flange beam while the output resistance increases from 0.5 to 5 N.m. This is shown for geometric transmission ratios of 4:1, 1:1, and 1:4. Figure 4.12 illustrates the sectional rotations along the full-flange beam when the resistance increases from 0 to 5 N.m in ten steps for the same ratios that are mentioned in Table 4.3. It is clear that with higher resistance, the transferred rotation angles decrease, the lines start to deviate from being straight, and the geometrical match rates drop.

4.5 Discussion

It is shown that warping is a key feature in this transmission. Thus, beams with higher warping constants performed well, while beams with almost no warping could barely transfer any rotation or moment (see Fig. 4.8 and 4.9). Moreover, it is also shown that the transmission ratio and the input moment do not have a major effect on the mechanism's match rate and, therefore, on this transmission behavior (almost straight lines in Fig. 4.10 for all ratios).

The relation between warping constant and achievable match rate is investigated and shows the same trends from all methods. The role of the warping constant in transmission is clear. However, the exact relation between these two can be further investigated, as the full-flange and half-flange beams show close match rates despite the order of magnitude difference in their warping constant (see Fig. 4.10).

The average match rates from analytical solutions and FEM with the beam element are very close (see Fig. 4.10 a and b). This indicates that the proposed analytical formulation is reliable. The small deviation can be due to the different theories that are utilized in these two models. The results from the beam-based model are close to the results from the more advanced and accurate FEM with shell elements (see Fig. 4.10 b and c). The experiments show the same overall trend, with an average 17% lower match rate compared with

FEM with shell elements (see Fig. 4.10 c and d). This can be due to different mismatches: Firstly, it is not possible to have exactly the same point-constraints on the beam in reality as in the models. Instead, we used prismatic grooves, which are a simple solution but can cause mismatches between experiments and models. Furthermore, some parts of the experimental setup are not infinitely stiff, meaning that they might cause some deformation and, therefore, errors. Secondly, the prototypes were made by additive manufacturing, which causes anisotropy in the structure, this anisotropy was not modeled in FEM and cannot be considered in the beam formulation. Therefore, it can be a major source of discrepancy. Thirdly, the measurement using vision processing can have an error of up to 0.5 degrees, which can cause an error of up to 10% in some measurements with small angles. Fourthly, having small fillets in the connection points of webs and flanges for better bonding and printing results of the prototypes, are not included in any of the models, which can be another source of the mismatch. Fifthly, some assumptions in the models, i.e., no deformations in cross-section shape in the beam model and thin-walled assumptions in the shell model, are not fully true in this case, which means that the models are not completely capturing all the deformations. Using a solid element can capture all these effects and results in better results. However, it will significantly increase the computational cost.

Finally, using PLA as the material for the prototype and having large elastic deformations and large local strains can make material non-linearity a non-negligible factor, which was not considered in any of the used models. As for the use of other materials in a practical embodiment of the presented concept it can be noted that the elastic material parameters such as the Young's Modulus and the Shear Modulus, which relate the moments and the rotation in a linear fashion, have no influence on the kinematic behavior of the transmission. It means that any other linearly elastic material with similarly scaled elastic moduli will have the same input-output behaviors in the unloaded condition. As for the strength parameters such as the yield stress, it is evident that they directly affect the range of motion of the transmission. Therefore the material strength should be carefully considered in relation to the intended range of motion within the application.

Using a compliant mechanism in this design led to several advantages. However, there are also disadvantages to this type of mechanism. An inherent drawback of compliant mechanisms is that they require energy for deformation. Thus, the output to input energy efficiency of the mechanism becomes lower. It is possible to reduce this elastic strain energy since it is not lost but only temporarily stored in the form of elastic deformation; therefore, by the introduction of prestress, we can compensate for it and store the required energy in the mechanism so that we have a neutrally stable compliant element. This idea is currently being investigated by the authors to enhance the efficiency of the current compliant transmission.

It can be seen in Table 4.3 and Fig. 4.12 that for larger amounts of resistant moment, the output over input moment ratio matches closer with the ideal geometric ratio. However, by increasing the resistance, the deviation from a uniform twist angle along the structure increases, which means that the output/input match rate with the ideal geometric ratio drops.

This mechanism is presented mainly for applications where kinematics is the main focus. It is shown that it can transfer the moment as well as the rotation. However, having proportionally high moments at the output can change the warping behavior to semirestrained and lead to a different mode of deformation where the geometrical transmission may vanish. Nonetheless, it is still possible to analyze and characterize these highly restrained beams with the presented methods.

4.6 Conclusion

We have presented a design for a CVT using a compliant mechanism. It is shown that the warping induced displacement in the beams with a high warping constant can transfer the rotation from one side to the other, while continuously variable transmission ratios between the sides of the twisting beam can be achieved by the relocation of a prismatic rotational constraint along the beam.

The concept has been explained and investigated using analytical models, finite element analysis, and experiments. The results were compared with an ideal transmission to show the performance of the beams with different warping constants. All methods verified the hypothesized relation between the warping constant and transmission behavior.

More than 90% match rate with an ideal transmission was observed for a non-optimized design from the models. The match rate for the same beam is shown to be above 60% for the transmission ratio between 1:4 and 4:1 in the experiments. This shows the effectiveness and capability of this design. It is possible to further improve this match rate and thus the functionality of the transmission by optimizing the beam parameters.

This concept can be used instead of traditional CVTs in applications where it is essential for the design to be lightweight (e.g., flapping micro-robots, bio-mimetic walking robots), monolithic (e.g., submerged systems), free of backlash (e.g., precision systems and measurement devices), and easy to make on a small scale (e.g., MEMS, metamaterials). However, for applications where a continuous rotation is needed and/or a large amount of power should be transmitted with minimum loss of energy, the state-of-the-art belt and chain CVTs that are introduced in section 4.1 can perhaps perform better.

References

[1] G. Carbone, L. Mangialardi, and G. Mantriota, “A comparison of the performances of full and half toroidal traction drives,” *Mechanism and machine theory*, vol. 39, no. 9, pp. 921–942, 2004.

[2] K. Atallah, J. Wang, S. D. Calverley, and S. Duggan, “Design and operation of a magnetic continuously variable transmission,” *IEEE Transactions on Industry Applications*, vol. 48, no. 4, pp. 1288–1295, 2012.

[3] N. Srivastava and I. Haque, “A review on belt and chain continuously variable transmissions (cvt): Dynamics and control,” *Mechanism and machine theory*, vol. 44, no. 1, pp. 19–41, 2009.

[4] L. L. Howell, S. P. Magleby, and B. M. Olsen, *Handbook of Compliant Mechanisms*. Somerset: Wiley, 1 ed., 2013.

[5] C. Zhang and C. Rossi, “A review of compliant transmission mechanisms for bio-inspired flapping-wing micro air vehicles,” *Bioinspiration & biomimetics*, vol. 12, no. 2, p. 025005, 2017.

[6] S. L. Weeke, N. Tolou, G. Semon, and J. L. Herder, “A fully compliant force balanced oscillator,” in *International Design Engineering Technical Conferences and Computers and Information in Engineering Conference*, vol. 50152, p. V05AT07A008, American Society of Mechanical Engineers, 2016.

[7] S. H. Collins, M. Wisse, and A. Ruina, “A three-dimensional passive-dynamic walking robot with two legs and knees,” *The International Journal of Robotics Research*, vol. 20, no. 7, pp. 607–615, 2001.

[8] S. Seok, A. Wang, M. Y. Chuah, D. Otten, J. Lang, and S. Kim, “Design principles for highly efficient quadrupeds and implementation on the mit cheetah robot,” in *2013 IEEE International Conference on Robotics and Automation*, pp. 3307–3312, IEEE, 2013.

[9] R. Mak, A. Amoozandeh Nobaveh, G. Radaelli, and J. L. Herder, “A curved compliant differential mechanism with neutral stability,” in *International Design Engineering Technical Conferences and Computers and Information in Engineering Conference*, American Society of Mechanical Engineers, 2022.

[10] J. B. Hopkins and R. M. Panas, “Design of flexure-based precision transmission mechanisms using screw theory,” *Precision Engineering*, vol. 37, no. 2, pp. 299–307, 2013.

[11] D. F. Machekposhti, N. Tolou, and J. Herder, “A statically balanced fully compliant power transmission mechanism between parallel rotational axes,” *Mechanism and Machine Theory*, vol. 119, pp. 51–60, 2018.

[12] C. B. Pedersen and A. A. Seshia, “On the optimization of compliant force amplifier mechanisms for surface micromachined resonant accelerometers,” *Journal of Micromechanics and Microengineering*, vol. 14, no. 10, p. 1281, 2004.

[13] T. Okada and K. Tahara, “Development of a two-link planar manipulator with continuously variable transmission mechanism,” in *2014 IEEE/ASME International Conference on Advanced Intelligent Mechatronics*, pp. 617–622, IEEE, 2014.

[14] L. L. Chu, J. A. Hetrick, and Y. B. Gianchandani, “High amplification compliant microtransmissions for rectilinear electrothermal actuators,” *Sensors and Actuators A: Physical*, vol. 97, pp. 776–783, 2002.

[15] N. D. Mankame and G. K. Ananthasuresh, “A Compliant Transmission Mechanism With Intermittent Contacts for Cycle-Doubling,” *Journal of Mechanical Design*, vol. 129, pp. 114–121, 09 2006.

[16] X. Lachenal, S. Daynes, and P. M. Weaver, “A non-linear stiffness composite twisting i-beam,” *Journal of intelligent material systems and structures*, vol. 25, no. 6, pp. 744–754, 2014.

[17] G. Radaelli, "Reverse-twisting of helicoidal shells to obtain neutrally stable linkage mechanisms," *International Journal of Mechanical Sciences*, vol. 202, p. 106532, 2021.

[18] D. Farhadi Machekposhti, N. Tolou, and J. Herder, "A review on compliant joints and rigid-body constant velocity universal joints toward the design of compliant homokinetic couplings," *Journal of Mechanical Design*, vol. 137, no. 3, p. 032301, 2015.

[19] R. Vos, Z. Gürdal, and M. Abdalla, "Mechanism for warp-controlled twist of a morphing wing," *Journal of Aircraft*, vol. 47, no. 2, pp. 450–457, 2010.

[20] M. J. Bianco, A. K. Habtemariam, C. Könke, and V. Zabel, "Analysis of warping and distortion transmission in mixed shell–gbt (generalized beam theory) models," *International Journal of Advanced Structural Engineering*, vol. 11, no. 1, pp. 109–126, 2019.

[21] S. Shayan and K. Rasmussen, "A model for warping transmission through joints of steel frames," *Thin-Walled Structures*, vol. 82, pp. 1–12, 2014.

[22] C. Basaglia, D. Camotim, and N. Silvestre, "Torsion warping transmission at thin-walled frame joints: Kinematics, modelling and structural response," *Journal of Constructional Steel Research*, vol. 69, no. 1, pp. 39–53, 2012.

[23] M. Valentijn, "Thin-walled warping beams for differential mechanism applications," 2020.

[24] P. Hoogenboom and A. Borgart, "Method for including restrained warping in traditional frame analyses," *Heron 50 (1)*, 2005.

[25] V. Vlasov, "Thin-walled elastic beams, english translation," *Published for NSF and Dept. of Commerce, USA by Israel Program for Scientific Translation, Tel Aviv*, 1961.

[26] A. Qattawi, B. Alrawi, A. Guzman, *et al.*, "Experimental optimization of fused deposition modelling processing parameters: a design-for-manufacturing approach," *Procedia Manufacturing*, vol. 10, pp. 791–803, 2017.

[27] S. Timoshenko, *Theory of elastic stability 2e.* Tata McGraw-Hill Education, 1970.

[28] M. Schulz and F. C. Filippou, "Generalized warping torsion formulation," *Journal of engineering mechanics*, vol. 124, no. 3, pp. 339–347, 1998.

5

Compliant variable stiffness twisting elements

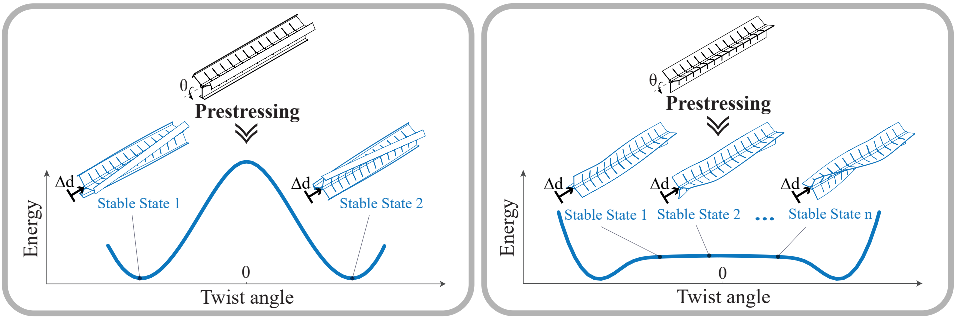

The previous chapter shows one of the functionalities of warping in twisting beams namely transmission. However, the presented compliant beam always has stiffness in its range of rotation and stores a portion of input energy as elastic deformation. This issue pertains not only to the presented compliant transmission but also to compliant mechanisms in general. Hence, controlling or eliminating the inherent positive stiffness of compliant elements is a key requirement for a variety of applications. This chapter presents two concepts to resolve the positive stiffness issue of the twisting beams that are the subject of research in part II of this thesis. In the first concept, the beam shows a range of variable torsional stiffness, from positive to zero and negative. In the second concept, the beam shows a switching behavior from positive to zero torsional stiffness. The working principle of both concepts is based on the shortening of the center-axis line of the multi-symmetric open thin-walled beams.

This chapter was submitted as:
Amoozandeh Nobaveh, A., Herder, J.L. and Radaelli, G., 2023. Compliant variable negative to zero to positive stiffness twisting elements.

Compliant variable negative to zero to positive stiffness twisting elements

Abstract *Compliant mechanisms have the potential to be utilized in numerous applications where the use of conventional mechanisms is unfeasible. These mechanisms have inherent stiffness in their range of motion as they gain their mobility from elastic deformations of elements. In most systems, however, complete control over the elasticity is desired. Therefore, compliant mechanisms with variable, including zero, stiffness can have a great advantage. We present a novel concept based on the prestressing of open thin-walled multi-symmetric beams. It is demonstrated that by changing the prestress on the center-axis of these beams, a range of variable torsional stiffness can be achieved. For beams with a large warping constant, the stiffness changes from positive to zero and negative as the prestress increases, while for beams with a near-zero warping constant, the range of neutrally stable twisting motion increases. A planar equivalent is shown in this work to elucidate the notion, and numerical and experimental analyses are performed to validate the prestress-related behavior.*

5.1 Introduction

Compliant Mechanisms (CM) have been developed by researchers to make more efficient mechanical devices that can work in specific conditions such as vacuum or high temperature [1]. These mechanisms can integrate several functionalities into one system, leading to lighter and more space-efficient designs. Moreover, due to their monolithic design, these mechanisms are potentially suited for applications where minimized friction, backlash, and particle generation are important, as well as for applications where, due to the small sizes, assembly is not viable. CMs are widely being applied to precision devices and even some daily-used products. Aside from that, there are ongoing investigations into how to transfer the principles of compliant mechanism design to other research fields, such as soft robotics [2, 3], wearable robotics [4–6] Micro Electronic Mechanical Systems (MEMS) [7], morphing structures [8–10], origami [11], and metamaterials [12]. There are several studies on the design of compliant units that are useful for incorporation into modular architectures. Examples include linear motion guides [13], constant force generators [14] and prescribed kinetostatic behavior generators [15–17], bistable units [18, 19], twisting elements or revolute joints [20, 21].

CMs derive their mobility from the elastic deformation of their elements, which means that normally they have an inherent positive stiffness in their range of motion. Therefore, to actuate a CM, a certain amount of energy should be added to the system, which is stored in the material in the form of elastic strain energy. Once the compliant mechanism is not actuated, this energy will be released to bring the mechanism back to its natural, undeformed configuration. This integration of motion and energy storage into one element is beneficial for several applications. However, in some applications, providing this energy to move the mechanism in its intended range of motion is not desirable because the system requires more power for each cycle and the overall efficiency decreases. This means that in these applications a range of constant potential energy, or in other words, a range of neutral stability would be convenient. There are several ways to achieve a range of elastic neutral stability, e.g., utilizing anisotropic materials [22–24], prestressing the structure either by imposing a constraint [25], or by plastic deformation [26–28], or by introduction of a movable deformed region [29, 30].

In some applications of CM, one or more element(s) have specific functionality, and it is not feasible to remove them and their inherent positive stiffness. In these cases, it is not possible to change the whole design to make the mechanism neutrally stable with one of the above-mentioned methods. Therefore, to achieve neutral stability in these cases, a common way is to compensate the inherent positive stiffness of the system with the exact same negative stiffness from another system to achieve a range of zero stiffness. Using the negative stiffness to compensate for positive stiffness is widely researched in the literature [31, 32], both for linear negative stiffness [33] and nonlinear negative stiffness compensators [34]. In addition, there are numerous applications in the literature that require variable stiffness on demand, which means the part with negative stiffness should be able to change its amount so that the overall stiffness of the system becomes tunable [35]. These applications are ranging from aerospace engineering [36–38], to medical devices [39, 40], wearable devices [41–43], and vibration control [44]. In all these applications, the shared desired characteristic of having variable stiffness allows them to alter the overall system behavior in a specified direction on demand.

However, looking at these variable stiffness concepts, they are mainly developed for translation motion. To the best of authors' knowledge, there is no rotational variable stiffness concept that covers variable stiffness from negative to positive, including zero. There are only a handful of concepts that have the potential to provide that. Bilancia et al. [45] demonstrated a zero torque compliant rotational joint that uses prebuckled beams to achieve negative stiffness to compensate for the mechanism's positive stiffness. Li et al. [46] presented a torsional negative stiffness mechanism utilizing several thin strips. Schultz [47] presented an airfoil-like bistable twisting element that was made from two precurved shells connected to each other. Seffen and Guest [48] further researched similar effects, and later, Lachenal et al. [49] presented a bistable twisting I-beam where the precurved flanges assembled on the beam's web to provide a negative stiffness twisting behavior.

In this work, we are introducing two concepts for twisting compliant elements. The first concept can provide variable torsional stiffness from negative to zero to positive. The second concept can provide on-off switchable torsional stiffness, which changes the element's inherent positive stiffness to zero stiffness. Both concepts works based on the fact that as the center axis of a multi-symmetric thin-walled beam shortens, the outer parts of the beam's section go under compression. As compression is the stiffest mode of deformation and requires high elastic energy, the outer parts start to deform in other forms instead, in order to facilitate the web shortening with a lower overall elastic energy. In one concept where the beam has flanges and a high warping constant, after the shortening, the beam twists to facilitate the shortening with lower amount of energy. This twist can happen in both directions and therefore, it is bistable. By changing the amount of shortening, the mechanism's stiffness varies from its inherent positive to zero and more negative stiffness. In the other concept, the flanges of the beam are removed. Therefore, the outer parts of the webs start to buckle under the compression due to the center axis shortening. This locally buckled part of the webs can move along the structure upon twisting the beam without requiring extra energy, and provides a range of neutral stability. Therefore, the mechanism's stiffness switches from the inherent positive to zero upon buckling due to the axial shortening. In this case, by increasing the preload, the range of of motion with zero torsional stiffness increases. These two designs and their effective parameters are explored and modeled with FEM and experiments. Moreover, a simplified planar equivalent is presented that helps with understanding the principles behind the concepts.

The chapter is structured as follows: In Section 5.2, an overview of the concept and its principle of working is introduced. Also, a planar equivalent model is introduced for a better understanding of the beams' behavior. The definition of effective parameters, together with the finite element solver and the context of experimental verification procedures, are elaborated in Section 5.3. In Section 5.4 the resulting behavior from the two designs with different preloads are shown. A discussion on the results and possible improvements are given in Section 5.5, and the conclusion beside possible applications of these concepts are given in Section 5.6.

5.2 Concept overview

The geometry of the concepts is shown in Fig. 5.1. Both concepts are long, thin-walled extruded beams with transverse slits running the length of their multi-symmetric webs. These slits allow for shortening of the center axis, implying longitudinal preload. The First concept Fig. 5.1(a), also has flanges to enable warping along the structure and the second concept Fig. 5.1(b) is only made form the multi-symmetric webs. A center hole is made in both concepts, which makes room for an element, i.e., wire, for preloading and shortening of the beams.

The working principle of both beams to achieve neutral and negative stiffness under prestress can be clarified by understanding their total energy states in their twisting range of motion. This energy is depicted in Fig. 5.1(a) for the beam with flanges. Two minima can be seen in the range of motion. There is also a peak in between these two minima or stable states. This peak indicates that the beam is not stable between these two and hence exhibits a negative stiffness. Figure 5.1(b), also shows two minima for the beam without flanges; however, it has a flat energy state in between these two minima. This flat section indicates that for a relatively large range between its stable states, the beam exhibits neutrally stable twisting motion, i.e., zero torsional stiffness.

Different techniques could be used to contract the web(s) and prestress the mechanism with a displacement to achieve these behaviors. Here, we employed transverse slits along the web(s) such that a longitudinal displacement along the axis of the beam's center could make the beam shorter with less reaction force. These slits and the displacement Δd that causes the longitudinal prestress are shown in Fig. 5.1.

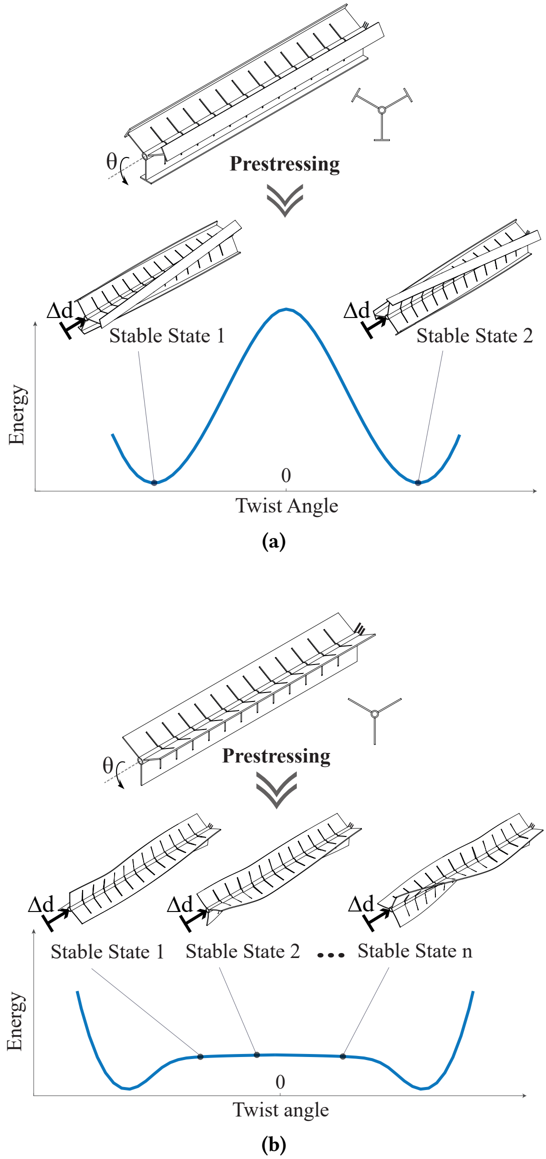

Figure 5.1: The geometry of the multi-symmetric beams and their transverse slits. The prestressed beams exhibit two stable twisted forms. (a) The beam with flange (high warping constant) possesses an energy peak between the two minima and, therefore, bistable behavior. (b) The beam without flange (near-zero warping constant) exhibits a flat energy state and, therefore, neutrally stable behavior between the two minima.

We also propose another way of understanding the principle of the presented design using a simplified planar equivalent, Fig. 5.2. To make this planar representation of the beams, we used a set of parallelograms, where the deviation in edge angles of each parallelogram from 90° represents the twist in each section of the beam. Therefore, in this model, when the beam is unstressed, all parallelograms are straight. To represent different stiffnesses of the beam sections in the planar equivalent, two torsion springs were added to each parallelogram. One is between two perpendicular links of each parallelogram (red springs), which keeps the parallelogram in its initial rectangular shape. These springs represent the torsional rigidity of the beam's sections. By increasing this rigidity, it is harder to twist the beam, which, in its planar equivalent, means that it is harder to make each parallelogram deviate from their initial rectangular shape. The second spring is positioned between the vertical links of two adjacent parallelograms (green springs). These springs maintain the angles of adjacent parallelograms and reflect the ability to transfer twist to the following section of the beam. By increasing this rigidity, it becomes more difficult to make a quick change in the twist angle from one element to its neighbors. In planar equivalent, it becomes more difficult to make each parallelogram diverge from the angle of its neighbors. This spring stiffness can be related to the beam section's warping constant. In prior research, we have shown that the warping of an evenly extruded beam is the primary cause of twist transfer along its length [50]. In Fig. 5.2(a, b), the torsional rigidity of both beams is on the same order of magnitude; hence, the red springs are depicted as being sized comparably. However, the beam with flange has a warping constant that is an order of magnitude more than the beam without flange. Therefore, the green springs on beam (a) are considerably more rigid, depicted as being thicker.

Under a vertical displacement Δd, the energy stored in the planar equivalent is the sum of all the energies stored in springs:

$$U_{\text{total}} = \frac{1}{2}\sum_{i=1}^{n}(k_{\text{red}_i}\Delta\theta_i^2 + k_{\text{green}_i}\Delta\varphi_i^2). \tag{5.1}$$

In the beam with flanges, the stiffness of the green springs is significantly greater than that of the red springs; consequently, the majority of deformation occurs in the red springs when the structure is prestressed to reduce the overall energy. This will result in the uniform bending to the right or left, i.e., equivalent to a uniform CW or CCW twist angle for the beam. Now, if we attempt to shift the upper section of the structure horizontally, i.e., similar to twisting the free side of the beam, it will snap into the stable position on the other side, i.e., equivalent to torsional bistability.

In a similar manner, the beam without flanges initially displays a uniform bend to one side; but, upon horizontal displacement of the top portion to the opposite side, one of the parallelograms snaps to its inverted stable condition, since it is much less dependent on the angle of its neighboring parallelograms. As this horizontal displacement of the top portion continues, the number of inverted parallelograms increases and the point where the tilt angle inverses descends from the top to the bottom. Based on Eq. 5.1, the transition between these states requires no additional energy. Therefore, horizontally shifting the top portion of the structure (similar to twisting the beam between its stable states) goes without change in energy and is therefore neutrally stable. In the actual beam without a flange, the bent portion of the webs can move along the structure without consuming energy and provides a range of zero torsional stiffness.

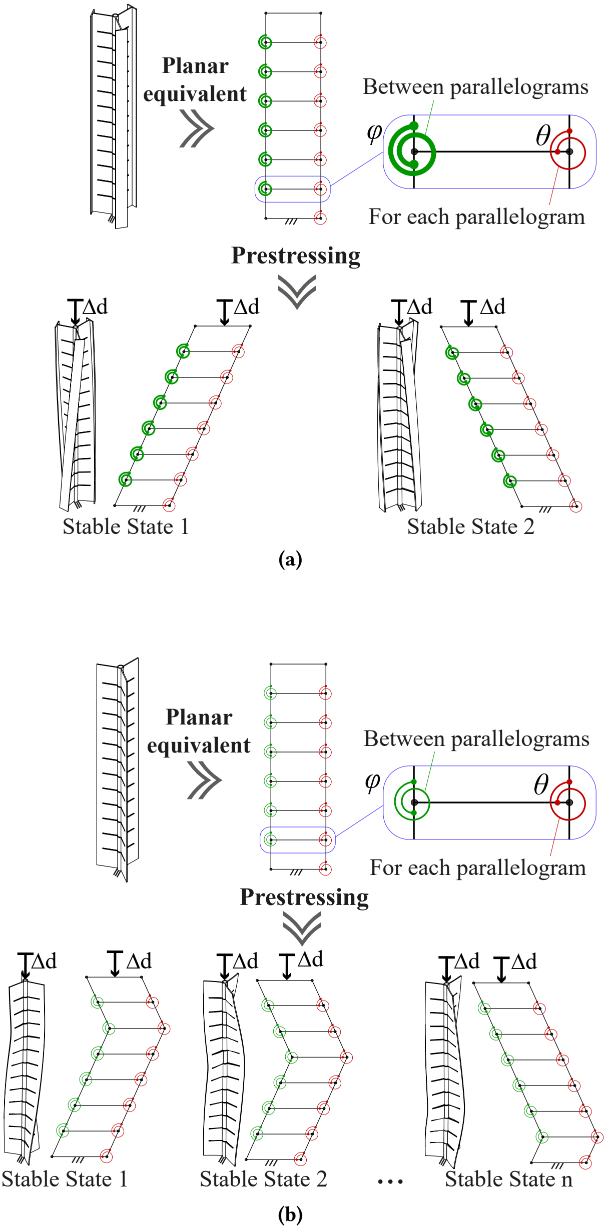

Figure 5.2: The planar equivalent of the beams with the red springs representing the torsional constant, and the green springs representing the warping constant. (a) The beam with flanges has a high warping constant and, as a result, exhibits uniform twist. (b) The beam without flanges has a near-zero warping constant which alows for transition of bent location along its length, and maintains a constant total energy based on Eq. 5.1.

5.3 Methods

In the following subsections, the effective design parameters of the concept are elaborated. A Finite Element Model (FEM) to analyze the beams' behavior in different preloading conditions is presented, followed by an explanation of the experimental setup for verifying the results.

5.3.1 Design parameters

The current design's main principle is based on shortening the center axis of a thin-walled multi-symmetric beam to achieve neutral- or bi- stability. It will be shown that the amount of shortening improves the captured behavior. Therefore, this parameter is subject to investigation. However, the design of the web and its dimensions are remaining fixed throughout all results. Therefore, here we discuss the reasoning behind the selection of this shape and its design parameters.

There are several ways to decrease the compression stiffness of the center axis of the beam in order to achieve local shortening by implying less stress to the structure, i.e., using non-homogeneous material where the middle part is softer than outer part, or thickening the webs towards the outside, or making several slits in the center part of the sections throughout the beam, which is the solution that is used in this work. These slits help the structure to significantly reduce the longitudinal stiffness along the center axis with respect to the outer parts to allow for shortening. The size and number of these slits (n) are selected based on preliminary investigation and they are kept the same for all the simulations and prototypes. The effect of using insufficient number of slits is later explained in section 5.5. Other design parameters are all indicated in Fig. 5.3. These parameters are arbitrarily selected and can be tuned for different applications and from preliminary investigation they appear to have only a minor contribution to the overall concept. The web width (w_w) is 20 mm, the flange width (w_f) is 15 mm for the beam with flange, the axial hole diameter (d) is 3.5 mm, the thickness (t) is 0.9 mm all over the beams, the length of the beam (L) is 200 mm, the slit width (w_s) is 15 mm, the slit thickness (t_s) is 0.5 mm and the length of each section (L_s) is 10 mm, with (n = 19) slits along the beams.

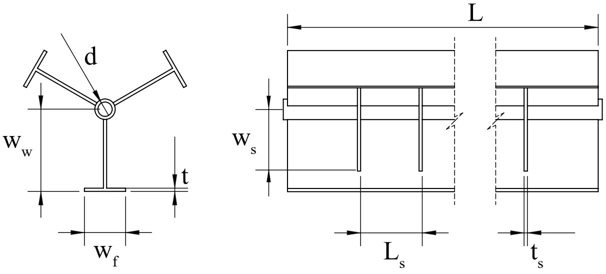

Figure 5.3: The design parameters of the beams.

The geometry, loading, and constraints are all axisymmetric; therefore, it is possible to reduce the model to only a one-web structure with axisymmetric constraints, as shown in Fig. 5.4. This reduces the computational cost, and to match reality, everything will be multiplied by the number of webs (m). It is important to mention that for spatial stability in a physical prototype, the number of webs in one beam should not be less than three (m ≥ 3), so that all forces caused by the shortening and bending of each web can be supported by the two other webs and the structure remains stable. This means that not only three, but any number of multi-symmetric webs larger than three will work for this structure, as shown in Fig. 5.4.

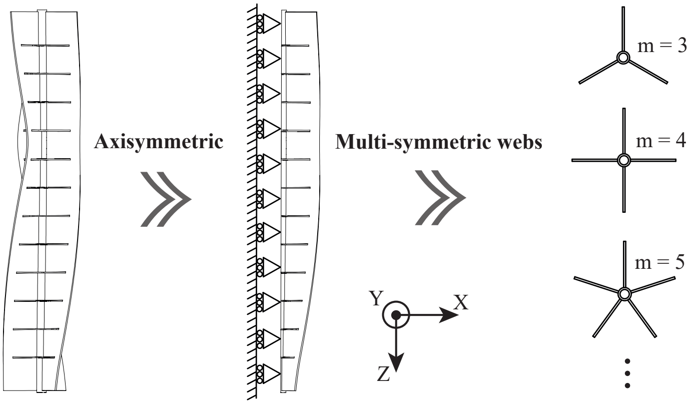

Figure 5.4: The axisymmetric constraint simplifies the multi-symmetric beam to a single web. The number of webs (m) on beams must be at least three for spatial stability.

5.3.2 FEM

For both set of simulations, only one web from each beam is modeled with axisymmetry constraints similar to Fig. 5.4 as discussed in Subsection 5.3.1. The beams' web is constrained in all translations at the axis-point of the grounded side as shown in Fig. 5.5 and constrained in X and Y translational directions at the axis-point of the prestressed (actuated) side. To constraint the rotation on the grounded side of the beam a Y translational constraint applied to the middle point of the web. In addition, a Z rotation match between the axis-point of the actuated side and the middle point of the actuated side was added.

The simulation includes two steps. First, a longitudinal displacement (Δd) is applied to the axis-point of actuated side of the beams; simultaneously, a rotation (RotZ) is applied to assist its transitioning to a twisted state. The twist angle at the end of the preloading step was registered as θ. In the second step, a twist angle in the other direction with twice the size of the initial registered angle, i.e., -2θ, was applied to the beam and the reaction moment in the axis-point of actuated side is registered to form the moment – angle graphs of the beams.

For the simulations, the eight-node shell element, shell 281, from ANSYS Parametric Design Language (APDL) is selected as the constructing element. The material properties are set to be similar to the prototypes material, Nylon (PA12), with Young's modulus of 1.7 GPa and Poisson's ratio of 0.38. A nonlinear solver was used, with minimum 40 steps for preloading depending on the (Δd) and minimum 50 steps for capturing the moment – angle behavior depending on the range of rotation.

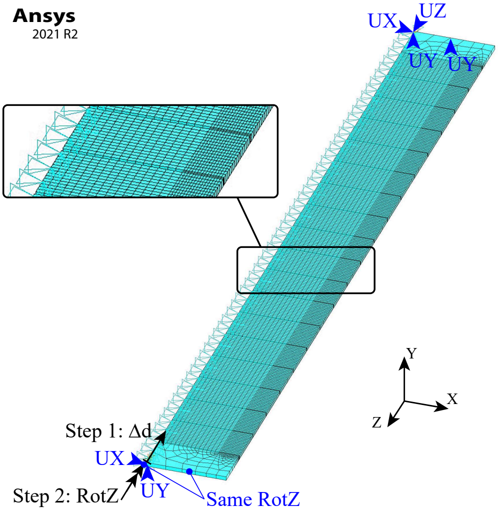

Figure 5.5: The constraints on the fixed and actuated sides of the web are shown. An axisymmetric constraint is applied similar to what is shown in Fig 5.4 along the web.

5.3.3 Experimental setup

Two sets of beam with and without flanges are fabricated using multi-jet fusion additive manufacturing method with Nylon (PA12) as the material, as shown in Fig. 5.6.

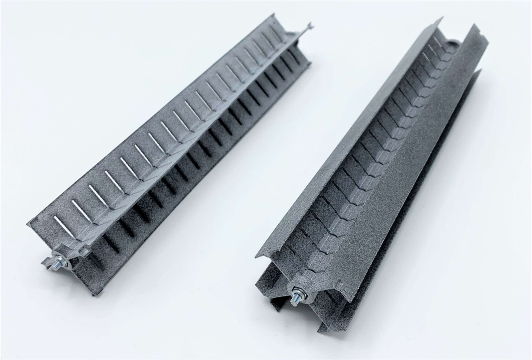

Figure 5.6: The prototypes were made from nylon (PA12) using multi-jet fusion 3D printing and prestressed using threaded rods.

The beams are initially prestressed by providing displacement using a threaded rod within the beams' center axis. This displacements range from 0 to 4 mm in 1 mm increments for beams without flange and 0 to 2.8 mm in 0.7 mm increments for beams with flange. With each degree of prestress, the moment – angle of the beams was measured using a universal test machine, Zwick Z005, with a separate torque meter module, HBM T20WN as shown in Fig. 5.7.

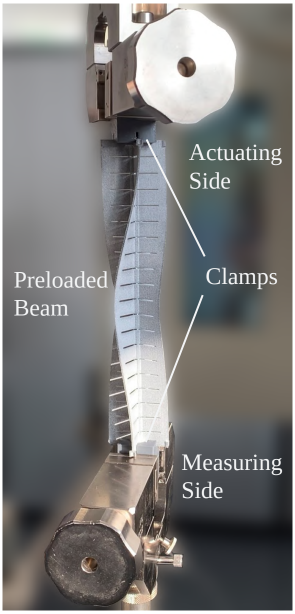

Figure 5.7: The measurement setup shows the actuating and reaction moment measuring sides of the preloaded beam that is clamped to the machine.

Similar to the constraints that are implied in the FEM, each of the prestressed beams is clamped on one side to the measuring point of the machine, and on the other side, a rotation is progressively applied to the actuated side of the webs.

5.4 Results

Figure 5.8 shows the moment – angle graphs of both with and without flange beams. They share the same web dimensions (see Fig. 5.3) and the same number of slits (n = 19). The longitudinal preloading in their center axis increases in four steps, as discussed in section 5.3. Figure 5.8(a,c) are for the beam without flanges from numerical model and experiments respectively. It can be clearly seen that the beam has its inherent positive stiffness when no prestress is applied, and upon applying prestress, an increasing range of zero moments and neutrally stable behavior are achieved. Figure 5.8(b, d) show the numerical model and experiment results for the beam with flanges. These results show that this beam also shows its linear inherent stiffness without preload, and upon 0.7 mm preload it shows a short range of near-zero stiffness. Finally, a clear bistable behavior, negative torsional stiffness, can be seen upon 1.4 to 2.8 mm of preload.
It is important to note that the beams that are used in experiments have four webs; therefore, to make the results comparable with the single web with axisymmetric constraint from FEM, the resulting moments from experiments are divided by four, and all the results are for a single web (beam without flange) or a single web and flange (beam with flange).

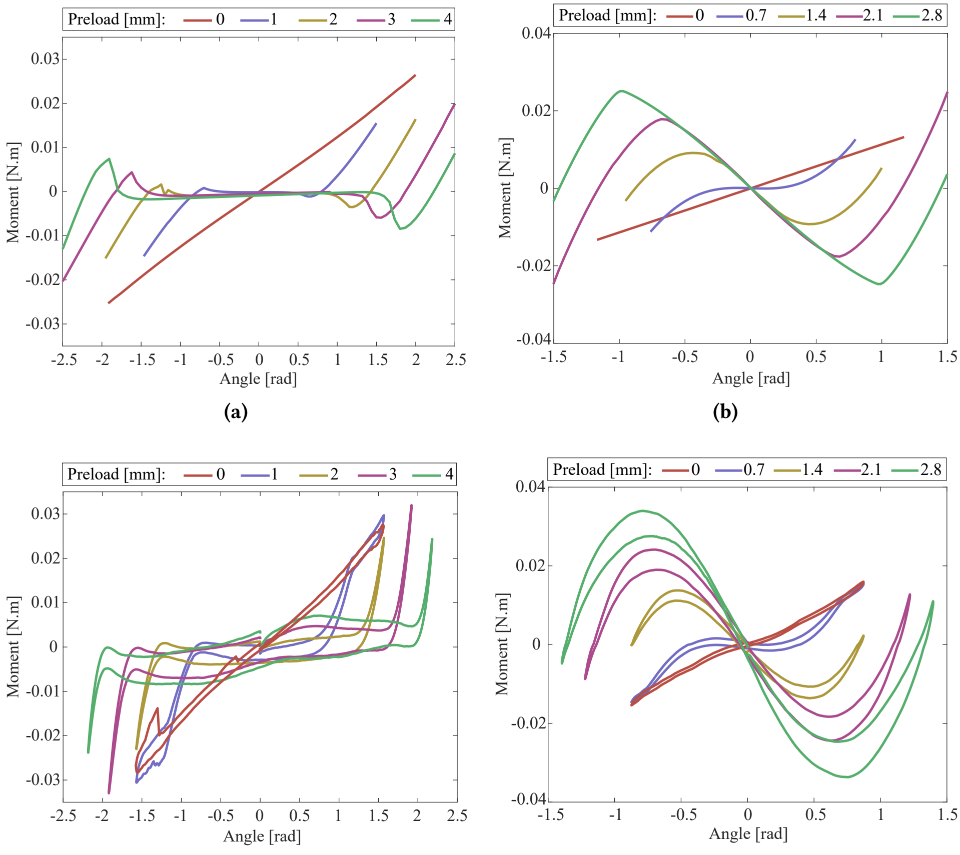

(a) (b)

(c) (d)

Figure 5.8: The moment – angle graphs of the beams upon different preloadings. (a) and (c) show the numerical and experimental results for the beam without flange under axial preloads of 0 to 4 mm. (b) and (d) show the numerical and experimental results for the beam with a flange under axial preloads of 0 to 2.8 mm.

5.5 Discussion

It is demonstrated that the prestressing of the center axis of an open, thin-walled, multi-symmetric beam can have significant influence on its torsional stiffness. Both the with- and without-flange beams exhibit two local minima at the ends of their range of motion following prestressing. The beam with flanges displays an energy peak between these two minima, indicating bistable behavior. The beam without flange exhibits a flat energy between the two minima, indicating a neutrally stable behavior. In addition, it is demonstrated that both bistable behavior and neutral-stability range can be enhanced by increasing the beams' prestress. Consequently, the presented concept can provide a twisting element with variable stiffness that can achieve negative, zero, and positive torsional stiffness for beams with high warping constant, and a positive and tunable range of zero torsional stiffness for beams with near-zero warping constant.

A rather large range of zero torsional stiffness motion for the compliant beam without flange and a high bistable energy storage in beam with flange were obtained by the parameters that are used in this work to demonstrate the functionality of the concept. These behaviors can be further enhanced to maximize design functionality based on specific requirements of certain applications of these concepts.

The investigations in this chapter show a clear trend between the amount of prestress and the resulting behaviors of the beams, i.e., peak moment in bistability and range of neutral stability. The exact relation between prestress and the achieved behavior can be further investigated in future research.

Some design parameters, such as the number of slits, have effects on the overall functionality of the presented concept and should be carefully selected. In Fig. 5.9 we have shown that increasing this number will cause a smoother behavior for the twisting element, and avoid multi-stability due to the snapping of bistable units (parallelograms) along the beams. However, after selecting a sufficient amount of slits, this effect vanishes and no further investigation is required for it, therefore, it is also excluded from the results of the current work.

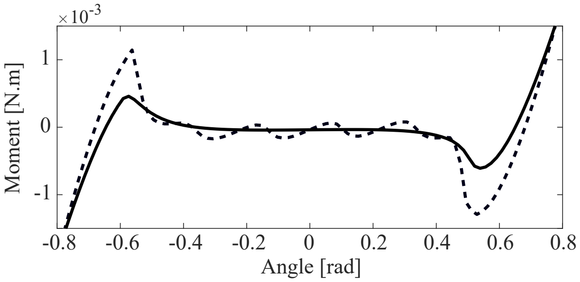

Figure 5.9: The effect of using an insufficient number of slits (n = 7) is shown with a dashed line, and the sufficient number of slits for prototypes and simulations (n = 19) is shown with a solid line.

The experiments and simulations show very similar results and trends, which indicates the validity of the results. There are small discrepancies that can be due to different effects. To begin with, there are geometrical differences between the model and the prototype: in the prototype, a hole in the center was added for prestressing the beams; additionally, small fillets were added between webs and flanges in the actual prototypes to ensure a good connection. The thickness of the prototypes also deviates ±0.05 mm from the model, which can cause differences in the results. Secondly, idealized constraints are applied to the model; however, in reality, making these constraints exactly like simulations is not a viable option. There are a few details that are different in the constraints of the model and experiments, e.g., the way that prestress is applied in the center axis by only constraining one point is not feasible in reality; therefore, a center circle with a 10 mm diameter is prestressed instead in the experiments. Also, there is a difference in the way the rotation is applied to the web in simulation with respect to the experiment. This causes the webs' in-plane sectional deformation to suddenly change its curvature direction upon higher changes in reaction moments as shown in Fig. 5.10. This explains the sharper changes in the reaction moment of the simulation results for larger preloads, see Fig. 5.8(b). In simulations with lower prestress, this behavior is not strong. Therefore, curvier changes between positive and negative stiffness were achieved for the bistable beam. Similarly for neutrally stable beam a smoother change to a flat part was achieved in the experiments comparing to the simulations, as the clamping imperfections gave room for webs to have some deformations during rotation.

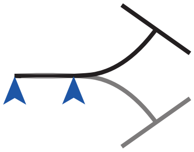

Figure 5.10: The bistable beam's sectional deformation switches from black to gray state upon higher changes in reaction moments.

Another difference can be seen in the stiffness of the beams outside the range of zero or negative stiffness. This is also because of the differences in constraints; in FEM, the movement of the beam in the longitudinal direction (Z) is free, but in experiments, the side clamps also partially limit this movement. This makes the structure stiffer in torsion because the twist is coupled with a shortening in the longitudinal direction. Also, in FEM, the preloading displacement limits the longitudinal movement of the beam's axis in both directions. In experiments, however, it is only done by shortening the axis line with a screw, which only limits movement in one direction. This means that after a certain amount of twist, the beams become short enough to effectively release the preload. This effect is clearly visible in Fig. 5.8(c,d) where the purple line matches the linear red line after a certain amount of twist. Another important observation is that, a rather large hysteresis loop in experiments is captured. This effect is mainly due to the use of nylon as the prototype's material, and this loss of energy due to the internal friction increases as more preload is added to the material. Lastly, some small imperfections can be seen in the data from experiments with the neutrally stable beam, Fig. 5.8(c) red and purple lines. These imperfections are caused by the random contact between middle threaded rod and the structure of the beam.

5.6 Conclusion

We presented two concepts to achieve variable and switchable torsional stiffness from compliant beams using axial preload. The method shows that a variable torsional stiffness range from positive to zero and negative can be achieved by changing the preload of the high-warping-constant beam. It is also demonstrated that by applying the same preload, we can achieve zero torsional stiffness on a near-zero-warping-constant beam and that by increasing this preload, we can achieve an extending range of twisting neutral stability.

The method we used here, which is based on shortening the center axis of the beams, can be used in other ways and for other structures, e.g., wire-frame beam, to control and reduce torsional stiffness. Several techniques, such as thinning toward the center axis or varying the material stiffness toward the outside of the beam, can be used instead of transverse slits. Additionally, other methods for creating the high-warping-constant beam section, such as having curved webs, which can even lessen the stress concentration along the connection of webs and flanges, can also be used.

It is possible to use this element as a part of a larger structure that requires a repetitive simple element, e.g., origami or metamaterials, and evaluating its support stiffness as a revolute joint by changing design parameters, e.g., increasing the number of webs (m) for higher support, can be investigated in future works.

Tuning the torsional stiffness of structures and structures with zero stiffness is an important concern across several fields of research.This concept can be used in several applications where continuous rotation is not required, e.g., flexible medical devices, soft robotics, wearable robotics, legged robots, bio-mimicking robotics, and shape-morphing structures.

References

[1] L. L. Howell, "Compliant mechanisms," in *21st century kinematics*, pp. 189–216, Springer, 2013.

[2] S. G. Nurzaman, F. Iida, L. Margheri, and C. Laschi, "Soft robotics on the move: scientific networks, activities, and future challenges," 2014.

[3] J. Shintake, V. Cacucciolo, D. Floreano, and H. Shea, "Soft robotic grippers," *Advanced materials*, vol. 30, no. 29, p. 1707035, 2018.

[4] R. Mak, A. Amoozandeh Nobaveh, G. Radaelli, and J. L. Herder, "A curved compliant differential mechanism with neutral stability," *Journal of Mechanisms and Robotics*, pp. 1–11, 02 2023.

[5] A. A. Nobaveh and B. Caasenbrood, "Design feasibility of an energy-efficient wrist flexion-extension exoskeleton using compliant beams and soft actuators," in *2022 International Conference on Rehabilitation Robotics (ICORR)*, pp. 1–6, IEEE, 2022.

[6] A. Amoozandeh Nobaveh, G. Radaelli, and J. L. Herder, "A design tool for passive wrist support," in *Wearable Robotics: Challenges and Trends: Proceedings of the 5th International Symposium on Wearable Robotics, WeRob2020, and of WearRAcon Europe 2020, October 13–16, 2020*, pp. 13–17, Springer, 2022.

[7] S. Kota, J. Joo, Z. Li, S. M. Rodgers, and J. Sniegowski, "Design of compliant mechanisms: applications to mems," *Analog integrated circuits and signal processing*, vol. 29, no. 1, pp. 7–15, 2001.

[8] K.-J. Lu and S. Kota, "Design of compliant mechanisms for morphing structural shapes," *Journal of intelligent material systems and structures*, vol. 14, no. 6, pp. 379–391, 2003.

[9] D. Li, S. Zhao, A. Da Ronch, J. Xiang, J. Drofelnik, Y. Li, L. Zhang, Y. Wu, M. Kintscher, H. P. Monner, *et al.*, "A review of modelling and analysis of morphing wings," *Progress in Aerospace Sciences*, vol. 100, pp. 46–62, 2018.

[10] D. van der Lans, A. Amoozandeh Nobaveh, and G. Radaelli, “Reversible shape morphing of a neutrally stable shell by untethered local activation of embedded ni-ti wires,” *Journal of Intelligent Material Systems and Structures*, p. 1045389X221151065, 2023.

[11] H. Greenberg, M. Gong, S. Magleby, and L. Howell, “Identifying links between origami and compliant mechanisms,” *Mechanical Sciences*, vol. 2, no. 2, pp. 217–225, 2011.

[12] K. Kim, H. Heo, and J. Ju, “A mechanism-based architected material: A hierarchical approach to design poisson’s ratio and stiffness,” *Mechanics of Materials*, vol. 125, pp. 14–25, 2018.

[13] A. B. Mackay, D. G. Smith, S. P. Magleby, B. D. Jensen, and L. L. Howell, “Metrics for evaluation and design of large-displacement linear-motion compliant mechanisms,” 2012.

[14] P. Wang and Q. Xu, “Design and modeling of constant-force mechanisms: A survey,” *Mechanism and Machine Theory*, vol. 119, pp. 1–21, 2018.

[15] A. Amoozandeh Nobaveh, G. Radaelli, and J. L. Herder, “Symmetric kinetostatic behavior from asymmetric spatially curved beams,” *Journal of Mechanisms and Robotics*, vol. 15, no. 4, p. 041010, 2023.

[16] G. Radaelli, *Synthesis of mechanisms with prescribed elastic load-displacement characteristics.* PhD thesis, Delft University of Technology, Delft, The Netherlands, 2017.

[17] A. Amoozandeh Nobaveh, G. Radaelli, and J. L. Herder, “Asymmetric spatial beams with symmetric kinetostatic behaviour,” in *ROMANSY 23-Robot Design, Dynamics and Control: Proceedings of the 23rd CISM IFToMM Symposium 23*, pp. 247–254, Springer, 2021.

[18] B. D. Jensen and L. L. Howell, “Bistable configurations of compliant mechanisms modeled using four links and translational joints,” *J. Mech. Des.*, vol. 126, no. 4, pp. 657–666, 2004.

[19] P. G. Opdahl, B. D. Jensen, and L. L. Howell, “An investigation into compliant bistable mechanisms,” in *International Design Engineering Technical Conferences and Computers and Information in Engineering Conference*, vol. 80319, p. V01BT01A046, American Society of Mechanical Engineers, 1998.

[20] G. Radaelli, “Reverse-twisting of helicoidal shells to obtain neutrally stable linkage mechanisms,” *International Journal of Mechanical Sciences*, vol. 202, p. 106532, 2021.

[21] D. Farhadi Machekposhti, N. Tolou, and J. Herder, “A review on compliant joints and rigid-body constant velocity universal joints toward the design of compliant homokinetic couplings,” *Journal of Mechanical Design*, vol. 137, no. 3, p. 032301, 2015.

[22] M. R. Schultz, M. J. Hulse, P. N. Keller, and D. Turse, “Neutrally stable behavior in fiber-reinforced composite tape springs,” *Composites Part A: Applied Science and Manufacturing*, vol. 39, no. 6, pp. 1012–1017, 2008.

[23] J. P. Stacey, M. P. O'Donnell, and M. Schenk, "Thermal prestress in composite compliant shell mechanisms," *Journal of Mechanisms and Robotics*, vol. 11, no. 2, p. 020908, 2019.

[24] T. Murphey and S. Pellegrino, "A novel actuated composite tape-spring for deployable structures," in *45th AIAA/ASME/ASCE/AHS/ASC Structures, Structural Dynamics & Materials Conference*, p. 1528, 2004.

[25] C. Vehar, S. Kota, and R. Dennis, "Closed-loop tape springs as fully compliant mechanisms: preliminary investigations," in *International Design Engineering Technical Conferences and Computers and Information in Engineering Conference*, vol. 46954, pp. 1023–1032, 2004.

[26] S. Guest, E. Kebadze, and S. Pellegrino, "A zero-stiffness elastic shell structure," *Journal of Mechanics of Materials and Structures*, vol. 6, no. 1, pp. 203–212, 2011.

[27] E. Lamacchia, A. Pirrera, I. Chenchiah, and P. Weaver, "Non-axisymmetric bending of thin annular plates due to circumferentially distributed moments," *International Journal of Solids and Structures*, vol. 51, no. 3-4, pp. 622–632, 2014.

[28] K. Seffen and R. McMahon, "Heating of a uniform wafer disk," *International Journal of Mechanical Sciences*, vol. 49, no. 2, pp. 230–238, 2007.

[29] S. Kok, G. Radaelli, A. A. Nobaveh, and J. Herder, "Neutrally stable transition of a curved-crease planar shell structure," *Extreme Mechanics Letters*, vol. 49, p. 101469, 2021.

[30] S. Kok, A. A. Nobaveh, and G. Radaelli, "Neutrally stable double-curved shells by inflection point propagation," *Journal of the Mechanics and Physics of Solids*, p. 105133, 2022.

[31] N. Tolou, V. A. Henneken, and J. L. Herder, "Statically balanced compliant micro mechanisms (sb-mems): Concepts and simulation," in *International Design Engineering Technical Conferences and Computers and Information in Engineering Conference*, vol. 44106, pp. 447–454, 2010.

[32] N. Tolou and J. L. Herder, "Concept and modeling of a statically balanced compliant laparoscopic grasper," in *International Design Engineering Technical Conferences and Computers and Information in Engineering Conference*, vol. 49040, pp. 163–170, 2009.

[33] K. Hoetmer, G. Woo, C. Kim, and J. Herder, "Negative stiffness building blocks for statically balanced compliant mechanisms: design and testing," 2010.

[34] R. Mak, A. Amoozandeh Nobaveh, G. Radaelli, and J. L. Herder, "A curved compliant differential mechanism with neutral stability," in *International Design Engineering Technical Conferences and Computers and Information in Engineering Conference*, vol. 86281, p. V007T07A004, American Society of Mechanical Engineers, 2022.

[35] S. Yuan, Y. Sun, M. Wang, J. Ding, J. Zhao, Y. Huang, Y. Peng, S. Xie, J. Luo, H. Pu, *et al.*, "Tunable negative stiffness spring using maxwell normal stress," *International Journal of Mechanical Sciences*, vol. 193, p. 106127, 2021.

[36] I. K. Kuder, A. F. Arrieta, W. E. Raither, and P. Ermanni, "Variable stiffness material and structural concepts for morphing applications," *Progress in Aerospace Sciences*, vol. 63, pp. 33–55, 2013.

[37] J. Sun, Q. Guan, Y. Liu, and J. Leng, "Morphing aircraft based on smart materials and structures: A state-of-the-art review," *Journal of Intelligent material systems and structures*, vol. 27, no. 17, pp. 2289–2312, 2016.

[38] H. Akhavan, P. Ribeiro, and M. De Moura, "Large deflection and stresses in variable stiffness composite laminates with curvilinear fibres," *International Journal of Mechanical Sciences*, vol. 73, pp. 14–26, 2013.

[39] L. Blanc, A. Delchambre, and P. Lambert, "Flexible medical devices: Review of controllable stiffness solutions," in *Actuators*, vol. 6, p. 23, Multidisciplinary Digital Publishing Institute, 2017.

[40] H. M. Le, L. Cao, T. N. Do, and S. J. Phee, "Design and modelling of a variable stiffness manipulator for surgical robots," *Mechatronics*, vol. 53, pp. 109–123, 2018.

[41] A. Dunning, J. Stroo, G. Radaelli, and J. Herder, "Feasibility study of an upper arm support based on bending beams," in *2015 IEEE International Conference on Rehabilitation Robotics (ICORR)*, pp. 520–525, IEEE, 2015.

[42] S. Jadhav, M. R. A. Majit, B. Shih, J. P. Schulze, and M. T. Tolley, "Variable stiffness devices using fiber jamming for application in soft robotics and wearable haptics," *Soft Robotics*, vol. 9, no. 1, pp. 173–186, 2022.

[43] A. A. Nobaveh, G. Radaelli, W. W. van de Sande, R. A. van Ostayen, and J. L. Herder, "Characterization of spatially curved beams with anisotropically adaptive stiffness using sliding torsional stiffeners," *International Journal of Mechanical Sciences*, vol. 234, p. 107687, 2022.

[44] T. Jin, Z. Liu, S. Sun, Z. Ren, L. Deng, D. Ning, H. Du, and W. Li, "Theoretical and experimental investigation of a stiffness-controllable suspension for railway vehicles to avoid resonance," *International Journal of Mechanical Sciences*, vol. 187, p. 105901, 2020.

[45] P. Bilancia, S. P. Smith, G. Berselli, S. P. Magleby, and L. L. Howell, "Zero torque compliant mechanisms employing pre-buckled beams," *Journal of Mechanical Design*, vol. 142, no. 11, p. 113301, 2020.

[46] J. Li, K. Fu, Y. Gu, and Z. Zhao, "Torsional negative stiffness mechanism by thin strips," *Theoretical and Applied Mechanics Letters*, vol. 9, no. 3, pp. 206–211, 2019.

[47] M. R. Schultz, "A concept for airfoil-like active bistable twisting structures," *Journal of Intelligent Material Systems and Structures*, vol. 19, no. 2, pp. 157–169, 2008.

[48] K. A. Seffen and S. D. Guest, “Prestressed morphing bistable and neutrally stable shells,” *Journal of Applied Mechanics*, vol. 78, no. 1, 2011.

[49] X. Lachenal, S. Daynes, and P. M. Weaver, “A non-linear stiffness composite twisting i-beam,” *Journal of intelligent material systems and structures*, vol. 25, no. 6, pp. 744–754, 2014.

[50] A. A. Nobaveh, J. L. Herder, and G. Radaelli, “A compliant continuously variable transmission (cvt),” *Mechanism and Machine Theory*, vol. 184, p. 105281, 2023.

III

Applications in passive exoskeletons

6

A wrist flexion-extension exoskeleton

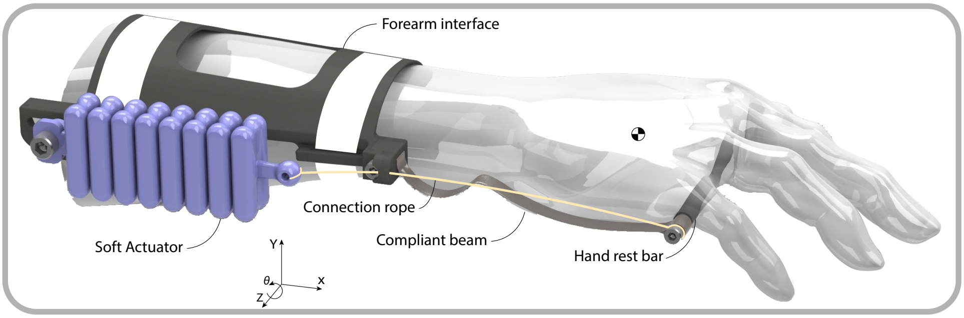

In part I, we covered designs with spatially curved beams. Considering the requirements for wearable devices, simplicity, lightweight, and slenderness are some of the key features. Therefore, utilizing these beams appears to be a promising option. This chapter introduces a wrist exoskeleton where the weight of the hand is balanced using the support provided by the elasticity of the same kind of curved compliant beams that are introduced in part I. The beam that is designed for this purpose is made using the optimization scheme that is described in chapter 2. Furthermore, an active soft actuator from the project's collaborator is added to the design to enhance the range of motion of the wrist flexion – extension exoskeleton.

This chapter was published as:
Amoozandeh Nobaveh, A. and Caasenbrood, B., 2022, July. Design Feasibility of an Energy-efficient Wrist Flexion-Extension Exoskeleton using Compliant Beams and Soft Actuators. *In 2022 International Conference on Rehabilitation Robotics (ICORR)* (pp. 1-6). IEEE.

Design Feasibility of an Energy-efficient Wrist Flexion-Extension Exoskeleton using Compliant Beams and Soft Actuators

Abstract *Passive and active exoskeletons have been used over recent decades. However, regarding many physiological systems, we see that the majority explore both active and passive elements to minimize energy consumption while retaining proper motion control. In light of this, we propose a design that combines compliant mechanisms as passive support for gravity balancing of the hand's weight and soft actuators as active support for wrist flexion-extension. Our approach offers a safe, lightweight solution that intrinsically complements and supports the wrist's degrees of freedom. We hypothesize that the proposed soft wearable device is able to increase the range of motion and reduce muscle fatigue while being energy-conservative by balancing of the passive and active subsystems. In this work, we perform a design feasibility study for such soft wrist exoskeletons, particularly focused on wrist flexion-extension rehabilitation. Through optimization, geometries for the required functionality of the compliant beam and soft actuator are obtained, and their performance as separate subsystems is evaluated by simulations and experiments. Under the appropriate inputs, we show that the system can introduce a controllable bifurcation. Through experiments, we investigate such bi-stability and explore its usefulness for rehabilitative support of wrist flexion-extension. In short, the proposed wearable can offer a viable, energy-efficient alternative to traditional rehabilitation technologies.*

6.1 Introduction

Exoskeletons are a particular research field of robotics aimed at developing wearable robotic systems that augment, enhance, or restore human motor functions [1]. Although the term *"exoskeleton"* was originally used in biology to describe the support and protection of soft organs, it is nowadays recognized as distinct wearable robotic devices that are actively controlled and (fully) autonomous [2]. Besides their applicability in industry [3], they also play a vital role in rehabilitation technology, especially in cases of muscular dystrophy, like post-stroke or Duchenne disease [4]. Persistent and early physical therapy has been shown to restore or improve the longevity of muscular functionality of the paretic limbs [5, 6]. In light of this paradigm, wearable exoskeletons have paved the path towards in-house rehabilitation that can prolong therapy exposure and thereby, its effectiveness. However, there is a lack of solutions to the *"one-strategy-fits-all"* problem, and consequently, proposed exoskeleton frameworks often benefit only a limited group of target patients.

6.1.1 Related works

Passive exoskeletons are being developed primarily to demonstrate that by balancing the weight of body parts, it is possible to significantly reduce the amount of muscular effort, which is required to perform a specific task [7]. This type of exoskeleton is developed to reduce the complexity, cost, and weight of assistive devices [8].

In most of the developed passive exoskeleton concepts, a rigid body mechanism has been used with a close kinematics to the human body and a set of springs or elastic bands to store energy [9, 10]. This combination, however, is inconsistent with the ultimate goal of exoskeletons being slender, and not impeding natural human motion. As a solution to these issues, a relatively new branch of passive exoskeletons has been developed in recent years, utilizing compliant mechanisms to integrate the energy storage and kinematic functionality into a single element. These exoskeletons are scarcer but slowly emerging [11–13].

In contrast to rigid support, soft robots continue the path of lightweight, cost-effective, and safe robotics. By exploring *soft materials*, e.g., silicone rubbers and thermoplastics, the natural compliance of the system can be significantly improved, leading to continuum-bodied motions that are difficult, if not impossible, to achieve for conventional robots. Naturally, these soft robots have major benefits for healthcare and human-robot collaboration [14], where safe and passive interactions are prioritized over the classic robotics requirements, e.g., precision and speed. Several researchers have shown the prominent role soft robots can have in rehabilitation and other assistive technologies. Polygerinos et al. developed a soft robotic glove for hand rehabilitation using pneumatic actuation [15], exploring the flexibility to partially solve the one-fits-all problem. Yap et al. designed a soft actuator with optimal joint placement to maximize the force transferal [16], and other more recent examples of soft exoskeletons include [17, 18].

A major drawback of conventional soft actuators, however, is their limited force and torque transmission. Although softness benefactors safety, it lacks the structural stiffness to efficiently transfer large loads without buckling. A possible solution here might be fiber-reinforced strategies [15, 19] or soft robots that explore semi-rigidity (similar to most physiological systems in biology). Alternatively, Yang et al. proposed a vacuum-actuated muscle-inspired pneumatic structure (VAMPs) that purposefully introduces buckling instability for enhanced actuation strength, whose motions resemble linear actuators in rigid robots [20].

6.1.2 Our contribution(s)

In retrospect to the previous literature, we propose a synergy between the distinct fields of passive muscular support using compliant mechanisms and active support using soft robotics technology. In this work, we primarily focus on a wrist exoskeleton that naturally compliments and supports the flexion-extension of the patient's hand(s). Furthermore, we perform a design feasibility study for a soft wrist exoskeleton. In our analysis, we seek a system that enhances both the range of motion and reduced muscle fatigue while attaining high energy-efficiency through the synergy between passive and active elements. Our contributions presented in this work are listed below:

- Development of a novel and safe design for wrist-support used for gravity-balancing;
- Optimization-driven design of compliant beam and soft robotic actuator;
- Experimental verification of the mechanical behavior of the designed soft wrist exoskeleton, exploring its controllable bi-stable nature for enhanced wrist mobility.

This chapter is organized as follows. First, we discuss the design of the proposed wrist exoskeleton – detailing the passive gravity balancing and the bi-stability mechanism that allows bi-directional mobility through one actuation input and the external stimulus from the user (or patient). Second, we show results from simulations and experiments of each individual sub-component to show the feasibility of the final integrated design. Following, we investigate the bi-stability and its role in the hand's range of motion, followed by a brief discussion and conclusion.

6.2 Design overview

A monolithic compliant mechanism can be an appropriate option for passive gravity balancing of hand without adding a considerable weight or occupying a large space [7, 8]. Among a wide range of possible compliant mechanism topologies, a cantilever beam is chosen as it has a relatively simple and slender topology, which benefits comfort and ease of design. The design objective of the beam is to keep the hand in the straight position without any muscular effort while still giving the user the flexion and extension freedom. In addition to the described passive beam, a tendon-like soft actuator is introduced as an active parallel subsystem. This tendon can help the user cover the hand's range of motion with a minimal effort. As such, the compliant beam balances the hand's dead weight while the soft actuator helps with the hand's movement in its range of motion. The tendon free-end is connected via a thin nylon rope to the endpoint of the compliant beam. This rope passes through the hole at the beam's grounding near the wrist joint. The beam is designed in such a way that the straight posture maximizes the distance between the hand interface and the hole at the wrist joint. Therefore, contraction of the active tendon induces a bi-stable flexion-extension motion around the straight posture of the hand. As a result, only by inducing a minimal flexion or extension from the user, the soft actuator can start helping the hand with its contraction to reach either side of the motion range. In other words, the active actuator for the tendon is designed in such a way that its contraction can have dual effects, similar to the flexor-extensor muscles embedded in the human forearm. The operation of the passive and active subsystems together and their interface with the patient's hand is illustrated in Fig. 6.1 and Fig. 6.2. The following subsections detail the design process for each component of this exoskeleton.

6.2.1 Compliant beam (passive support)

The ultimate goal of the monolithic passive compliant element is to mimic the motion of the hand during wrist flexion-extension while providing balancing support for the hand's weight as a pendulum around the wrist joint.

The steps for designing the required beam are as follows. First, a method for parametrizing the beam shape using B-splines is developed, whose shape is defined by a set of control points. Second, an optimization routine is used to satisfy the balancing kinetostatic

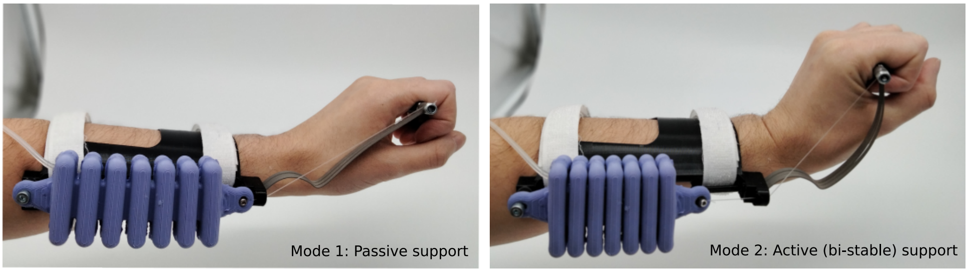

Figure 6.1: An illustration of the energy-efficient wrist exoskeleton that explores the fields of passive compliant beams and active soft actuation. In the zero-input situation (Mode 1 – passive support), the compliant beam balances the weight of the hand. The integration of the soft actuator (Mode 2 – active support) extends the range of motion.

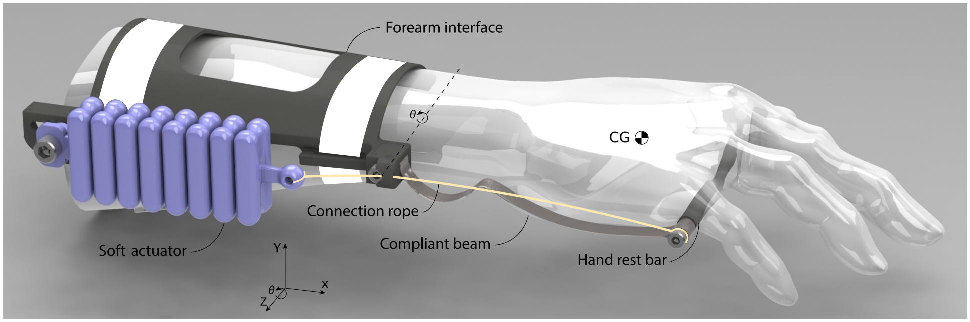

Figure 6.2: An illustration of the concept of the wrist exoskeleton. The compliant beam and soft actuator are both connected to the forearm interface at their grounding. The beam's endpoint is directly connected to the hand bar, and the soft actuator is connected via a nylon rope to the hand interface. The bar is sitting under the roots of the user's fingers.

requirements by tuning these control points as design parameters. In each iteration, the optimizer forms a beam shape based on the control parameters and evaluates the balancing behavior by a set of endpoint incremental loadings from zero to twice the hand's weight. The displacements upon these loadings are numerically computed using a self-developed finite element model. The reader is referred to [12] for more detail.

As for the beam shape parametrization, a degree-four B-spline is used to interpolate the spine shape and the width of the beam based on seven optimized control points as shown in Fig. 6.3. The B-spline is chosen to have an open uniform knot vector to ensure equal weight for each control point and to make the first and last optimized control points coincide with the first and last parameters of the beam itself. Using B-spline interpolation not only reduced the parameters, but also caused a smooth transition between the optimized parameters of the beam and avoided any discontinuities that could have happened due to sudden dimensional changes in the finite element model.

The beam is designed to be made with a 2D fabrication method out of planar material. Therefore, a rectangular cross-section with a fixed width (9 mm) is selected for it. Based on this assumption, a set of parameters including two Cartesian coordinates and one thickness at each control point (21 parameters) are subjected to optimization.

For the optimizer, the *Multi Start* option from *optimization toolbox* of Matlab® is used. To increase the chance of having a better optimum solution, five random starting points are selected for the main *fmincon* function with *Interior-Point* as the algorithm. Upper and lower constraints are set for coordinates to keep the beam shape in a limited design space.

Table 6.1: The flexion-extension and pronation angles of the beam's endpoint from experiments and simulations.

	Extension+/Flexion- (deg)		Pronation (deg)	
load (g)	model	experiments	model	experiments
$\delta = 0$	+57	+50	0	0
$\delta = 100$	+50	+43	1.1	9.3
$\delta = 200$	+32	+26	2.5	25.7
$\delta = 300$	+10	+14	4.6	34.1
$\delta = \delta_W$	-5	+2	7.4	35.2
$\delta = 500$	-15	-7	10.6	37.7
$\delta = 600$	-22	-12	14.2	37.9
$\delta = 700$	-27	-15	18	38.3
$\delta = 800$	-32	-21	22.1	38.7

It is desired that the mechanism has a minimum effect on supination-pronation angle and keeps it as straight as possible. However, as the mechanism is on the side of the hand and the beam is designed to be planar, it is inevitable to have some pronation. The range of motion for supporting the user hand is set to reach $\theta = \pm 30^\circ$ for flexion-extension from straight posture with 50% less muscular effort. The hand's weight assumed to be $\delta_W = 400\,\mathrm{g}$, with its center of gravity (CG) in 0.07 m from the wrist joint itself in X direction, and 0.045 m in Z direction from the outer side of hand as illustrated in Fig. 6.2.

A self-developed solver using geometrically nonlinear co-rotational beam elements, based on the Euler-Bernoulli formulation, is used for modeling of the beam behavior. The details of this solver can be found in [21]. The final topology of the beam and the thickness at each of the control points (in millimeters) are shown in Fig. 6.3 (left).

To validate the beam performance, experiments are conducted to show the flexion-extension and inevitable pronation behavior of the beam. The prototype for these experiments is made from spring steel (AISI 301) with an elastic modulus of $E = 190\,\mathrm{GPa}$ and a shear modulus of $G = 72\,\mathrm{GPa}$ (identical to simulation). The experiments include clamping the beam at the grounding point and using different suspended weights $\delta \in [0, 800]$ g at the endpoint. The deflection of the beam is measured by comparing the endpoint position of the loaded and unloaded states with image processing using images from two perpendicularly located cameras, one for flexion-extension and one for pronation. The experiment is shown in Fig. 6.4. The endpoint positions of the beam, which result from the experiments, are shown with ∘ in Fig. 6.3. In this figure, it is possible to compare the flexion-extension angles under different loadings from experiments and modeling. The angle information is shown in Table 6.1.

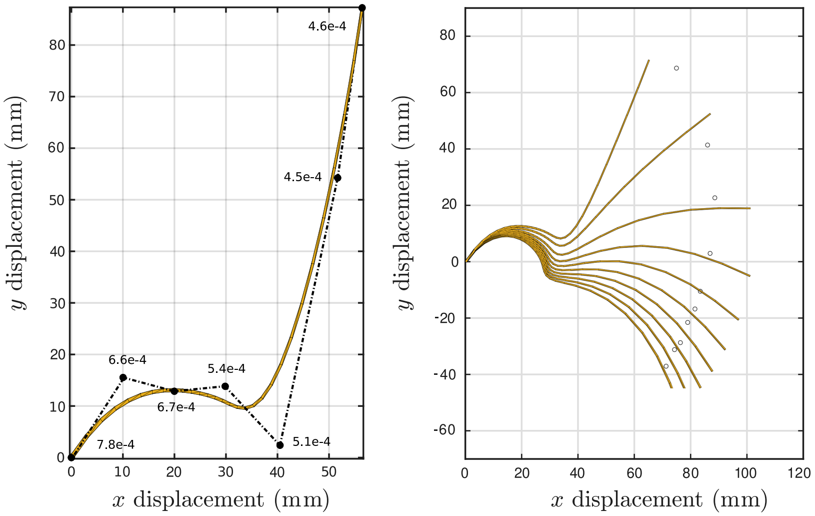

Figure 6.3: (Left) The optimized control points and thicknesses in each point and the final beam shape based on the control parameters. (Right) The (nonlinear) elastic deformation of the complaint beam under incremental vertical loadings at the tip.

6.2.2 Vacuum-actuated soft actuator (active support)

In this section, we will discuss the development of the active soft robotic muscle that ultimately acts as an active supportive layer to the wrist exoskeleton. In particular, for patients that suffer from muscular dystrophy, where muscle forces are significantly reduced, the soft actuator could potentially substitute or increase muscular strength. Similar to human muscles, we aim to seek a soft actuation subsystem that can undergo rapid contraction and relaxation. Here, we have chosen a vacuum-actuated muscle-inspired soft actuator design loosely inspired by the designs of [20]. These soft actuators use buckling of elastomeric structures to generate muscle-like motions when negative pressure (vacuum) is applied; the external (ambient) pressure causes their cooperative, reversible collapse. The soft material chosen to develop the soft actuator is two-component platinum cured silicone *Smooth-Sil 945* with a 45A shore hardness ($E = \pm 1.52$ MPa Young's modulus). To design the geometry of these soft actuators, we again explored an optimization-based design approach. However, contrary to the previous beam optimization, a nonlinear-topology optimization scheme is used to find the optimal two-dimensional material layout that maximizes contraction-like displacement when subjected to negative differential pressure. This forms a highly-nonlinear optimization problem, and the reader is referred to [22] for more detail on the method and solver. The optimization result can be found in Fig. 6.5, together with the experimental results of the final soft muscle.

To validate the performance of the vacuum-driven soft actuator, we developed a uni-axial benchmark test that can measure the contraction displacement, denoted here by $s(t)$, with respect to the negative pressure input $u(t)$. The intrinsic length of the soft actuator is given by $s_0 = 160.25$ mm. The pressure input is defined as a relative pressure difference, i.e., the pressure potential with the ambient pressure $u(t) = p(t) - p_{\text{atm}}$ with $p_{\text{atm}} \approx 101.33$

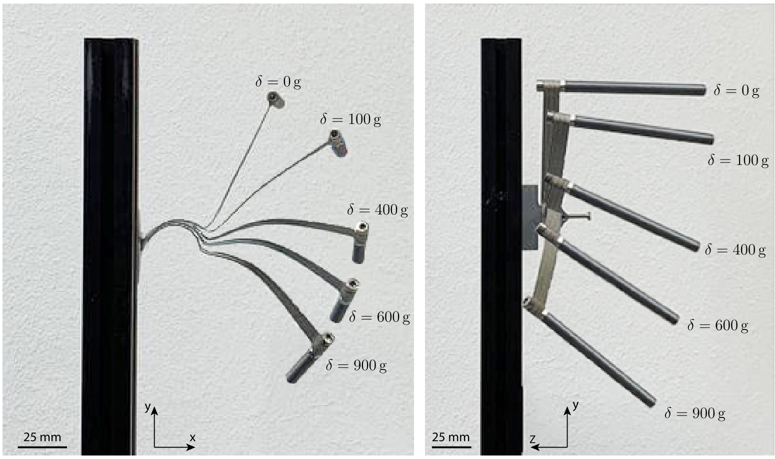

Figure 6.4: An illustration of experimental results. Here the load δ is applied at the CG of the wrist, illustrating both flexion-extension and pronation mobility in the complaint beam.

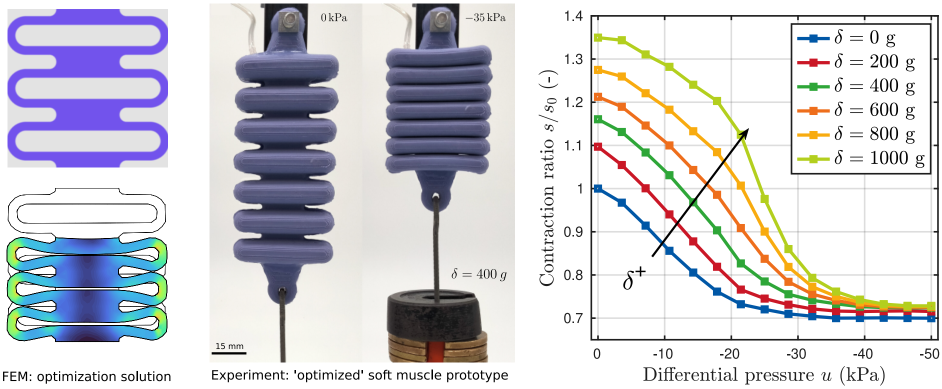

FEM: optimization solution

Experiment: 'optimized' soft muscle prototype

Figure 6.5: (Left) Exemplary benchmark test of the vacuum-actuated soft actuator subjected to a loading weight of $\delta = 400$ g. Here we clearly see the soft subsystem being sufficiently strong to lift the suspended-weight for a differential pressure of $u = -35\,\mathrm{kPa}$. (Right) The quasi-static evolution of the contraction displacement $s(t)$ against different input pressures $u(t)$ for different suspended weights δ. As expected, a decreasing slope for larger suspended weights can be seen. Although the actuator can lift $\delta > 1000g$, the contraction amplitudes significantly diminish beyond its practical use.

kPa. To investigate the force transmission of the proposed soft actuation, we subject the system to a range of suspended weights $\delta \in [0, 1000]$ g. In Fig. 6.5, we show an example of such benchmark tests for $\delta = 400$ g (i.e., the average weight of the human hand). The evolution of all contraction ratios for the remaining loading scenarios are also shown in Fig. 6.5.

First of all, as expected, we observe that the soft actuator has a bounded contraction range, roughly ±30% contraction for $\delta = 0$, and ±65% contraction for $\delta = 1000$ g. Please note that the increase of +35% work range is caused by pre-stretching of the soft actuator. Regarding the force transmission, we observe that the soft actuator is sufficiently strong to produce a wide range of forces – whose loading conditions should not exceed $\delta > 1000$ to prevent tearing. For the no-load condition ($\delta = 0$), we observe that the necessary differential pressure required is less than −35 kPa, slowly increasing towards −50 kPa for increasing loads δ. Clearly, the trend of the contraction w.r.t. to the pressure input is nonlinear. However, the trend w.r.t. the loading δ appears to be closely linear. These observations indicate that the soft actuator possesses dual control functionality, namely as an actuator and a variable stiffness. As a result, a merit benefit of such soft actuation systems is their low energy consumption, only requiring an influx of energy when switching between the states. Although this process is nearly reversible (assuming minimal temperature exchange with the environment), it is difficult to realize it in practice.

Let it be clear that the proposed soft wrist exoskeleton is not fully back-driveable. Only contractile motion of the soft actuator is feasible, yet positive pressures can ensure that the rest configuration is reached faster. However, (large) compressive forces will eventually result in structural buckling. A possible solution to the system in Fig. 6.2 might be antagonistic soft muscle pairs, similar to a flexor-extensor muscles.

6.3 Exploring the bi-stability property

To show the feasibility of the overall design, we combine the compliant beam of Section 6.2.1 and the vacuum-actuated soft actuator in Section 6.2.2, giving rise to the soft wrist exoskeleton as shown in Fig. 6.1. The goal is to investigate the feasibility of such design to support the whole range of motion of hand by exploiting the aforementioned bi-stability property. If the internal pressure in the soft actuator is $u = 0$, the exoskeleton will default to its gravity balancing stability for the load $\delta = \delta_W$, i.e., $\theta = 0$ (or close to zero, see Table 6.1). This is the global minimizer of the potential energy of the wrist exoskeleton without control. However, if the internal pressure in the soft actuator is non-zero, this induces a force inbalance between the gravitational component of the hand, the compliance of the beam, and contraction force of the soft actuator. Since the tendon of the soft actuator is in its most extended form in the straight posture of the hand ($\theta = 0$), the contraction of the tendon can lead to two unique (stable) equilibria. In this analysis, we load the wrist exoskeleton with the average human-hand weight δ_W, and investigate the bi-stability for various pressure inputs $u \in [-40, 0]$ kPa. These experimental results are shown in Fig. 6.6.

As can be seen, there indeed exist pairs of stable equilibria for identical input conditions. We see that for low differential pressures (i.e., $u \geq -8$ kPa), only one stable equilibrium $\theta^* = 0$ exists (passive gravity balancing). Further increasing the negative pressure input u, we observe a so-called bifurcation point, where $\theta^* = 0$ is now unstable and two new stable equilibria appear, $\theta^*_- < 0$ (down/flexion) and $\theta^*_+ > 0$ (up/extension), respectively. The change of stability in the zero position θ^* is actually beneficial, as it allows the user to switch to flexion or extension with limited effort. It is worth noting that the pair of equilibria can be tuned accordingly by changing the input u. Let it be clear that the magnitude of the flexion equilibrium is lower than the extension angle since the soft actuator has to

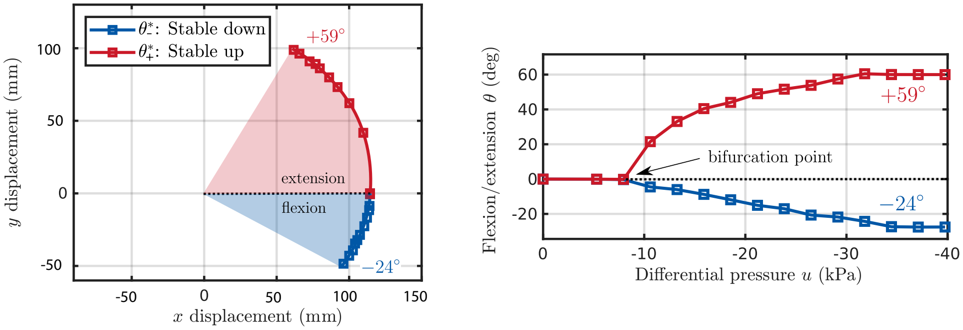

Figure 6.6: Experimental results of the bi-stability analysis. Here we see the transition of one stable equilibrium ($\theta^* = 0$) for low-pressure, to an unstable equilibrium and two stable equilibrium pairs θ^*_-, θ^*_+.

further deform the compliant beam. Nevertheless, given the full actuation range of the soft actuator, we observe a substantial range of support ($|\theta^*_-| \le 24^\circ$ for flexion, $|\theta^*_+| \le 59^\circ$ for extension) for wrist mobility, indicating such hybrid system can be a viable, energy-efficient alternative to traditional wrist exoskeletons.

6.4 Discussion

The results of the compliant beam and soft actuator experiments indicate that both subsystems satisfied the required share for balancing and actuating the user's hand, while the combination of both subsystems demonstrated the hypothesized bi-stable behavior, indicating that such design can support the hand in flexion-extension direction over a broad range of motion. This is further supported by the fact that the dead weight of the hand is balanced during actuation, the active support can greatly minimize the actuation energy. Additionally, both passive and active elements do not require energy to maintain an angle. Thus, when the device is turned off, it can be employed as a fully passive support or as a posture fixation for the hand's flexion-extension.

It is worth mentioning that this device is created to function as a semi-active gravity balancer. As a result, the orientation of the user hand must always match the direction illustrated in Fig. 6.2. However, this is not a significant concern because the majority of the device's intended users, e.g., people with Duchenne disease, preferably have their hands on the armrest of the wheelchair.

The device demonstrates a substantial support angle (83°) for hand flexion-extension. This range is sufficient for the majority of the hand placement and range of motion tasks required to perform activities of daily living [23]. However, this range can still be enhanced in order to make it more symmetrical in terms of flexion and extension. For instance, a closed-loop control scheme can be proposed that counteracts the stiffness of the compliant beam under compression.

Nevertheless, there are still some limitations to the current design. First, additional experiments, modeling, and testing are required with patients to arrive at a final design that well integrates both subsystems – especially for user clinical tests. The proposed bi-stable property can still be improved by tweaking the individual subsystems and the connections between them. Additionally, patient tests might highlight constraint or comfort issues, e.g., limited wrist supination-pronation, that are currently not investigated. In future work, we will extend to patient trails.

6.5 Conclusion

A novel design for energy-efficient wrist exoskeletons is presented that utilizes a compliant mechanism and soft actuation to exploit both passive and active support elements simultaneously. The compliant beam is optimized, and the experiments indicated that it can balance the hand's dead weight over the desired range of motion. The topology-optimized soft actuator has demonstrated the ability to sustain the needed contraction force for hand flexion-extension. The combination of these two subsystems into a singular exoskeleton proved that the proposed bi-stable behavior of exoskeletons is capable of achieving both flexion and extension via actuator contraction in an extended range of motion (83°). This unique soft exoskeleton can be used in two modes: *(i)* when the passive part maintains the hand in its straight position and allows for a range of motion with lower muscular force; *(ii)* by engaging the soft actuator and active support of the body. Given these preliminary insights, such a semi-active wrist exoskeleton can be utilized to support other body parts while complementing the part's natural movement and requiring reduced energy consumption.

References

[1] S. Mohammed, Y. Amirat, and H. Rifai, "Lower-limb movement assistance through wearable robots: state of the art and challenges," *Advanced Robotics*, vol. 26, no. 1-2, pp. 1–22, 2012.

[2] C. Yang, J. Zhang, Y. Chen, Y. Dong, and Y. Zhang, "A review of exoskeleton-type systems and their key technologies," *Proceedings of the Institution of Mechanical Engineers, Part C: Journal of Mechanical Engineering Science*, vol. 222, no. 8, pp. 1599–1612, 2008.

[3] M. P. De Looze, T. Bosch, F. Krause, K. S. Stadler, and L. W. O'sullivan, "Exoskeletons for industrial application and their potential effects on physical work load," *Ergonomics*, vol. 59, no. 5, pp. 671–681, 2016.

[4] J. Weichbrodt, B.-M. Eriksson, and A.-K. Kroksmark, "Evaluation of hand orthoses in duchenne muscular dystrophy," *Disability and rehabilitation*, vol. 40, no. 23, pp. 2824–2832, 2018.

[5] D. X. Cifu and D. G. Stewart, "Factors affecting functional outcome after stroke: a critical review of rehabilitation interventions," *Archives of physical medicine and rehabilitation*, vol. 80, no. 5, pp. S35–S39, 1999.

[6] C. L. Flick, "Stroke rehabilitation. 4. stroke outcome and psychosocial consequences," *Archives of physical medicine and rehabilitation*, vol. 80, no. 5, pp. S21–S26, 1999.

[7] T. Bosch, J. van Eck, K. Knitel, and M. de Looze, “The effects of a passive exoskeleton on muscle activity, discomfort and endurance time in forward bending work,” *Applied ergonomics*, vol. 54, pp. 212–217, 2016.

[8] L. F. Cardoso, S. r. Toma´ zio, and J. L. Herder, “Conceptual design of a passive arm orthosis,” in *International Design Engineering Technical Conferences and Computers and Information in Engineering Conference*, vol. 36533, pp. 747–756, American Society of Mechanical Engineers, 2002.

[9] T. Rahman, W. Sample, S. Jayakumar, M. M. King, *et al.*, “Passive exoskeletons for assisting limb movement,” *Journal of rehabilitation research and development*, vol. 43, no. 5, p. 583, 2006.

[10] P. N. Kooren, A. G. Dunning, M. M. Janssen, J. Lobo-Prat, B. F. Koopman, M. I. Paalman, I. J. de Groot, and J. L. Herder, “Design and pilot validation of a-gear: a novel wearable dynamic arm support,” *Journal of neuroengineering and rehabilitation*, vol. 12, no. 1, pp. 1–12, 2015.

[11] M. Tschiersky, E. E. Hekman, D. M. Brouwer, and J. L. Herder, “Gravity balancing flexure springs for an assistive elbow orthosis,” *IEEE Transactions on Medical Robotics and Bionics*, vol. 1, no. 3, pp. 177–188, 2019.

[12] A. Amoozandeh Nobaveh, G. Radaelli, and J. L. Herder, “A design tool for passive wrist support,” in *International Symposium on Wearable Robotics*, pp. 13–17, Springer, 2020.

[13] S. E. Chang, T. Pesek, T. R. Pote, J. Hull, J. Geissinger, A. A. Simon, M. M. Alemi, and A. T. Asbeck, “Design and preliminary evaluation of a flexible exoskeleton to assist with lifting,” *Wearable Technologies*, vol. 1, 2020.

[14] C. Thalman and P. Artemiadis, “A review of soft wearable robots that provide active assistance: Trends, common actuation methods, fabrication, and applications,” *Wearable Technologies*, vol. 1, 2020.

[15] P. Polygerinos, K. C. Galloway, E. Savage, M. Herman, K. O’Donnell, and C. J. Walsh, “Soft robotic glove for hand rehabilitation and task specific training,” *Proceedings - IEEE International Conference on Robotics and Automation*, pp. 2913–2919, 2015.

[16] H. K. Yap, J. H. Lim, F. Nasrallah, J. C. Goh, and R. C. Yeow, “A soft exoskeleton for hand assistive and rehabilitation application using pneumatic actuators with variable stiffness,” *Proceedings - IEEE International Conference on Robotics and Automation*, vol. 2015-June, no. June, pp. 4967–4972, 2015.

[17] S. Liu, Z. Fang, J. Liu, K. Tang, J. Luo, J. Yi, X. Hu, and Z. Wang, “A Compact Soft Robotic Wrist Brace With Origami Actuators,” *Front. Rob. AI*, vol. 0, 2021.

[18] D. Chiaradia, L. Tiseni, M. Xiloyannis, M. Solazzi, L. Masia, and A. Frisoli, “An Assistive Soft Wrist Exosuit for Flexion Movements With an Ergonomic Reinforced Glove,” *Front. Rob. AI*, vol. 7, 2020.

[19] G. Klute, J. Czerniecki, and B. Hannaford, "Mckibben artificial muscles: pneumatic actuators with biomechanical intelligence," in *1999 IEEE/ASME International Conference on Advanced Intelligent Mechatronics (Cat. No.99TH8399)*, pp. 221–226, 1999.

[20] D. Yang, M. S. Verma, J. H. So, B. Mosadegh, C. Keplinger, B. Lee, F. Khashai, E. Lossner, Z. Suo, and G. M. Whitesides, "Buckling Pneumatic Linear Actuators Inspired by Muscle," *Advanced Materials Technologies*, vol. 1, no. 3, pp. 31–33, 2016.

[21] A. A. Nobaveh, G. Radaelli, and J. L. Herder, "Asymmetric spatial beams with symmetric kinetostatic behaviour," in *Symposium on Robot Design, Dynamics and Control*, pp. 247–254, Springer, 2020.

[22] B. Caasenbrood, A. Pogromsky, and H. Nijmeijer, "A Computational Design Framework for Pressure-driven Soft Robots through Nonlinear Topology Optimization," in *2020 3rd IEEE International Conference on Soft Robotics, RoboSoft 2020*, pp. 633–638, 2020.

[23] J. Ryu, W. P. Cooney III, L. J. Askew, K.-N. An, and E. Y. Chao, "Functional ranges of motion of the wrist joint," *The Journal of hand surgery*, vol. 16, no. 3, pp. 409–419, 1991.

7

A compliant differential mechanism

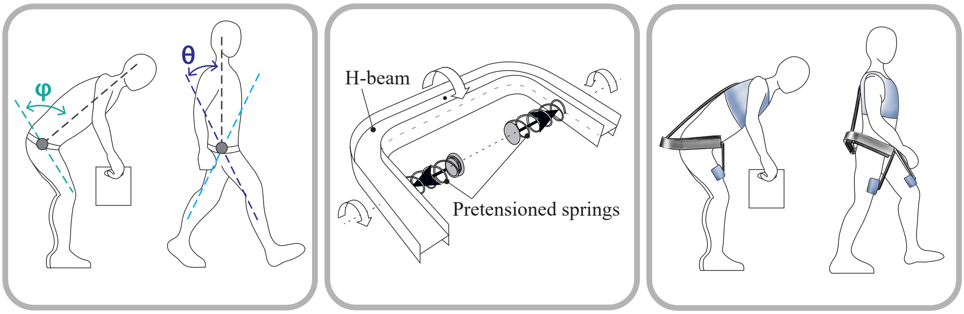

This chapter presents a design for a lightweight compliant differential mechanism based on the knowledge developed in Part II. Firstly, the warping principle from chapter 4 was used to couple the legs' reverse motion, and in the second step, a prestressing technique based on what was presented in chapter 5 was applied to provide zero stiffness for this differential mechanism in its range of motion. Passive back support exoskeletons have a way to store energy during forward bending and give it back once the user requires support. The energy storage mostly works based on the angle between the user's upper body and the legs. It is an effective method for supporting forward bending. However, this upper-body-to-lower-body angle also constantly changes when the user is walking with the exoskeleton. This means that the passive exoskeleton applies forces on the body with every step during walking, which can be very disturbing. One solution to this problem is using a differential mechanism to connect the legs' mirrored motion on the sides while keeping the middle connection to the upper body straight during walking. During forward bending, when both legs' angles change in relation to the upper body, this differential locks to support the user. However, using conventional differential mechanisms in this context, adds a large amount of weight and bulk. This chapter introduces a compliant solution for the differential mechanism with remote center of rotation to be around the body and without exerting any forces to the body in its range of motion.

This chapter was published as:

A curved compliant differential mechanism with neutral stability

Abstract *Differential mechanisms are remarkable mechanical elements that are widely utilized in various systems; nevertheless, conventional differential mechanisms are heavy and difficult to use in applications with limited design space. This chapter presents a curved differential mechanism that utilizes a lightweight, compliant structure. This mechanism acquires its differential characteristic by having a high rotational stiffness when the mechanism is symmetrically actuated on two sides, while having a low rotational stiffness when actuated only on one side. To make the mechanism neutrally stable, the intrinsic elastic strain energy required for deformation of the compliant differential is compensated for by the reintroduction of potential energy, which is provided by two preloaded springs. The rotational stiffness of the one-sided actuation of the compliant differential mechanism around the neutral position is hypothesized to be adjustable by changing the preload of the springs. The stiffness can be positive, zero, or negative, indicating that the mechanism can be neutral or bistable. This hypothesis is investigated using a simulated model in Ansys Parametric Design Language using optimized parameters to achieve the desired stiffness for the mechanism. The simulated model is validated using an experimental setup for both the one-sided and symmetrical actuation stages. The experimental results showed a high correlation with the simulation results. The mechanism with optimized dimensions and preload demonstrated neutral stability over a* 16° *range. Bistability was discovered for preloads greater than the optimized preload. At* $\theta = 0$, *a linear relationship was discovered between the spring preload and the rotational stiffness of the mechanism. Furthermore, an output/input kinematic performance of 0.97 was found for the simulated results and 0.95 for the experimental results.*

7.1 Introduction

The first recorded instance of a differential mechanism being used in a mechanism was over 2000 years ago in the Antikythera mechanism, which used differential gears [1]. The differential mechanism was used to determine the angle between the ecliptic positions of the Sun and Moon. Other uses of differential mechanisms in history are for the use as a compass around 250 AD by engineer Ma Jun [2], or by clockmaker Joseph Williamson in a clock mechanism. One of the most known uses for differential mechanisms is as an automobile differential, which was invented by Onésiphore Pecquer in 1827 [3]. In this long

---

Mak, R., Amoozandeh Nobaveh, A., Radaelli, G. and Herder, J.L., 2023. A curved compliant differential mechanism with neutral stability. *Journal of Mechanisms and Robotics*, pp.1-11.

history of differential mechanisms, only conventional mechanisms using predominantly gears were found. Only one compliant differential mechanism by Valentijn was found [4]. He used a thin-walled warping beam to create differential behavior in his mechanism. The principle of using warping for rotational transmission is explained in [5].

Compliant mechanisms are mechanisms that use elastic deformation to accomplish something useful [6]. Traditionally, when designers needed movement within a mechanism, they only used rigid bodies connected with hinges and sliding joints. However, when you look at nature, much more flexibility in movement can be seen. Think of bee wings, elephant trunks, eels, seaweed, spines, and the blooming of flowers. Very compact mechanisms using this flexible behavior can be seen in nature. Compliant mechanisms have many advantages, such as significantly lower cost due to fewer parts and monolithic construction, increased precision due to reduced wear and eliminated backlash, no need for lubrication, and generally a reduction in mass and size. However, compliant mechanisms also introduce some challenges, such as a more difficult simultaneous design process for motion and force behavior, fatigue life needs to be addressed, the motion is often more limited than traditional rigid-link mechanisms with no continuous rotation possible, there are higher stress concentrations, and most importantly, they require energy during movement due to elastic deformation [7].

A way to have the benefits of a compliant mechanism, but eliminate the energy stored during elastic deformation, is to make the mechanism neutrally stable [8–11]. This technique was also widely used in compliant flexural pivots to make them neutrally stable in a certain range of motion [12, 13]. If the input and output energies of the mechanism are the same over a range of motion, the potential energy will be constant with the initial assumption that the system is isolated and conservative [10]. Several equivalent descriptions for this behavior exist, such as neutral stability, continuous equilibrium, constant potential energy, or zero stiffness [11]. A method to make a mechanism neutrally stable is to reintroduce energy into the energy stream between the input and output of the system [14].

There are multiple ways to store the potential energy in a system to compensate for the elastic strain energy. This could be done by creating prestresses in the material [11, 15] or during the assembly process [16, 17]. Prestressing is also possible by adding an external compensator, which can be another compliant element or a conventional element like a spring. An example of a mechanism that uses an external prestressed compensator is proposed by Herder [18], who added a rolling-link spring mechanism to a compliant laparoscopic grasper to eliminate stiffness in this compliant grasper. This idea was further developed by Stapel, who proposed preloaded compliant flexures to reduce the stiffness of the aforementioned compliant laparoscopic grasper [19]. Although the storage and reintroduction of potential energy have been widely exploited in the past to create compliant mechanisms with zero stiffness, no neutrally stable compliant differential mechanism has been reported.

The goal of this work is to demonstrate the use of a compliant differential mechanism in conjunction with a stiffness reduction technique by reintroducing energy to compensate for the potential elastic strain energy within the range of movement of the mechanism. Reintroduction of energy changes the stiffness of the mechanism from positive stiffness to zero stiffness or negative stiffness. The behavior of the mechanism is investigated and enhanced using simulations and optimization. The simulated results are validated using an experimental setup with a physical prototype. The experiments show a good match between anticipated and actual results in adjusting the stiffness and achieving high kinematic performance.

In Section 7.2 the working principle and intended application of the mechanism are explained. In Section 7.3 the details of the modeling together with the experimental setup are explained. In Section 7.4 the results of both the simulations and experimental setup are shown and discussed in Section 7.5. Finally, in Section 7.6, a conclusion is drawn from the results.

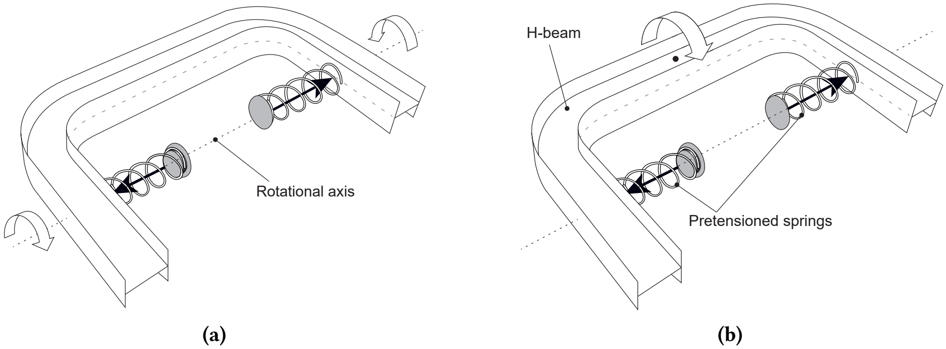

Figure 7.1: A schematic view of the compliant differential mechanism. The dotted line indicates the rotational axis of the mechanism and the arrows show the rotation around each side of the mechanism and the middle output. The pretensioned springs are used to compensate the energy required for compliant mechanism's elastic deformation. (a) The one-sided input to output connection is with zero stiffness and energy free. (b) The symmetric drive from the middle to the side outputs has a very high stiffness.

7.2 Working Principle

The compliant differential mechanism can be seen in Fig. 7.1. The mechanism works by having two pretensioned springs pushing outwards on the inside of the U-shaped open section thin-walled beam. While actuating the mechanism on one side, an opposite rotation on the other side of the mechanism is generated. This one-sided actuation can be seen in Fig. 7.1(a) and Fig. 7.2. During this actuation, the springs are decompressed and transfer their potential energy into the energy required for the elastic deformation of the mechanism. The springs are constrained to be always aligned with the rotational axis of the mechanism, in this way, the springs only experience compression and decompression without any translation or bending in other directions. The transfer of energy causes the energy required to actuate the mechanism to be lower, which in turn lowers the rotational stiffness of the mechanism in one-sided actuation mode, while the symmetrical actuation mode still has a very high rotational stiffness. This latter actuation mode can be seen in Fig. 7.1(b). This mechanism has the interesting behavior of a differential mechanism.

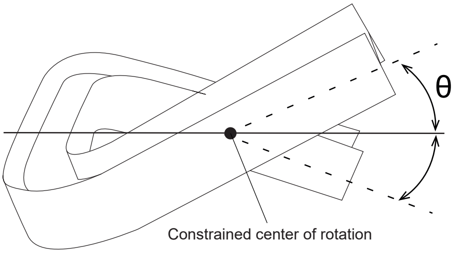

Figure 7.2: A side view of the one-sided actuation, θ indicates the angular displacement of the input. The motion transferred to the output can also be seen on the other side of the mechanism.

The mechanism is hypothesized to work in a way in which the required elastic strain energy is compensated with a source of potential energy. When the mechanism is actuated on one side, the sides of the beam go out of plane and make skew lines, this causes the springs to decompress and go to a lower energy state. At the same time, the U-shaped beam is going to a higher energy state during elastic deformation. The sum of these two energies can be designed to be the constant. Due to the conservation of energy in an isolated and conservative mechanical system [10], the total potential elastic energy of all components would then be expected to look like Fig. 7.3, the dotted line is the potential spring energy of the two springs, the dashed line is the potential elastic strain energy of the mechanism. The total potential energy can be found by the summation of both the potential energy of the beam and the potential energy of the springs. This total energy is illustrated by the solid line, for which a constant level can be observed for a range of motion. This constant potential energy can be categorized as “neutral stability”. The second derivative of the potential energy is the stiffness, so when the potential energy is constant, the stiffness and actuation force of the mechanism are both zero.

If the springs lose more energy than the energy required for the elastic deformation of the beam, a different behavior will be observed, which will create a peak in the potential energy with two minima on each side. This behavior would be classified as bistable, with two stable equilibrium points at the two local minima and an unstable equilibrium point at the peak of the potential energy. This unstable equilibrium indicates a negative stiffness when the potential energy is differentiated twice.

This would indicate that three different states can be achieved. A state with positive stiffness when no or insufficient energy compensation is used. A state with zero stiffness when the potential elastic strain energy is perfectly compensated. And lastly, a state with negative stiffness occurs when the stored potential energy released is greater than the potential elastic strain energy required to actuate the mechanism. The released energy of the spring is a function of the initial preload, stiffness, and amount of decompression of the spring.

This behavior of varying the stiffness of the mechanism, specifically the zero stiffness state is further investigated and validated on a physical prototype.

The original design purpose of this compliant differential mechanism was for the use in a passive exoskeleton as a back support where the U-shaped beam is located around the waist, with the two sides connected to the legs and the middle part connected to the

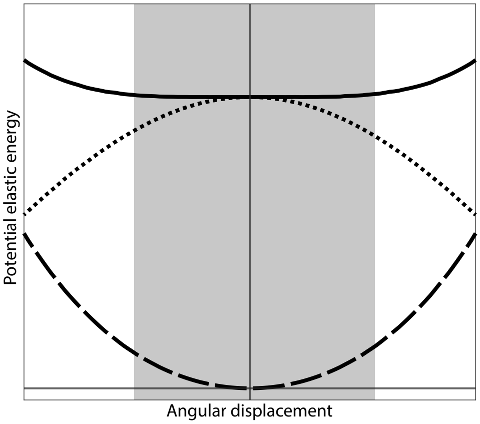

Figure 7.3: The hypothesized total potential elastic energy (solid line) of the neutrally stable mechanism in its range of motion. This line is a summation of the energy of the beam (dashed line) during elastic deformation and the potential energy of the pretensioned springs (dotted line). The range of motion with a constant total potential energy is shown in gray.

upperbody. During walking, you have alternating hip flexion on one side and hip extension on the other side. When bending there is hip flexion on both sides of the hip joint simultaneously. For this use case, it is required that the mechanism have low stiffness when walking and high stiffness when bending. This makes the users walking easy and energy free while this high stiffness provides bending support. These two cases are referred to in this chapter as one-sided actuation and symmetrical actuation respectively. Such a mechanism can be labeled as a differential mechanism.

The mechanism is required to be around the human body but still have a rotational axis that aligns with the rotational axis of the human hip joint. Therefore, a U-shaped beam is chosen with constraints on the side of the human hip to create a rotation axis around these constraints. In this research, this application was chosen as the basis for all parameters, requirements, and optimized values. The parameters are therefore chosen on the basis of human-sizes and can be changed to suit other applications.

7.3 Methods

The mechanism consists of a thin-walled beam, with an H-shaped cross-section, which has two bends forming a U-shape geometry. The mechanism can be found in Fig. 7.1 and Fig. 7.4. A force is applied to the sides of the mechanism at points L and R using two springs. The aim is to research and analyze the neutral stability and bistability behavior of the mechanism and the changes in rotational stiffness due to the reintroduction of potential energy by changing spring parameters. Furthermore, the characteristics and performance of this mechanism as a compliant differential are analyzed using simulations and experimental results for various initial spring preloads.

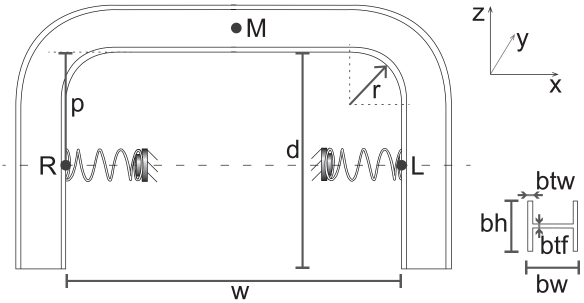

Figure 7.4: The compliant differential mechanism investigated in this research is shown with its parameters. The location of the applied constraints and spring forces are also shown.

7.3.1 Requirements

The mechanism is subjected to the requirements which are set for the aforementioned case of a passive exoskeleton. For this case, the one-sided actuation is used for walking, and the symmetrical actuation is used as a support for bending. In this research, a linearly increasing moment for symmetrical actuation is set to reach 30 N m after 20° of angular displacement. For the one-sided actuation scenario, the maximum moment for the one-sided actuation should be lower then 5 N m with a range of motion of 50°, between −25° and 25° for each side. Furthermore, the mechanism should be as compact and lightweight as possible.

7.3.2 Geometry

The geometry of the mechanism can be found in Fig. 7.4. The cross-section of the beam was chosen to be H-shaped. This cross-section was chosen due to initial tests showing cross-sections with low torsional stiffness, high bending stiffness, and a high warping constant would perform better for the desired differential behavior.

The mechanism is constrained at 3 points, each constraining 2 degrees of freedom, thus, a total of 6 degrees of freedom are constrained in this monolithic mechanism, which makes it iso-constrained. The locations of the constraints are symmetric and located at points ‘R’, ‘L’, and ‘M’ as seen in Fig. 7.4. The points ‘R’ and ‘L’ both constrain translation in the Y and Z directions and thus only move in the X direction while allowing rotation around all axes. Point ‘M’ is constrained in translation in the Y and X directions and thus can move in the Z direction while allowing rotation around all axes. These constraints are the same for all loading scenarios. The preload force is applied to the points ‘R’ and ‘L’ in opposite directions in line with the X direction. This preload force is created by compressed linear springs.

7.3.3 Parameters

The parameters used for this mechanism are chosen for the passive exoskeleton case and stated in Table 7.1. Although the mechanism can be scaled to fit multiple design purposes, the parameters for this research are mainly based on anthropometric data and optimization

Table 7.1: Parameters in this table are used for both modeling and experimental validation and are chosen based on an anthropometric data.

Parameter	**Symbol**	**Value**
Inside width	w	450 mm
Inside depth	d	160 mm
	p	125 mm
Curve radius	r	25 mm
H profile height	bh	34 mm
H profile width	bw	34 mm
Web thickness	btw	0.8 mm
Flange thickness	btf	0.8 mm
Density	ρ	$7880\,\mathrm{kg\,m^{-3}}$
Poisson ratio	υ	0.275
Youngs modulus	E	190 GPa
Free spring length	$\mathrm{L_0}$	86.6 mm
Maximum spring force	$\mathrm{F_n}$	102 N
Spring constant	c	$1.49\,\mathrm{N\,mm^{-1}}$

using simulations in Ansys, with a finite element solver. The width and depth of the mechanism have been obtained using anthropometric data from DINED [20] with the data set “Dutch adults, dined 2004”. w was obtained by taking a hip breadth of 400 mm plus two times 25 mm for the preloaded springs. p was obtained by taking half of the abdominal depth, which is chosen to align with the rotational axis of the hip joint. The hip breadth and abdominal depth were chosen around the 50 percentile of the age group of 20-60 years. These could be approximated because they will be used as input parameters for the optimization of the mechanism. For the radius of the two curves, R, early tests found that its contribution to the behavior of the beam was rather small. Therefore, it was removed from the scope of the research, and R was not varied in the optimization and has been chosen to follow the shape of the human body. bw and bh are the height and width of the H-profile cross-section. These were obtained using an optimization problem in Matlab, which is further explained in Section 7.3.6. For this research, the thickness of the web and flanges have been chosen to be equal. The thickness has been found by manual optimization based on available stock material thicknesses for prototyping purposes. A thickness of 0.8 mm was found to be best suited for the chosen design parameters and requirements. The springs used to apply the preload to the mechanism are also chosen based on the required force F_n, free length L_n and the highest possible spring constant c.

For the material AISI 301 or EN 1.4310, which is a hardened austenitic chromium-nickel stainless steel is used, with a Young’s modulus E of around 190 GPa, and an ultimate tensile strength between 1300-1500 $\mathrm{N\,mm^{-2}}$.

7.3.4 Modeling

For modeling the mechanism, Ansys Parametric Design Language (APDL) is used. The main advantage of this program is that the mechanism can be modeled using a scripting language and can be made as a parametric model. This ensures maximum control over the simulations and allows for simulating with different sets of parameters using Matlab. By using an integration of Ansys and Matlab, it is possible to run the Ansys model in an optimization problem to optimize the model for given input parameters and requirements of the mechanism.

The model is simulated in Ansys Parametric Design Language using Finite Element Modeling (FEM). The model is fully parametric and is fully constructed in the APDL scripting language. For the simulation, a static analysis with a large deflection option is used. A shell model is selected to simulate the behavior of the beam. The shell is meshed using 8-nodal SHELL281 elements.

The constraints are as aforementioned and applied to the nodes at the locations of points 'R', 'L', and 'M' on the shell. The preloading of the mechanism is performed by having two forces at points 'R' and 'L' in opposite directions. These forces simulate a linear spring in accordance with Hooke's law based on the U_x displacement of points 'R' and 'L'.

7.3.5 Measurement

The modeled mechanism can be actuated in two different ways: one-sided actuation and symmetrical actuation. For the one-sided actuation scenario, a rotation is applied to a line of nodes on the left inside of the mechanism, this line of nodes spans 25 mm in both directions of the Z-axis with the point 'R' in the middle. For the symmetrical actuation scenario, a line of nodes spanning a line in the Z direction at point 'M' in the web. For both scenarios, the rotation is around the X-axis. To obtain the Moment-Angle and Potential Energy-Angle curves, the required moment to actuate the mechanism to an angle in the range of motion has to be calculated. This is performed for both the one-sided actuation and symmetrical actuation scenario. The one-sided actuation moment is calculated in the simulations by measuring the reaction forces at point 'M'. With the known distance from point 'R' to 'M', this accounts for a change in distance in the deformed state, and the moment around the rotational axis between points 'R' and 'L' can be calculated. For the symmetrical actuation scenario, a similar approach is taken, however for this scenario, the reaction forces on points 'R' and 'L' are measured and converted to a moment around point 'M'. The reaction forces can be exported directly from the simulations. To calculate the potential energy at a given angle, a cumulative trapezoidal numerical integration is used. This approximates the area under the Moment-Angle graph, which is the potential energy. The rotational stiffness of the mechanism is calculated by differentiating the Moment-Angle curve, the focus of this chapter is mainly on the rotational stiffness at $\theta = 0$. The compliant differential mechanism has a difference in input angle and output angle, where the input angle is the actuated side of the mechanism and the output angle is the angle of the unactuated side, as can be seen in Fig. 7.2. In this research, the ratio between the input and output angles is defined as the kinematic performance. To calculate the kinematic performance of the compliant differential mechanism, the angle of both the actuated side and the unactuated side is measured. These angles are plotted against each other to find the correlation. From these data points, a linear regression is taken, for which the slope of this linear regression approximates the average kinematic performance over the complete range of motion.

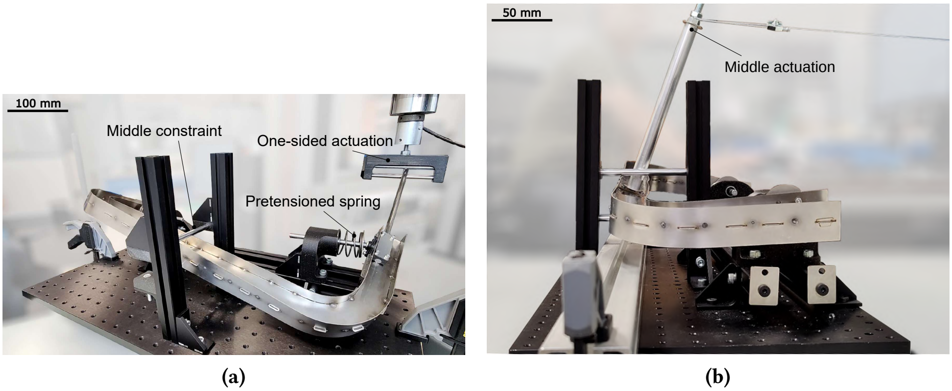

(a) (b)

Figure 7.5: The experimental setup for validation of the simulated results for both the symmetrical actuation and one-sided actuation scenarios.

7.3.6 Optimization

As discussed previously, the values of bw, bh and the initial preload to achieve neutral stability are found using optimization in Matlab. This was performed by Matlab running the Ansys model with different sets of parameters. As the objective function, a weighted function of both the root-mean-square error (RMSE) of the one-sided actuation moment and a penalty function for the required symmetrical actuation moment is used. The RMSE is used to approximate zero stiffness at $\theta = 0$. The penalty function is used to constrain the lifting moment to fit the desired symmetrical actuation moment. Sequentially, the initial preload of the spring was optimized using the same RMSE to find the initial preload for which zero stiffness is achieved and thus neutral stability.

7.3.7 Physical Prototype

The physical prototype is constructed with a hardened stainless spring steel with the properties mentioned in section 7.3.3. The thickness and properties of the material are in accordance with the simulated model. The material is laser cut with slits and wedges in the web and flanges to allow for alignment and fixation of the web and flanges. Although this gives a fairly rigid connection, it does not fully fixate the web and the flanges similar to the model. Therefore, spot welds are introduced to fixate the web and flanges.

7.3.8 Experimental setup

The experimental setup in Fig. 7.5 consists of the mechanism attached to two axes on linear sliders which constrains the translation in the Y and Z directions for points ‘R’ and ‘L’. To ensure that the constraint points are still allowed to freely rotate in all directions, a ball joint is used at the contact point between the axis and the inside flange of the mechanism. The preload force is applied to the mechanism using two springs which are attached to the two axes, this applies the force directly to the ball joint, and matches the simulated model. The constraint at point ‘M’ is only in the Y direction, contrary to the simulated model which was also constrained in the X direction. However, this constraint was omitted for the experimental setup because the springs removed a degree of freedom, which constrained the mechanism in the X direction.

7.3.9 Measurement

To measure the Moment-Angle curve, a tensile testing machine is used to actuate one side of the mechanism using a rod attached to the flanges and the web on one side of the mechanism, as shown in Fig. 7.5(a). The universal testing machine operates at a speed of $200\,\mathrm{mm\,min^{-1}}$. The measurement is performed by actuating one side of the mechanism to 25° and then to −25° before returning to 25°. The cycle is repeated twice for both sides of the mechanism to check for repeatability and to get more data points for smoother and more accurate results. The measured forces and displacements can be converted to a moment and angle with the known length and displacement of the actuation rod. The effect of the weight of the actuation rod is compensated for in the data processing. Due to Coulomb friction in the constraints, such as the ball joint and linear bearings, there is a hysteresis loop which centers around the predicted Moment-Angle curve, as can be seen in Fig. 7.6 in gray. The predicted true Moment-Angle curve can be subtracted from the hysteresis loop by averaging the higher and lower moments of the loop for each angle, this should be a close estimation if the mechanism is symmetrical and friction in both directions is assumed to be the same.

To measure the symmetrical actuation scenario, a rod is attached to the middle of the web at point 'M' a force is applied to this rod which causes a moment on the beam at the point of attachment. This force is applied using the tensile testing machine and a cable, as can be seen in Fig. 7.5(b). This force and the resulting displacement can be converted to a moment and an angle respectively. The springs are also tested separately to see if their force-deflection behavior is similar to that of the modeled linear springs.

Finally, to calculate the kinematic performance, an additional rod is attached to the unactuated side of the mechanism to better visualize its angle. A camera and video analysis software are used to measure both the input and output angles to calculate the kinematic performance of the mechanism. This calculation was performed using the same method as the simulated results by finding the slope of the linear regression.

7.3.10 Experiments

In this research, four different scenarios are considered for the experiments. The first three scenarios are variations of the initial preload of the springs: no preload 0 N, an initial preload of 70 N which makes the mechanism neutrally stable, and an initial preload of 95 N where the mechanism shows bistable behavior. For the fourth scenario, a rotation is applied to point 'M', the symmetrical actuation scenario. In this case, the preload effect is negligible and, therefore, is not considered in the tests.

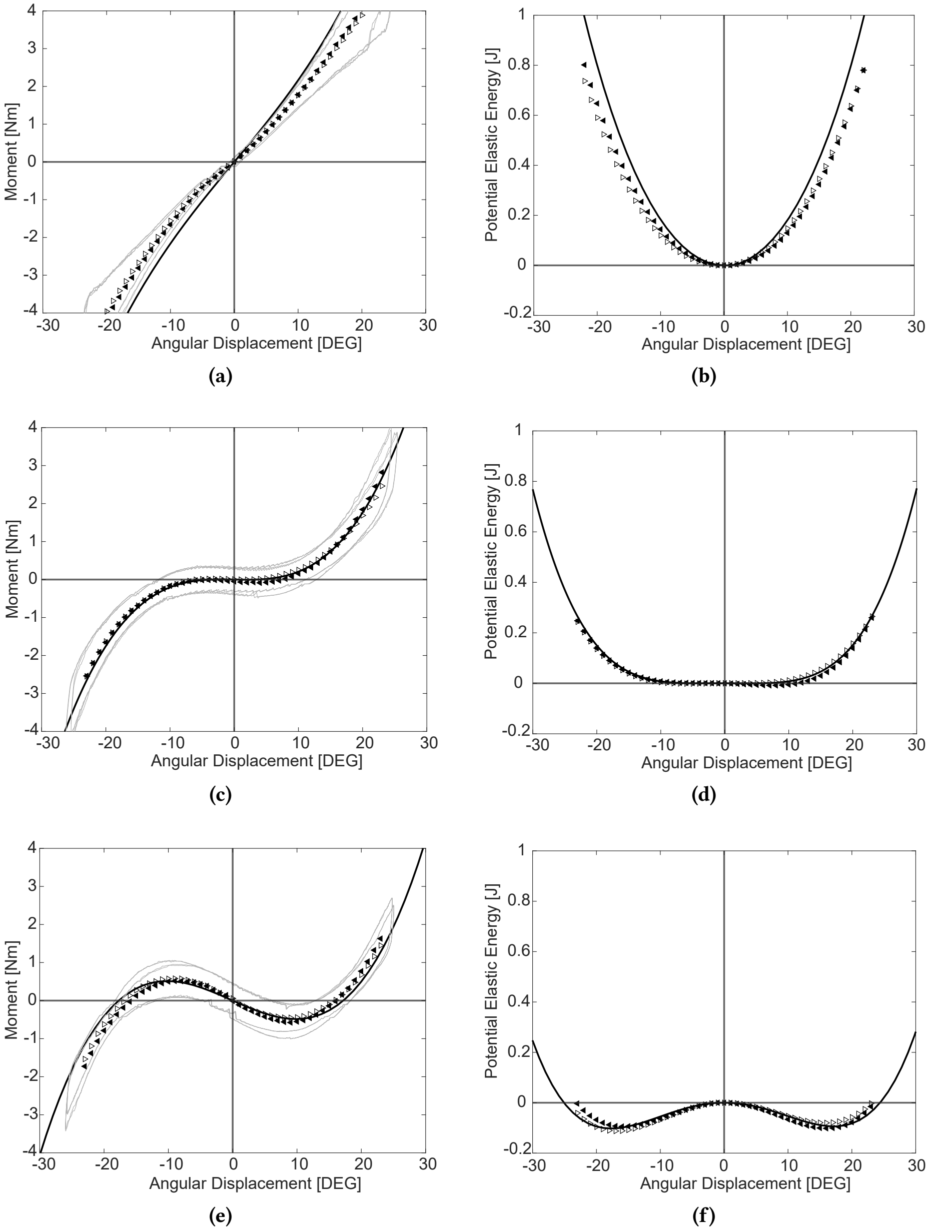

(a) (b)

(c) (d)

(e) (f)

Figure 7.6: The simulated (black) and the experimental (gray) results for the moment-angle and energy-angle of the mechanism in a one-sided actuation scenario with three different spring preloads. The ◂ and ▹ symbols show the friction compensated results for the left-side and right-side actuation respectively.

7.4 Results

Figure 7.6(a, c, e) shows with the black line the resulting simulated moments for one-sided actuation for no initial preload, initial preload which led to neutral stability, and an initial preload which results in bistability. These moments are plotted against the angular displacement in degrees. The experimental results are shown with ◂ and ▹ symbols for left and right side actuation, respectively. In light Grey, the raw measured results are shown, these results show a hysteresis loop due to the friction in the experimental setup. As discussed in Section 7.3.9, friction in the experiment results is compensated for by averaging the moments.

Figure 7.6(b, d, e) show the simulated potential energy in joules measured from the mechanism with the black line. Both of these cases are plotted against the angular displacement of one of the two actuated sides of the mechanism. The experimental results are shown with ◂ and ▹ symbols for left and right side actuation respectively. The potential energy is calculated from the sampled Moment-Angle curve. Hence, the friction in the results has already been compensated.

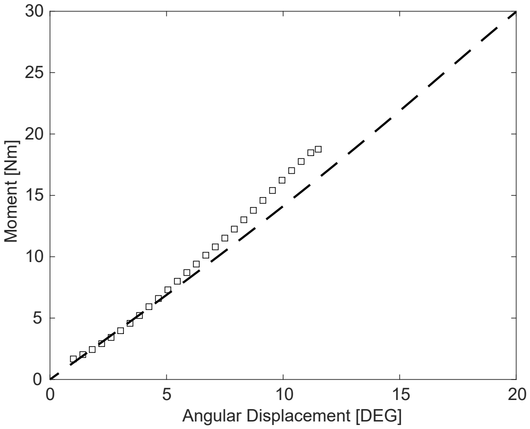

Figure 7.7: The moment required for the symmetrical actuation case, for the simulated results (dashed line) and the experimental results. The experimental results are shown with the □ symbol.

For the neutrally stable or zero stiffness scenarios, the results are shown in Fig. 7.6 (c, d). The results in Fig. 7.6(c) show a near zero moment within a range of motion of 16°, between −8° and 8°. Also the results in Fig. 7.6(d) show a near constant potential elastic energy within the same range. The constant potential energy and a slope of zero, can also indicate zero stiffness at $\theta = 0$.

For the bistable scenarios, the results are shown in Fig. 7.6(e, f). The results in Fig. 7.6(e) show a local minimum and a maximum at −10° and 10°, respectively. There are three locations where the moment is zero at: −17°, 0° and 17°, which are the equilibrium points. The results in Fig. 7.6(f) show the potential elastic energy with two local minima at −17° and 17°, which correspond to the equilibrium points in Fig. 7.6(e). Furthermore, the negative slope through $\theta = 0$ indicates negative stiffness. The experiments show the same behavior as the simulated results, but there is a slight difference. After the peaks the experimental results seem to have a steeper angle which indicates more stiffness, this can be observed in both the Moment-Angle curve and Potential Elastic Energy-Angle curve.

For the not preloaded scenarios, the results are shown in Fig. 7.6(a, b). The results in Fig. 7.6(a) show almost linear behavior going through the origin, which indicates an almost constant positive stiffness over the entire range of motion.

Figure 7.7 shows the moment for the symmetrical actuation scenario, the dashed line is the simulated moment for the symmetrical actuation scenario. These results show a linear relation with the angular displacement from 0 N m to the optimized value of 30 N m. The experimental results for the symmetrical actuation scenario are shown with the □ symbol. These experimental results show a deviation from the experimental results after 5°, after this point, a steeper slope can be observed which indicates a higher stiffness for the symmetrical actuation scenario.

Figure 7.8 shows that within the tested initial preloads, the mechanism shows a linear relationship between the preload and the stiffness of the mechanism at $\theta = 0$. This linear relationship is shown in Eq. 7.1, where k_ψ is the rotational stiffness and F_p is the initial preload of the springs.

$$k_\psi = -0.1673F_p + 11.6153 \tag{7.1}$$

This means that the initial preload is negatively correlated with the stiffness, and a higher initial preload results in a lower stiffness. This behavior can also be observed for negative preloads, with a force pulling inward instead of pushing outward. For initial preloads at 70 N zero stiffness is observed, indicating neutral stability. While for initial preloads higher than 70 N negative stiffness is observed, which indicates bistability. The experimental results are shown with the calculated stiffness using the ■ symbol.

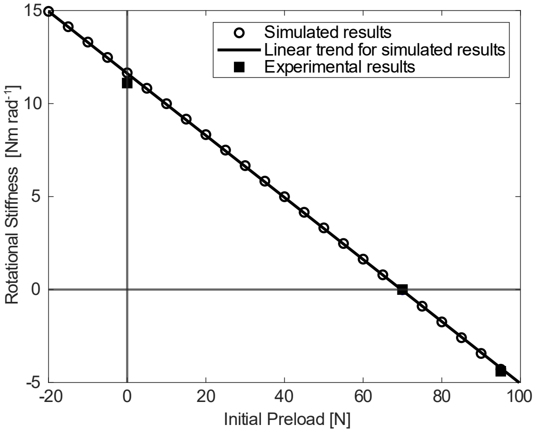

Figure 7.8: The effect of the initial preload of the springs on the rotational stiffness of the mechanism.

Figure 7.9 shows the kinematic performance of the different initial preloads from simulations. The dashed line shows a linear trend between the kinematic performance and the initial preload. The kinematic performance shows a linear trend between 0.96 and 0.98

for the simulations. The experimental results for the neurally stable scenario which are shown with the ■ symbol in the same figure is 0.95 for a 70 N initial preload; the error bar indicates the 95% confidence range.

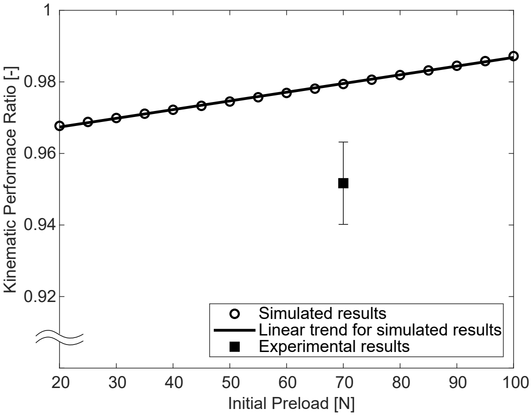

Figure 7.9: Kinematic performance, the ratio between motion of the actuated side and the unactuated side, for different initial preloads are shown with a linear trend between them, the resulting ratio from the experiment is also shown.

The linear approximation for the springs according to Hooke’s law has been tested. The compression test has been performed on the springs used in the experimental setup. The springs showed the same linear behavior as the simulated springs, with the same expected spring stiffness of 1.49 $\mathrm{N\,mm^{-1}}$.

7.5 Discussion

The expected behavior of neutral stability was found both in the simulations and experimental results for the optimized initial preload. This indicates that the current method, the reintroduction of potential energy, is an effective way to manipulate the stiffness. Furthermore, it is shown that by increasing the reintroduced potential energy, i.e., higher springs pretension, it is possible to achieve bistable behavior. This bistable behavior was observed in the simulated and experimental results.

The experimental results of the neutrally stable scenario almost perfectly match the simulated results. However, in bistable and non-preloaded scenarios, the experimental results show a small deviation from the simulated results. Furthermore, the results show consistency between cycles and sides of the mechanism. The small deviations could be due to the experimental setup, for example, the tool used to actuate the mechanism required a few millimeters of backlash to work properly, this is also the case for the fixation at point M. This backlash could cause a shift in the final processed results. This will be most pronounced in the not preloaded scenario due to the steeper slope. This backlash could be removed by creating better fixations.

Another discrepancy that could explain the differences between the simulations and the experimental results is the difference in exertion of the actuation. The simulated model is actuated only by applying an angular displacement, which differs from the experiments where it is applied by a linear displacement. This introduces forces into the system instead of only a pure moment. furthermore, the effect of the difference in constraints between the Ansys model and prototype seemed to be minimal but could be improved in future works.

Another source of difference between simulations and the experimental results can be due to the connection between the web and flanges, in the simulations, this is a uniform continuous rigid connection. However, in the experimental setup, a continuous connection was not feasible, and a connection using spot-welds was used, which gave the mechanism a rigid connection while minimally affecting the material properties at the connection. It is possible to use laser-welding to create a better fixation between the web and the flanges, this minimizes added material and only makes a relatively small heat affected zone. Another way to better match the results to the model is to model the connection between the web and the flanges in Ansys.

For the symmetrical actuation scenario, the optimization to reach 30 N m at 20° was successful and resulted in constant rotational stiffness in the desired range of motion. However, in the experiments a higher rotational stiffness was captured after 5°. This deviation could be caused by the difference in the exertion of the moment.

For the symmetrical actuation scenario, the full 20° of angular displacement could not be achieved due to buckling in the flanges, this buckling was observed after about 7°. The simulations also showed buckling, however, this only occurred at deformations higher than the 20°. Buckling at smaller deformations could be caused by the spot weld, which caused a non-uniform connection with the web, the spot-welds also caused some slight imperfections in the flanges which could also cause an earlier buckling. Due to this buckling, the experiment was stopped after 12° of angular displacement.

The kinematic performance for the simulated results is around 2% to 3% lower than the ideal ratio of 100%. The measured experimental results show only a 2% difference with a 95% transfer of motion. This is a high percentage and is considered a good result. This deviation between the experiments and the simulated kinematic performance can be seen in Fig. 7.9. This could be explained by a few factors, which are sorted based on their effects. Firstly, the friction in the experimental setup could cause losses in transferring motion from the input to the output side of the mechanism. This is believed to be the largest contributor to the discrepancy. Secondly, the minimum measurement unit for the angle using image processing was set to 1°. Finally, a camera was used to calculate the difference in angle between the actuated and unactuated arm; therefore, a difference in perspective or possible lens distortion can be another source of error during the measurements.

An important metric of this differential mechanism is the ratio between the rotational stiffness of the one-sided actuation (walking) and the symmetrical actuation (bending). This ratio for the range of motion of 20° is:

$$\frac{\text{Symmetrical actuation}}{\text{One-sided actuation}} = \frac{30}{1.76} = 17 \tag{7.2}$$

This is almost three times higher than the same ratio for the unpreloaded mechanism, for which this ratio is $\frac{30}{5.09} = 5.9$. This shows a significant increase in the difference in rotational stiffness by reintroducing energy to lower the overall rotational stiffness of the mechanism. The ratio could be even higher if the bistability of the mechanism was utilized; however, this bistability is not always desired. However, this bistability can be used to lower the overall required work to actuate the mechanism over a larger range.

When comparing the proposed compliant differential mechanism with the conventional differential mechanisms, the main advantages of the proposed design are the removal of backlash and friction, and the reduction in number of parts and thus assembly time. The main disadvantage of stored elastic energy for compliant differential mechanisms has been alleviated for a range of 16°, conventional differential mechanisms do not have this disadvantage and only suffer from friction between the gears. This friction is relatively low, but it is hard to compare to the proposed design due to the scalability of this proof of concept. The second limitation of the proposed compliant differential mechanism is the limited range of motion, while conventional differential mechanisms have continuous rotations this is limited for the compliant design. This is however a limitation which is not a problem for all design purposes.

Now that the expected behavior has been found and verified, more future research can be done into this mechanism. The design used for this proof of concept has been kept simple and uniform in order to find the behavior with as few variables as possible. In future research into the mechanism, a variation in the width and height of the beam could be investigated, for instance, the bw and bh of the beam could be optimized separately to see if the mechanism could be made more compact or have a wider range of motion with neutral stability and zero stiffness. Another interesting thing to look into is varying the thickness of the web and flanges as separate parameters, e.g., a lower thickness web could lower the stiffness of the mechanism while having less impact on the warping of the beam. Furthermore, from additional stress analysis that was outside the scope of this research, the two side sections around points ‘R’ and ‘L’ were found to be less important for the behavior of the mechanism and show much lower stresses than the straight back section. More narrow and compact dimensions could most likely be chosen for this area.

In addition to the dimensions, the cross-section could also be changed. While in initial testing a C-shaped and an I-shaped cross-sections seemed to perform worse than the H-shaped cross-section for the desired behavior, other sections could be further examined, especially if other parts of the mechanism are also altered. Cross-sections like open circular sections or T-profile which have not been looked into at all, could show different and possibly better behavior.

Another improvement is to change the source of potential energy storage in the mechanism. In the current version potential energy is stored in the external springs, but it can be replaced by prestresses in the mechanism itself. A similar approach to Lachenal [17] with prestressed flanges could be interesting to look into. Another approach would be to reduce the out-of-plane stiffness on the sides and store the potential energy in a fashion similar to that of the external springs in those two regions.

7.6 Conclusion

In this chapter, a compliant differential mechanism with near zero stiffness is presented. A method to manipulate the rotational stiffness of the mechanism by reintroducing energy to compensate for the inherent strain energy of the compliant mechanism due to elastic deformation. The compensation energy is supplied by pretensioned springs. Three different initial preloads of these springs have been investigated to show the effect on the mechanism's behavior: no initial preload, initial preload which makes the mechanism neutrally stable, and finally, an initial preload which causes the mechanism to have negative stiffness and becomes bistable. It was found that for the optimized value of 70 N spring pretension a neutrally stable range of motion of 16° can be achieved. Furthermore, it is shown that the initial preloads of the spring had a linear relationship with the mechanism's rotational stiffness at its neutral position at $\theta = 0$. This was even the case for negative stiffnesses for initial preloads greater than 70 N.

The initial requirements of the mechanisms were met. The maximum absolute moment between −25° and 25° for the one-sided actuation was 3.6 N m which is lower than the set requirement of 5 N m for walking, this was for the optimized initial preload of 70 N m. For symmetrical actuation, the mechanism was successfully optimized for the minimum required moment of 30 N m at 20° for bending. Due to the optimization of the mechanism, the dimensions of the mechanism were minimized while meeting the requirements.

The mechanism performed well as a compliant differential mechanism with high symmetrical stiffness and low stiffness when actuated from one side. The required moment after 20° of actuation was shown to be 17 times higher for the symmetrical actuation compared to the one-sided actuation. Furthermore, a high kinematic performance was observed for the one-sided actuation of more than 0.97 in the simulated results, with the experimental results showing only 2% lower.

It can be concluded that this compliant differential mechanism can be optimized to have a range of motion for which the potential energy can be near constant and that the stiffness outside of this range is also reduced significantly. This was validated using both simulations and experimental validation. Furthermore, the mechanism can be easily optimized to fit specified requirements for a chosen application. This application could be for the use in an exoskeleton design, for which the mechanism can be optimized for a specific user, or in other applications where having a monolithic, lightweight, and scalable mechanism is essential.

References

[1] M. T. Wright, "The Antikythera Mechanism reconsidered," *Interdisciplinary Science Reviews*, vol. 32, pp. 27–43, 3 2007.

[2] M. Santander, "The Chinese South-Seeking chariot: A simple mechanical device for visualizing curvature and parallel transport," pp. 782–787, 9 1992.

[3] V. V. Vantsevich, *Advanced Autonomous Vehicle Design for Severe Environments.* 10 2015.

[4] M. C. Valentijn, "Thin-walled Warping Beams for Differential Mechanism Applications," tech. rep., Delft University of Technology, 2020.

[5] A. Amoozandeh Nobaveh, J. L. Herder, and G. Radaelli, "A compliant continuously variable transmission (cvt)," *Mechanism and Machine Theory*, 2023.

[6] L. L. Howell, *Compliant Mechanisms.* John Wiley & Sons, 2001.

[7] L. L. Howell, S. P. Magleby, and B. M. Olsen, *Handbook of Compliant Mechanisms.* Wiley, 2 2013.

[8] P. G. Opdahl, B. D. Jensen, and L. L. Howell, "An investigation into compliant bistable mechanisms," in *International Design Engineering Technical Conferences and Computers and Information in Engineering Conference*, vol. 80319, p. V01BT01A046, American Society of Mechanical Engineers, 1998.

[9] S. Kok, G. Radaelli, A. A. Nobaveh, and J. Herder, "Neutrally stable transition of a curved-crease planar shell structure," *Extreme Mechanics Letters*, vol. 49, p. 101469, 2021.

[10] J. A. Gallego and J. Herder, "Criteria for the Static Balancing of Compliant Mechanisms," tech. rep., 2010.

[11] M. Schenk and S. D. Guest, "On zero stiffness," 2014.

[12] F. M. Morsch and J. L. Herder, "Design of a generic zero stiffness compliant joint," in *International Design Engineering Technical Conferences and Computers and Information in Engineering Conference*, vol. 44106, pp. 427–435, 2010.

[13] H. Zhao, C. Zhao, S. Ren, and S. Bi, "Analysis and evaluation of a near-zero stiffness rotational flexural pivot," *Mechanism and Machine Theory*, vol. 135, pp. 115–129, 2019.

[14] J. A. Gallego, "Statically Balanced Compliant Mechanisms: Theory and Synthesis," tech. rep., 2013.

[15] E. Kebadze, S. Guest, and S. Pellegrino, "Bistable prestressed shell structures," vol. 41, p. 2801–2820, 1 2004.

[16] S. Daynes and P. M. Weaver, "Stiffness tailoring using prestress in adaptive composite structures," *Composite Structures*, vol. 106, pp. 282–287, 2013.

[17] X. Lachenal, S. Daynes, and P. M. Weaver, "A non-linear stiffness composite twisting I-beam," vol. 25, pp. 744–754, 4 2014.

[18] J. L. Herder and F. P. A. van den Berg, "Statically Balanced Compliant Mechanisms (SBCM'S): An Example and Prospects," 9 2000.

[19] A. Stapel and J. L. Herder, "Feasibility Study of a Fully Compliant Statically Balanced Laparoscopic Grasper," 2004.

[20] T. Huysmans, L. Goto, J. Molenbroek, and R. Goossens, "Dined mannequin," *Tijdschr. Voor Hum. Factors*, vol. 45, pp. 4–7, 2020.

8

Discussion

This chapter discusses the main accomplishments of the preceding parts of the thesis, in addition to outlining potential areas of application for these developments and their constraints. Additionally, a comprehensive assessment of the entire research project is presented, including recommendations and limitations that may prove advantageous for future scholars studying this topic.

8.1 Overview

In this thesis, different designs for slender spatial compliant elements with the primary objective of augmenting the functionality of modern exoskeletons are proposed. The study is divided into three primary parts. Part I discussed the design of spatially curved beams, the characterization of their kinetostatic behavior, and tuning this behavior as per requirement. Part II elucidated the behavior of straight open thin-walled twisting beams and demonstrated potential functionalities that can be harnessed from these elements. Finally, Part III proposed two applications of the aforementioned design methods in passive exoskeletons.

The subsequent subsections discuss the discoveries, conceivable applications of the design in exoskeletons, limitations of the methods and possible avenues of future research and developments in other related fields for each part of the thesis.

8.1.1 Part I - Spatially curved beams

In Part I, the impact of modifying the shape and sectional parameters of spatially curved beams to attain certain kinetostatic behavior at their endpoints was demonstrated. Based on this work and the understanding of how to illustrate the spatial kinetostatic behavior, we have presented a characterization method for these types of beams in the second chapter of this part. By using the characterization, we got a grasp on the contribution of torsion and bending stiffness of elements along the beams to the kinetostatic behavior of the endpoint. It is important to note that the effect of torsional deformation is barely investigated in the current state-of-the-art CMs since most of the developed mechanisms are planar where torsion is not defined. The effect of torsional deformation of elements along the structure on the kinetostatic behavior of the endpoint can be clearly seen in the results of the shape optimizer that is developed in Chapter 2. By employing this understanding and combining dissimilar elements in terms of torsion and bending, exceptional behaviors can be achieved that were not possible in the known realm of CMs. One example of these behaviors is described in Chapter 3 as anisotropic variable stiffness.

The presented designs can be applied to several parts of the exoskeletons since slender structures with a predefined force-displacement behavior, such as the presented beams, are favored for most connections in these devices since they can store energy and serve as an additional source of support for the users of passive exoskeletons. These beams also require little space and can provide complex functionalities; one example is the asymmetric beams with symmetric behavior that are presented in Chapter 2. The resulting beam was developed as a unilateral supporting structure for the forward bending of people who use wheelchairs and need support for bending. This unilateral beam can provide symmetric support similar to a closed bilateral structure around the upper body while giving freedom and safety to its users due to its open and slender nature. Moreover, it is expected that the use of these compliant beams as connection elements can contribute to the overall support provided by wearable devices. In this context, the design presented in Chapter 3 helps the user to adjust this support in a particular direction on demand. As an example, in back-support exoskeletons, the support for forward bending can be adjusted based on preference or on the type and intensity of work, while the support stiffness in other directions is preserved, in other words, the lateral bending flexibility remains the same during the adjustment of front bending support.

The use of such spatially curved compliant elements also entails limitations. The first limitation is associated with the fabrication of these beams, since extruding and bending them requires complex machines and producing them using additive manufacturing methods, as of yet is not economically feasible. During the project, parallel research was conducted on the development of methods for manufacturing the designed beams that are introduced in Part I, these methods also have challenges that can be further explored. Another limitation is related to the complexity of kinetostatic behavior that can be expected from these beams. Since they are only single-branch beams, achieving a wide range of nonlinear characteristics cannot be expected from them, and the kinetostatic outcome is limited. Finally, the distribution of strains in the beam and fatigue due to repetitive motions, which are two of the most important factors in the failure of CMs, are harder to control in a single-branch beam structure like the ones presented here.

In future research, it is possible to combine multiple beams and establish connections between them to achieve more intricate behaviors for certain applications. By doing so, the structure of beams will be able to create more complex behavior at each node, and therefore, the overall kinetostatic behavior can be more sophisticated. Combining beams can result in multi-stable structures, as one example. Moreover, having a network of beams can provide more possibilities regarding the intermediate deformed shape of the structure in large deformations. This can help the designers of exoskeletons make largely deformable compliant elements that conform to the body in different phases of support. It is also important to mention that by adding complexity to the shape, the slenderness of the overall structure will decrease, and therefore there is always a trade-off. By having a network of beams, it is also possible to introduce intermediate contact between them after a certain amount of deformation. This can facilitate the implementation of behaviors such as softening or stiffening and provide more possibilities for the type of nonlinear force displacement behavior that can be expected from the structure.

Utilizing the designs for spatially curved compliant beams that are introduced in this section can be relevant to various other fields of research, such as surgical robots and catheters, since they need to reach certain locations through complex paths around organs inside the body and yet provide certain kinetostatic behavior at their tip points. Also in aerospace structures spatially curved beams may be relevant, for instance when specific shapes are required due to aerodynamic requirements, only certain spatial shapes are available, yet the structure should be fully functional due to weight limitations and crucial working conditions. Finally, in biomimetic robots, replicating creatures' motions requires complex functional structures. Moreover, surviving in harsh conditions, e.g., dirt and sand or high water pressure, requires monolithic functional parts that can provide support and motion.

8.1.2 Part II - Twisting beams

The present study demonstrates the capability of the warping phenomenon to transmit sectional twist along open thin-walled beams. A monolithic design for a transmission mechanism is presented based on this concept and the analytical model for this transmission along the length of the beam is established, paving the way for the development of monolithic variable transmission ratio elements. In the second step, to achieve zero stiffness in these twisting elements, a novel method is proposed that allows for variable and switchable torsional stiffness of this type of thin-walled beams.

The aforementioned beam with a high warping constant holds potential as a lightweight, compliant transmission in exoskeletons to enhance the match with the kinematics of the human body and reduce overall energy expenditure. Additionally, the variable-stiffness twisting element may function as a passive adaptive support structure for switching between tasks, e.g., forward bending, walking, and sitting, since the exoskeleton needs to have different support characteristics and therefore, different stiffness in each of these tasks.

Nonetheless, both twisting elements exhibit limitations, such as their limited range of rotation, which is common among CMs. Moreover, the manner in which these elements should be constrained presents a challenge since the deformation of sections is essential to the functionality, and therefore, the sections can only be constrained at specific locations where there are no out-of-plane displacements. Furthermore, the current rotational constraint in Chapter 4, which introduces different transmission ratios, is made from conventional mechanisms since its fixed ring requires sliding along the structure and making rigid contact with the beam at certain locations.

Further research can explore the combination of the transmission and variable torsional stiffness features in the curved beams that are introduced in Part I. The transmission via warping can be used to transfer sectional deformations along the structure to provide couplings between deflection modes with the aim of achieving certain anisotropic behaviors, such as extendable compliant beams with high bending stiffness. Moreover, it is possible to make structures where the overall stiffness can be manipulated from the base, since effects like warping in the base can propagate along the structure and change the stiffness of the endpoint. This feature can be widely used in robotics, where manipulation of the endpoint of a structure using actuators in the base is a common requirement.

The development of transmission without backlash is of significant interest in several research fields, including precision applications. The proposed design in Chapter 4 is a concrete answer to this requirement. Moreover, due to the lightweight of the presented beams, they can be suitable for shape-morphing wings or blades in aerospace applications where utilizing both fine control over deformation of the wing shape using compliant transmission and control over torsional stiffness of a wing or blade using the variable stiffness solution seems to be promising. Lastly, the presented compliant switchable stiffness twisting element can be miniaturized, making it an excellent candidate as a revolute joint with on-off stiffness for applications such as micro-robots or metamaterials.

8.1.3 Part III - Applications in passive exoskeletons

As mentioned in the previous subsections, the methods and tools that presented in this thesis have potential applications in various fields of research, including wearable devices such as exoskeletons, prostheses, and orthoses. Part III of this thesis presents two direct applications of the methods described in the earlier sections and the developed finite element tools that can also be fined in *doi.org/10.4121/be2fd76a-f037-44e0-a002-61c2276068cd* for other possible applications.

In this part, firstly, the optimization scheme that described in Chapter 2 was used to design a beam that balances the weight of the user’s hand in a relatively large range of motion of the wrist, reducing muscular effort for flexion and extension. This beam was then integrated with a soft actuator, resulting in a hybrid system that requires less energy to help the wrist movements. Secondly, the transmission presented in Chapter 5 was utilized to design a differential system that averages legs angle to upper body connection, addressing one of the primary challenges of passive back support exoskeletons which is the activation of the bending support mechanism in each walking step of the user.

Implementing the presented methods in exoskeletons has several advantages, but working with a complex system such as the human body also presents new challenges and limitations. Since the presented designs are based on ideal human kinematics, several other motions and considerations must be taken into account when designing for exoskeleton parts. These considerations range from the interfaces with the body and applying reaction forces from the support with the least discomfort to the directions in which mechanisms should provide freedom, size adaptability, differences between users' gaits, and several other considerations. Incorporating all of these considerations into the design requires a deeper understanding of human factors and biomechanics.

It is important for designers and users of these elements to be aware of the limitations and risks associated with using CMs for exoskeletons, since large deformations in CMs result in the material's strain being pushed to its yield limit. Considering the inherent motion uncertainties of the human body, having such largely deformable spatial elements for supporting unbounded body movements can increase the risk of going over the yield limit and failure.

Future research could focus on addressing the biomechanical issues associated with the presented designs and possibly considering the implementation of human models in the design process of these compliant elements. This can help the designers better understand the limitations regarding the reaction forces and moments on the human joints and the kinematic and force limitations for providing support to one part of the body using other parts. Additionally, close collaboration with the designers of commercial passive and active exoskeletons can help the designers of compliant mechanisms have a clearer idea of the requirements and help promote the use of their designs as the subsystems of commercial exoskeletons. The subsystem can be a part with certain kinetostatic behavior or an energy-saving addition to the wearable devices.

8.2 Limitations and Recommendations

The current work mainly looks at single-branched curved beams as a promising topology to be close to the body and conform to it while providing design freedom to achieve certain kinetostatic behaviors. Achieving the desired behavior can happen by tuning the beam shape in the area close to the body and taking advantage of less investigated spatial modes of deformation. The investigation started with a single branch of Euler-Bernoulli's beam and diverged in several directions to introduce new features into this simple and essentially straight element. The initial beam does not warp, the sectional deformation is not modeled, the shear is not considered and it is also set to be prismatic and have no twist or prestress. In Chapter 2, the curvature was added to these beams and the control over kinetostatic behavior was achieved. In Chapter 3 a type of non-prismatic beam was introduced and control over anisotropy was achieved. In Chapter 4 the effect of warping was considered and the transmission was achieved. And finally, in Chapter 5 the change of prestressing provided control over torsional stiffness. These investigations show that adding one step of complexity to the simple beam can cause exceptional functionalities. There are yet several possibilities for these beams, from the combination of the mentioned effects or from the non-studied effects, like shear, that can possibly cause other interesting and functional effects. Also, while the current work has concentrated on prismatic beams with negligible in-plane sectional deformations, incorporating variable sections along the structure and in-plane deformable sections could lead to new avenues for development of different kinetostatic behaviors.

Current designs for compliant elements in the literature are barely taking advantage of the torsion-related effects that are utilized in this work or those that have yet to be investigated, such as lateral torsional buckling. A deeper understanding of these effects could facilitate the development of new design techniques for controlling the kinetostatic behavior of spatial structures.

In the realm of passive exoskeletons, it is also possible to use 2D compliant shell structures instead of 1D beams. However, considering the limitation of the 2D design space close to the body, using shells heavily limits the parameters available for the design since the shape of the shell should essentially match the body shape, and achieving certain kinetostatic behavior by controlling the shape is therefore challenging. However, in the case of 1D spatial beams, which are selected as the main direction of development for this thesis, there are more possibilities in the same design area close to the body. This makes them a good choice for implementation and research in exoskeletons, and as it discussed before, still major directions of development for these beams are available that can be promising directions of development for successors to this research line.

9

Conclusion

This dissertation introduces designs for slender spatial compliant elements with specific kinetostatic behavior, with the aim of application in passive exoskeletons. In search of making slender, lightweight, flexible structures that can provide the nonlinear kinetostatic behavior required to support the human body, previous researchers widely investigated the potential of using compliant shell elements for this application; however, matching the shape of these shells with the available area close to the body implies constraints to the design space and restricts the range of achievable behavior. To overcome limitations of shells, spatial compliant beams were selected since they can provide enough parameters for the designers to achieve the desired behavior even in a limited design area close to the user's body.

By starting with one of the simplest elements, an Euler-Bernoulli beam, the understanding of how known three-dimensional deformation modes can contribute to the overall functionality of compliant beams was achieved. Several steps were taken in this thesis to add complexity to the design of these beams to achieve more intricate kinetostatic behaviors which are required in the domain of exoskeletons. It is demonstrated that making spatial curvatures in beams enables torsional deformation of elements along a structure, which is recognized as an effective deformation mode for controlling the endpoint stiffness of a single branched beam. Going from prismatic to non-prismatic beams and the combination of torsion-related effects with well-investigated bending effects enabled a wide range of design possibilities to achieve complex kinetostatic behavior such as anisotropic adaptive stiffness. Understanding secondary effects like beam warping, which causes a coupling in the torsional deformation of sections in open thin-walled beams, allowed for the introduction of widely applicable mechanical functions like transmission. Furthermore, the effect of prestressing in the direction of the stiffest mode of deformation of the beams with deformable sections led to controlling certain stiffness, i.e., achieving negative and zero torsional stiffness.

The understanding of each of the effects that can be enabled in spatial compliant beams has shown to be beneficial in providing a wide range of functionalities and complex kinetostatic behaviors. There are a handful of other effects in beams, e.g., non prismatic sections and shear, that are not investigated and can potentially lead to more intricate solutions.

Also, the combination of these beams in a network can lead to more intricate behaviors. This direction of research not only contributes to the field of passive exoskeletons but also to the broader realm of mechanical design since the integration of functionality into a slender lightweight element can make them preferable over conventional rigid body mechanisms. Moreover, going back to the root and looking at simpler topologies for more intricate behaviors rather than investigating more complex topologies worked effectively in this thesis and resulted in promising design directions. This demonstrates the effectiveness of the approach taken in this work, and the same way of thinking can be adapted more broadly in other fields of engineering design.

Curriculum Vitæ

Ali Amoozandeh Nobaveh

1992/10/19	Born in Tehran, Iran

Education

2019-2023	*PhD in Spatial Compliant Mechanisms* Department of Precision and Microsystems Engineering Delft University of Technology, Delft, The Netherlands Thesis: *Synthesis of slender spatial compliant mechanisms* Promotor: *Prof. dr. ir. Just L. Herder* Co-Promotor: *Dr. ir. Ron A.J. van Ostayen* Supervisor: *Dr. ir. Giuseppe Radaelli*
2015-2018	*MSc in Mechanical Engineering (Applied Design)* Department of Mechanical Engineering Sharif University of Technology, Tehran, Iran Thesis: *Design and fabrication of a full-size humanoid social robot* Supervisor: *Prof. dr. Ali Meghdari*
2011-2015	*BSc in Mechanical Engineering* Department of Mechanical Engineering University of Tehran, Tehran, Iran Thesis: *Design and fabrication of an electromechanical debonder for orthodontic bracket* Supervisor: *Dr. Farshid Najafi*

Experience

2017-2019	*ASNT NDT level II inspector (Part-time)*
2013-2017	*Product design and development engineer (Part-time)*

Publications related to PhD project:

Journal publications:

8. **Amoozandeh Nobaveh, A.**, Herder, J.L. & Radaelli, G., (2023). *A compliant variable negative- zero- positive- stiffness twisting element.* Submitted. 🗎

7. **Amoozandeh Nobaveh, A.**, Herder, J. L., & Radaelli, G. (2023). *A compliant Continuously Variable Transmission (CVT).* Mechanism and Machine Theory, 184, 105281. DOI: 10.1016/j.mechmachtheory.2023.105281 🗎

6. Mak, R.,**Amoozandeh Nobaveh, A.**, A., Radaelli, G., & Herder, J. L. (2023). *A curved compliant differential mechanism with neutral stability.* Journal of Mechanisms and Robotics, 1-11. DOI: 10.1115/1.4056867 🗎

5. van der Lans, D., **Amoozandeh Nobaveh, A.**, A., & Radaelli, G. (2023). *Reversible shape morphing of a neutrally stable shell by untethered local activation of embedded Ni-Ti wires.* Journal of Intelligent Material Systems and Structures, 1045389X221151065. DOI: 10.1177/1045389X221151065

4. Kok, S., **Amoozandeh Nobaveh, A.**, & Radaelli, G. (2023). *Neutrally stable double-curved shells by inflection point propagation.* Journal of the Mechanics and Physics of Solids, 171, 105133. DOI: 10.1016/j.jmps.2022.105133

3. **Amoozandeh Nobaveh, A.**, A., Radaelli, G., & Herder, J. L. (2023). *Symmetric kinetostatic behavior from asymmetric spatially curved beams.* Journal of Mechanisms and Robotics, 15(4), 041010. DOI: 10.1115/1.4055419 🗎

2. **Amoozandeh Nobaveh, A.**, Radaelli, G., van de Sande, W. W., van Ostayen, R. A., & Herder, J. L. (2022). *Characterization of spatially curved beams with anisotropically adaptive stiffness using sliding torsional stiffeners.* International Journal of Mechanical Sciences, 234, 107687. DOI: 10.1016/j.ijmecsci.2022.107687 🗎

1. Kok, S., Radaelli, G., **Amoozandeh Nobaveh, A.**, & Herder, J. (2021). *Neutrally stable transition of a curved-crease planar shell structure.* Extreme Mechanics Letters, 49, 101469. DOI: 10.1016/j.eml.2021.101469

🗎 Included in this thesis.

Peer-reviewed conference publications:

5. Mak, R., **Amoozandeh Nobaveh, A.**, A., Radaelli, G., & Herder, J. L. (2022, August). *A Curved Compliant Differential Mechanism With Neutral Stability.* In International Design Engineering Technical Conferences and Computers and Information in Engineering Conference (Vol. 86281, p. V007T07A004). American Society of Mechanical Engineers. DOI: 10.1115/DETC2022-89406

4. **Amoozandeh Nobaveh, A.**, & Caasenbrood, B. (2022, July). *Design Feasibility of an Energy-efficient Wrist Flexion-Extension Exoskeleton using Compliant Beams and Soft Actuators.* In 2022 International Conference on Rehabilitation Robotics (ICORR) (pp. 1-6). IEEE. DOI: 10.1109/ICORR55369.2022.9896528 🗎

3. **Amoozandeh Nobaveh, A.**, A., Radaelli, G., & Herder, J. L. (2022). *A design tool for passive wrist support.* In Wearable Robotics: Challenges and Trends: Proceedings of the 5th International Symposium on Wearable Robotics, WeRob2020, and of WearRAcon Europe 2020, October 13–16, 2020 (pp. 13-17). Springer International Publishing. DOI: 10.1007/978-3-030-69547-7_3

2. Yellowhorse, A., Rommers, J., **Amoozandeh Nobaveh, A.**, & Herder, J. L. (2021, August). *Methods for shape fitting in morphing compliant mechanisms.* In International Design Engineering Technical Conferences and Computers and Information in Engineering Conference (Vol. 85444, p. V08AT08A021). American Society of Mechanical Engineers. DOI: 10.1115/DETC2021-70686

1. **Amoozandeh Nobaveh, A.**, A., Radaelli, G., & Herder, J. L. (2021). *Asymmetric spatial beams with symmetric kinetostatic behaviour.* In ROMANSY 23-Robot Design, Dynamics and Control: Proceedings of the 23rd CISM IFToMM Symposium 23 (pp. 247-254). Springer International Publishing. DOI: 10.1007/978-3-030-58380-4_30

🗎 Included in this thesis.

MSc thesis projects supervised:

- Sjaak Kok, *Towards Neutrally Stable Compliant Shells*, (2020, Sep)
- Maurice Valentijn, *Thin-walled warping beams for differential mechanism applications*, (2020, Oct)
- Tom Cratsborn, *Designing a compliant hip-back support for an exoskeleton*, (2021, Feb)
- Laurens Staats, *Stiffness reduction of cantilever I-beams through lateral torsional buckling for compliant beams*, (2021, Jul)
- Robyn Gerlach, *Compliant curved beam transmission systems*, (2021, Jul)
- Robin Mak, *A Curved Compliant Differential Mechanism with Neutral Stability: For the use in Exoskeleton Design*, (2021, Aug)
- Marc Gritter, *The design of a robot mounted far-reaching X-type projection welding machine*, (2021, Oct)
- Stijn Houweling, *Slender compliant mechanism with a low axial-bending stiffness ratio for use in an exoskeleton*, (2022, Sep)
- Sjors van Nes, *The use of a rigid linkage balancer with torsion springs to realize non-linear moment-angle characteristics*, (2022, Nov)
- Tzu Lee, *A compliant spherical remote-center mechanism with variable stiffness*
- Siyang Zhou, *Design of an arm support compliant exoskeleton with biomechanical modeling of its effect on human joints.*
- Dhanush Chitluri, *A passive hand-support for Duchenne Muscular Dystrophy patients*
- Saralina Koentges, *A slender back support mechanism with non-linear behavior*

BSc thesis project supervised:

- Luuk Schattenberg, Wessel Schilders, Niels Flikweert, Kevin Pun, *Design of a grooving machine for spatially curved beams*, (2022, June)

Acknowledgments

This dissertation is the result of an enjoyable yet challenging journey. I wouldn't have completed it without the support and encouragement of my great supervisors, colleagues, friends and family. Although it is difficult to express my gratitude with words, I would like to use this opportunity to acknowledge and thank them.

It is a genuine pleasure to express my deep gratitude to my promotor, **Just**, for giving me the opportunity to work on this project and for supporting me throughout the ups and downs in the entire journey. I have learned so much from him, not only about design, but also about being a great teacher and supporting several people while in all situations, remaining calm and thoughtful. I would also like to acknowledge the invaluable help of my co-promotor, **Ron**, whose insightful suggestions made the path of my research much clearer.

Working with certain people feels like a continuous learning experience, and **Giuseppe**, my supervisor, is definitely one of those people. I consider myself extremely lucky to had him on my supervisory team. He is an incredibly knowledgeable, kind, and always available person without whom I could not have achieved most of the things that I have now in this thesis.

I'd like to express my gratitude to the master's students with whom I had the opportunity to work as a supervisor. **Maurice**, **Sjaak**, **Tom**, **Laurens**, **Robyn**, **Robin**, **Marc**, **Stijn**, **Sjors**, **Tzu**, **Siyang**, **Dhanush** and **Saralina**. Your contributions were significant to the success of this project, and I enjoyed all of our pleasant brainstorming and discussions.

In this project, I had the chance to work with four companies as the users of the project. People at **Laevo** helped me a lot to have a clearer idea of what is needed for exoskeletons and to create more applicable designs. I should thank **Boudewijn** for his support. Beside the knowledgeable and friendly people from the R&D team at Laevo and Intespring, my friend **Bas**, who is a great person and a talented engineer. **Mike**, who is one of the best designers I have ever seen, and all other knowledgeable engineers, **Jaromir**, **Rogier** and **Frank** that I had the opportunity to work with them. Moreover, I should thank other supporters of the project, my bright friend **Sjaak** from **Yumen Bionics**, **Marina** from **By-wire** and **Arthur** from **Baat Medical**. I learned a lot from them and had a great time working with them.

I would also like to thank my supervisors and colleagues in wearable robotics program. **Herman**, the leader of the project, who was always there to support us, **Edwin** and **Arjen**; and my dear friends **Brandon**, **Suzanne**, **Cor**, **Wouter**, **Niels**, **Ali**, **Alejandro**, **Mariska**, **Eline**, **Martijn**, **Ander** and **Nauzef**. I learned a lot and truly enjoyed working with this team.

To work on this project, I have received great support from all the staff in our department. Their assistance made everything much smoother and easier throughout this journey. The technical support of PME, including **Patrick**, **Bradley**, **Spiridon**, **Gideon**, **Alex**, and **Rob**, were always available to help, and their presence made complex tasks look easy. I would like to specifically thank **Patrick** for all his help with experiments, and **Bradley**, **Spiridon**, and **Gideon** for their assistance in making prototypes and setups. I also would like to thank **Birgit**, **Eveline**, **Annemieke**, **Sylviane**, **Marli** and **Marianne** for their invaluable assistance and support, which made all procedures much smoother for me. I also like to acknowledge **Lisette**, the manager of our department, for her efforts in ensuring that everything ran seamlessly in PME.

I would like to express my heartfelt gratitude to several individuals who have been instrumental in making my journey through the Mechatronic System Design (MSD) group a success. I am grateful to **Hassan**, **Jo**, **Nima T**, **Volkert**, and **Davood** as the supervisory team, and the talented researchers that helped me in the beginning phase of my PhD **Werner**, **Jelle R**, **Reinier**, **Freek**, **Ali A**, **Philipp**, **Niranjan**, **Thijs**, **Joep**, **Jaap**, **Andres**, and **Alden** with whom I had the pleasure of working.

My colleagues and my great friends **Nima K**, **Ad**, **Abdullah**, **Francesco**, **Marcin**, **Malte**, **Jelle S**, **Xinxin**, **Dave** and **Ali** have also been instrumental in creating a positive and productive work environment. I cannot express how much I have enjoyed our conversations and brainstorming in the office, and our fun time during outings and conferences. I believe one of the biggest achievements of this journey was to find friends like them.

I would like to thank my colleagues in PME, whose friendly smiles and short chats during lunch and coffee breaks were always uplifting. Special thanks to **Mingkai**, **Gerben**, **Daniel**, **Thomas**, **Stijn**, **Arnoud**, **Pieter**, **Qais**, **Abilash**, **Irek**, **Andrea**, **Vibhas**, **Hanqing**, **Zhichao**, **Vijay**, **Lucas**, **Inge**, **Ata**, **Nils**, **Gürhan**, **Xianfeng**, **Frederike**, and **Pierre**.

In the last four years, my time in the Netherlands has been wonderful, and I owe it to my amazing friends who have always been there for me and supported me. My friends **Amir**, **Tino**, and **Hesan** with whom I had a great time and several joyful conversations. I also wish to thank **Ali** and **Shaghayegh**, **Saleh** and **Mahnaz**, **Davood** and **Afagh**, **Amir** and **Zahra**, **Ghobad** and **Sonia**, **Nima** and **Delaram**, **Ali** and **Azar**, **Hassan** and **Elaheh**, who have made my life in the Netherlands much nicer. They are all dear to me, and I appreciate having them in my life.

I am forever grateful to my parents, **Shiva** and **Ghasem**, for their unwavering support and for providing me with everything they had. From them, I learned valuable lessons about living, thinking, and even working. Additionally, I would like to express my gratitude to my sister, **Reyhaneh**, and my brother-in-law **Hamed**, they have been an unlimited source of support throughout my life. Words cannot fully convey my appreciation for my family and all that they have done for me.

Finally, I would like to thank my beloved **Shahrzad**. Her presence by my side has always been a source of inspiration for me to strive for excellence. I cannot overstate the importance of her role to allow me to fully enjoy life.

به پایان آمد این دفتر حکایت همچنان باقی …

Ali Amoozandeh
Delft, March 2023